MAGNETOTELLURIC IMAGING OF CONVENTIONAL AND UNCONVENTIONAL GEOTHERMAL RESOURCES

A dissertation presented

by

Yohannes Lemma Didana

In fulfilment of the requirements
for the degree of

Doctor of Philosophy
in the subject of
Geophysics

THE UNIVERSITY
of ADELAIDE

Submitted to the

Department of Earth Sciences,

School of Physical Sciences, Faculty of Sciences

Adelaide, January 2016

Dedication

To my parents

Lemma Didana and Damench Abebe

without whom none of my success would be possible

CONTENTS

LIST OF TABLES

LIST OF FIGURES

ABSTRACT

This thesis presents magnetotelluric (MT) imaging of the Tendaho conventional geothermal system in the Afar Depression in north eastern Ethiopia and the Habanero Enhanced Geothermal System (EGS) in the Cooper Basin in South Australia. The aims of this dissertation are twofold. The first was to characterize the resistivity structure of the Tendaho conventional geothermal system. This includes delineating fluid pathways and heat sources and determining the connectivity of geothermal localities in the Tendaho field using 2D and 3D resistivity models. The second aim was to investigate the viability of MT to monitor permeability enhancement in an unconventional EGS reservoir during fluid injection using continuous MT measurement at Habanero EGS in the Cooper Basin, South Australia.

The 2D and 3D resistivity models of the Tendaho high temperature field reveal three main resistivity structures to a depth of $20\,\mathrm{km}$. The surface conductive structure (typically $\leq 10\,\Omega\,\mathrm{m}$ and $> 1\,\mathrm{km}$ thick) is interpreted as sediments, geothermal fluids or hydrothermally altered smectite clay. The underlying high resistivity structure is interpreted as Afar Stratoid Series basalts or chlorite-epidote alteration mineralogy. At a depth greater than $5\,\mathrm{km}$, low resistivity is observed across the whole of the Tendaho geothermal field. This structure is inferred to be the heat source of the geothermal system. Based on geochemical and borehole information and a bulk resistivity from the resistivity model, a melt fraction of about 13% by volume has been estimated for the structure. The most striking feature in the 2D and 3D models is a conductive fracture zone in the basalts, which is likely to increase the permeability and temperature of the deep reservoirs in the basalts and provide an upflow zone. Analysis of 3D resistivity models and the geochemistry of geothermal fluids sug-

gests that the Dubti and Ayrobera geothermal localities at the Tendaho field are not connected. The inferred presence of a conductive fracture zone and shallow magma reservoirs make the Tendaho geothermal field a promising prospect for geothermal power development.

An MT survey was conducted at Habanero EGS during stimulation of the Habanero-4 well, where 36.5 ML of water with a resistivity of $13\,\Omega\,\text{m}$ (at 25 ℃) was injected at a relatively continuous rate of between 27–53 L/s into the EGS reservoirs at a depth of 4077 m. Analysis of pre- and post-injection MT responses showed possible conductive fractures oriented in a N/NNE direction. Apparent resistivity maps also revealed that the injected fluids likely propagated towards N/NNE direction. This result is consistent with the propagation direction of the dominant micro-seismic events, as well as the orientation of pre-existing N-S striking sub-horizontal fractures susceptible to slip on stimulation. The MT responses close to the injection point show on average a 5% decrease in apparent resistivity for periods >10 s. The main reasons for detecting only subtle changes in resistivity at the Habanero EGS is the screening effect of the conductive thick sedimentary cover (about 3.6 km thick) and the presence of pre-existing saline fluids with resistivity of $0.1\,\Omega\,\text{m}$ (equivalent to a salinity of 16.1 g/L at 240 ℃) in the natural fractures in the EGS reservoirs. This is further compounded by the physics of the problem, that is, the small volume of injected fluid compared to the large volume averaging by an MT sounding at the depth of interest. For MT sites close to the EGS well, the analysis of time-lapse inversion models indicated an increase in total cumulative conductance of about 25 S over a depth range of 2–5 km in the N-S direction compared to the E-W direction. This likely indicates anisotropic permeability generated by the hydraulic stimulation. Overall, the MT monitoring at Habanero EGS highlights the need for favorable geological settings and/or controlled source methods and down-hole methods to measure significant changes in resistivity in EGS reservoirs.

STATEMENT OF ORIGINALITY

I certify that this work contains no material which has been accepted for the award of any other degree or diploma in my name in any university or other tertiary institution and, to the best of my knowledge and belief, contains no material previously published or written by another person, except where due reference has been made in the text. In addition, I certify that no part of this work will, in the future, be used in a submission in my name for any other degree or diploma in any university or other tertiary institution without the prior approval of the University of Adelaide and where applicable, any partner institution responsible for the joint award of this degree.

I give consent to this copy of my thesis when deposited in the University Library, being made available for loan and photocopying, subject to the provisions of the Copyright Act 1968.

The author acknowledges that copyright of published works contained within this thesis resides with the copyright holder(s) of those works.

I also give permission for the digital version of my thesis to be made available on the web, via the University's digital research repository, the Library Search and also through web search engines, unless permission has been granted by the University to restrict access for a period of time.

_____   _____

Signed   Date

ACKNOWLEDGEMENTS

CHAPTER

ONE

INTRODUCTION

The Intergovernmental Panel on Climate Change (IPCC) reported that it is necessary to replace fossil fuel-based production of energy with renewable energy sources, such as solar, wind, and geothermal, in order to reduce the emissions of carbon dioxide which contributes to climate change (Pachauri et al., 2014). Geothermal energy is a benign renewable energy which is becoming an important contributor to our energy mix with total installed capacity of $12.6\,\mathrm{GW_e}$ worldwide in 2015 (Bertani, 2015). It provides baseload electricity, which most other renewable energy sources are not able to provide. For instance, wind and solar are dependent on environmental variables.

Traditionally, geothermal energy is produced in areas with active tectonic settings, which are referred to as convection-dominated (conventional hydrothermal) geothermal systems (Moeck, 2014). Countries that produce energy from this type system include the USA, Philippines, Indonesia, Mexico, New Zealand and Iceland (Figure 1.1). These systems require a heat source, a permeable reservoir, a confining impermeable cap rock and a recharge (fluid source) to be economically exploited (DiPippo, 2012; Muñoz, 2014).

In contrast, conduction-dominated (unconventional) geothermal systems occur in regions characterized as being tectonically passive (DiPippo,
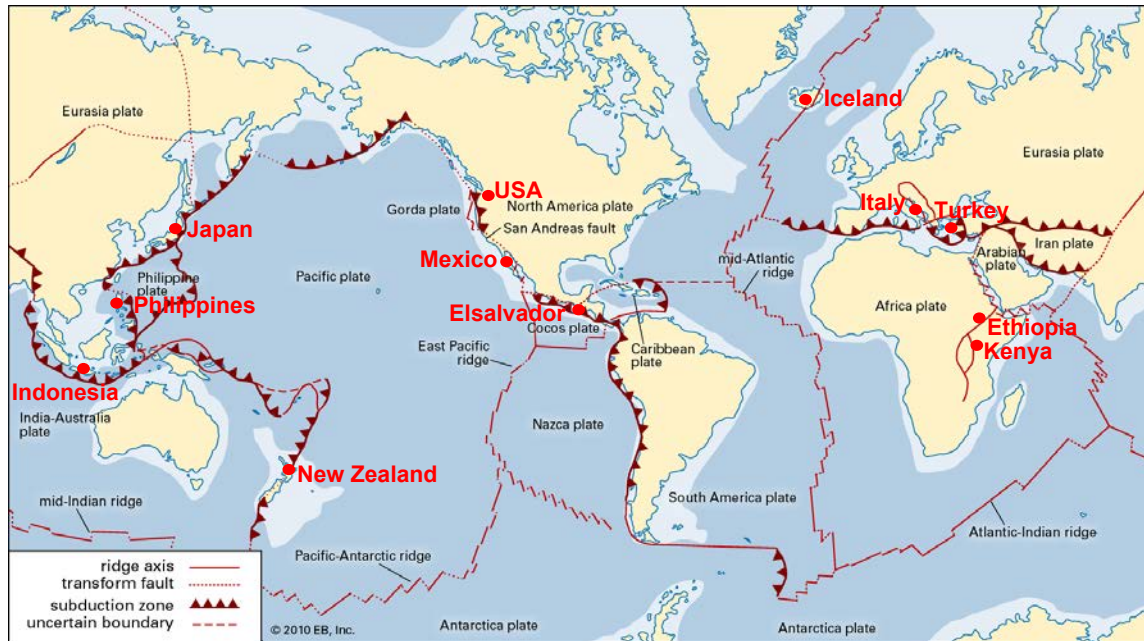
Figure 1.1: Examples of locations producing geothermal power from conventional geothermal systems. The geothermal systems lie close to active tectonic settings (divergent, convergent or transform boundaries) (modified from Britannica (2015)).

2012; Moeck, 2014). These systems include Enhanced Geothermal Systems (EGS) and hot sedimentary aquifers. Enhanced Geothermal Systems are unconventional geothermal resources with low permeability and relatively high temperature, which require hydraulic stimulation to enhance fracture connectivity (Audigane et al., 2002; Evans et al., 2005; Tester et al., 2006; Muñoz, 2014; McMahon and Baisch, 2015). In recent years significant advances have been made in evaluating the viability of EGS for the production of power around the world. These include the Cooper Basin in Australia (Bendall et al., 2014), Soultz in France (Baria et al., 2004; Gérard et al., 2006; Cuenot et al., 2008; Genter et al., 2010; DiPippo, 2012) and Newberry in the USA (Cladouhos et al., 2013). A typical EGS system consists of an injection well, which sends cold surface water to the hot EGS reservoirs at depth; and a production well, which brings heated water from the reservoirs to the surface (Figure 1.2). These systems are hydraulically stimulated to improve circulation.

Electromagnetic (EM) methods are commonly applied to investigate the resistivity structures of high temperature geothermal systems (Spichak and Manzella, 2009; Muñoz, 2014). Electromagnetic methods are sen-
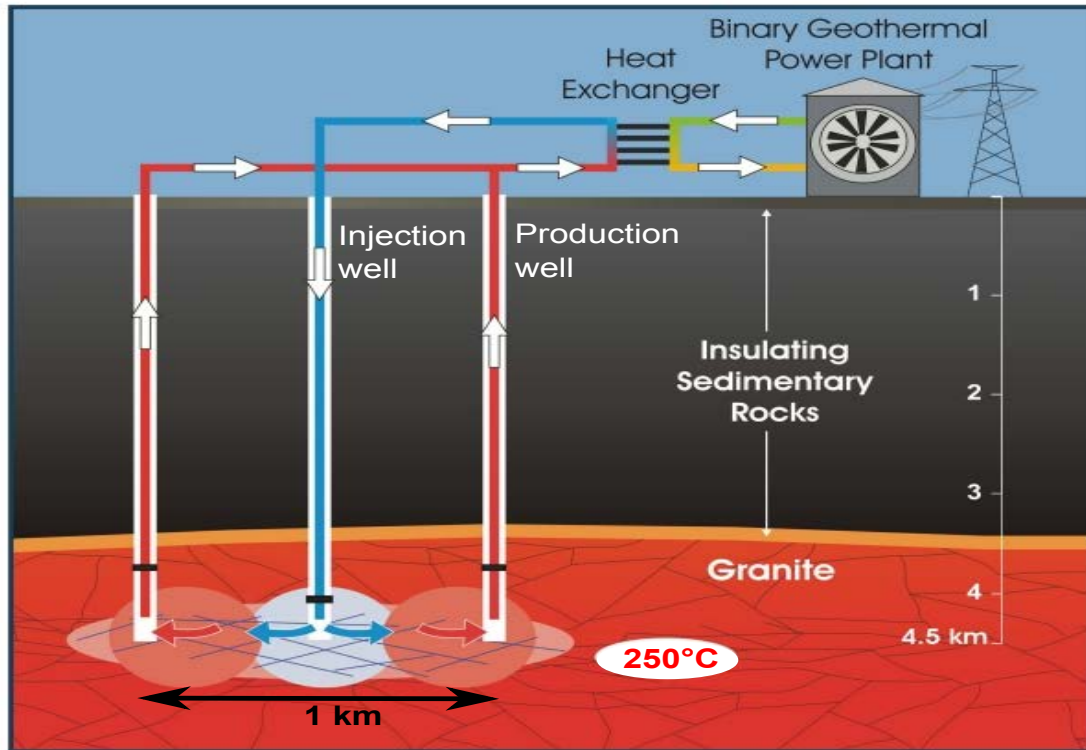
Figure 1.2: Schematic plot of Cooper Basin EGS project in South Australia. During a closed-loop test, the hot brine produced by the production well is re-injected into the injection well after heating the working fluid in the heat exchanger of the EGS pilot power plant (modified from Katusa and Bustin (2009)).

sitive to conductivity variations resulting from geothermal alteration of minerals, the presence of saline fluids, partial melting and high temperatures (Spichak and Manzella, 2009; Muñoz, 2014).

High frequency EM methods such as Transient Electromagnetics (TEM) and Controlled Source Electromagnetics (CSEM) are used to explore shallow geothermal resources ($<1\,$km), whereas magnetotellurics (MT) is used to investigate deep geothermal resources (Spichak and Manzella, 2009; Árnason et al., 2010; Cumming and Mackie, 2010).

The resistivity structures of conventional high temperature geothermal systems are predominantly controlled by their associated alteration mineralogy (Anderson et al., 2000; Ussher et al., 2000; Cumming, 2009; Árnason et al., 2010). These are typically characterized by a conductive smectite-zeolite alteration clay cap at temperatures of 70-150 ℃ underlain by a moderately resistive geothermal reservoir which is made up of
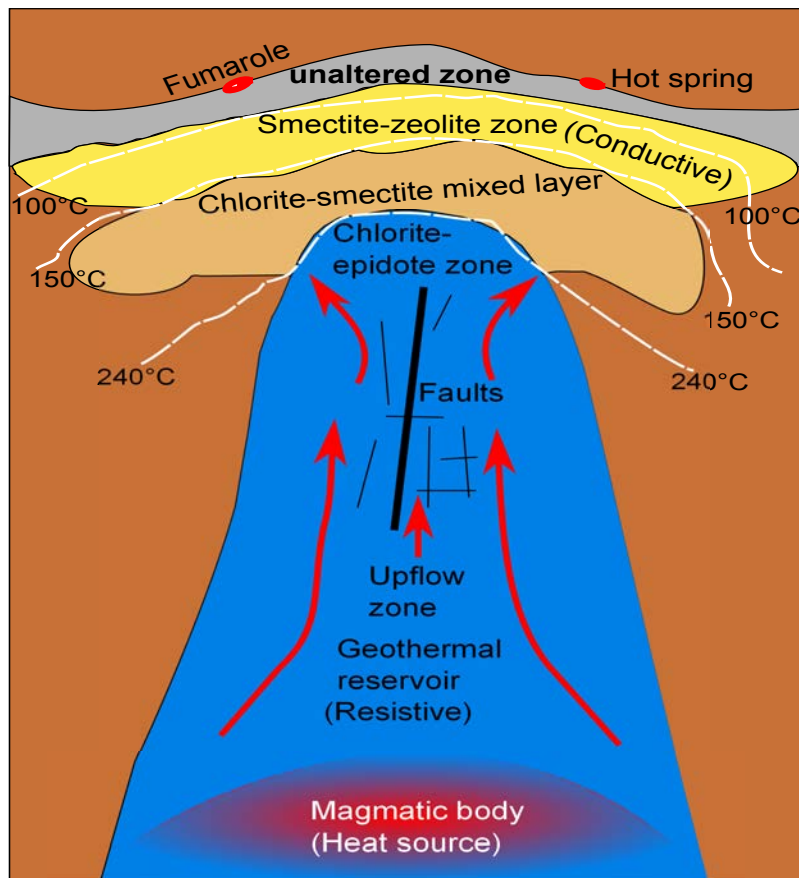
Figure 1.3: Conceptual resistivity model of conventional high temperature systems (redrawn from Pellerin et al. (1996)).

high temperature alteration minerals which include chlorite, ellite and epidote, etc. at temperatures of 220-240 ℃ (Pellerin et al., 1996; Anderson et al., 2000; Ussher et al., 2000; Árnason et al., 2010) (Figure 1.3). The resistivity structure helps in defining possible drilling targets in conjunction with other geoscientific data. Interestingly, the alteration mineralogy does not necessarily reflect the temperatures measured in the wells, for example cooling may occur in the reservoir formation (Árnason et al., 2010). Other conventional systems, as those characterized by Volpi et al. (2003) and Oskooi and Manzella (2011) in the Larderello high temperature geothermal field in Italy, have different resistivity structures with a low resistivity characterized as the geothermal reservoir in fractured metamorphic host rocks.

Three dimensional (3D) resistivity models of geothermal areas are essential to delineate the complex geology of deep geothermal reservoirs generated by hydrothermal circulation and alteration of rocks (Heise et al., 2008; Newman et al., 2008; Spichak and Manzella, 2009; Árnason et al., 2010; Cumming and Mackie, 2010; Bertrand et al., 2012; Gasperikova et al., 2015). In addition, integration of resistivity models with other geophysical data (for example, seismic velocity and gravity data), geochemical, geological and petrophysical information is important to understand the nature of the reservoir and avoid misinterpretation of electrical resistivity data (Wright et al., 1985; Bibby et al., 2005; Cumming, 2009; Muñoz, 2014). Newman et al. (2008) used MT and seismic velocity data to characterize the Coso geothermal field in California. They interpreted a low resistivity and high seismic velocity ratio (v_p/v_s) at a depth of 1.2 km as fluid saturation or high temperature (greater than 250 ℃) (Lees and Wu, 2000; Newman et al., 2008). Similarly, Wamalwa et al. (2013) interpreted low resistivity and low density zones at a depth of about 6 km at Coso geothermal field as partially molten magmatic rocks.

In an unconventional geothermal system, geophysical methods such as micro-seismics and MT can be used to monitor hydraulic stimulation of EGS reservoirs (Baria et al., 2004; Bedrosian et al., 2004; Cuenot et al., 2008; Cladouhos et al., 2013; Peacock et al., 2013; Baisch et al., 2015). The main geophysical method used to monitor fractures opening during hydraulic stimulation of EGS is micro-seismics (House, 1987; Wohlenberg and Keppler, 1987; Audigane et al., 2002; Baria et al., 2004; Cuenot et al., 2008; Cladouhos et al., 2013; Baisch et al., 2015). However, this method does not provide information about fluid movement in the connected fractures (Cladouhos et al., 2013). Magnetotellurics has been used to image enhanced electrical conductivity in fluid-filled fractures in EGS reservoirs to a depth of 3-5 km (Geiermann and Schill, 2010; Peacock et al., 2012, 2013; MacFarlane et al., 2014; Kirkby et al., 2015). Peacock et al. (2012) and Peacock et al. (2013) used MT for monitoring the injection of 3.1 ML of saline fluids into an EGS reservoir at a depth of 3.6 km at Paralana, South Australia, over a period of 4 days. The MT responses from the pre- and post-injection data showed an average decrease of 10% and 5% in the xy and yx components of

apparent resistivity, respectively (Peacock, 2012; Peacock et al., 2013). Furthermore, using residual phase tensor analysis, Peacock et al. (2013) demonstrated that the injected fluids propagated along pre-existing fault system oriented in a NNE direction. The micro-seismic survey conducted at Paralana EGS showed fractures opened in a NNE, NE, and ENE direction along pre-existing fault systems (Hasting et al., 2011; Albaric et al., 2014). These studies showed the complementarity of MT and micro-seismics in characterizing fluid injection into EGS reservoirs.

Bedrosian et al. (2004) also conducted MT monitoring studies around a natural gas exploration well in the North German Basin during hydraulic stimulation at a depth of 4 km for geothermal exploration purposes. The 2D MT models did not recover changes in subsurface resistivity following the fluid injection because of low data quality (low-signal-noise ratio) (Bedrosian et al., 2004). The time-lapse changes in the MT response can be modeled to image the reservoir as demonstrated by Rosas-Carbajal et al. (2015) using 3D probabilistic inversions.

1.1 Aims and Objectives

The aims of this dissertation are twofold. The first is to characterize the geothermal reservoir characteristics geophysically in a conventional hydrothermal geothermal system. These include specifically delineating possible fluid pathways (upflow zone) and heat sources and determining the connectivity of geothermal localities in a geothermal field using 2D and 3D resistivity models. Then, use a combination of geophysical, geological, geochemical and borehole information to characterize a conventional geothermal system. These objectives will be examined by using a 3D broadband MT array data from a conventional high temperature geothermal field.

The second aim is to investigate the viability of MT for monitoring permeability enhancement resulting from fluid injection into an unconventional EGS reservoir. To achieve this objective, a 4D broadband MT array data will be used to map spatial (volumetric) and temporal variations of bulk resistivity resulting from hydraulic stimulation.

The outcome will give a new constraints on permeability for conventional and unconventional systems and will aid in optimization of geothermal resource development.

1.2   Outline

This thesis is presented in six chapters, with this introduction being the first chapter. Chapter 2 provides a brief overview of the MT method including the basics of MT theory, phase tensors analysis and crustal partial melt fraction estimation. Chapter 3 describes 2D modeling results from the Tendaho high temperature geothermal field. This work has been published in *Geophysical Research Letters*. Chapter 4 describes 3D inversion results from the Tendaho high temperature geothermal field. This work has been published in the *Journal of Volcanological and Geothermal Research*. Chapter 5 describes the time-lapse MT monitoring at Habanero EGS and has been submitted to the *Journal of Geophysical Research: Solid Earth*. Chapter 6 provides an overall summary of the dissertation and discusses lessons learned and make concluding remarks.

MAGNETOTELLURIC METHOD

2.1   Introduction

Magnetotellurics (MT) is a passive electromagnetic method that makes use of a broad spectrum of the naturally occurring geomagnetic varia- tions as a source for electromagnetic (EM) induction in the Earth. The MT technique involves measuring fluctuations in the natural electric (**E**) and magnetic (**H**) fields in orthogonal directions on the Earth's sur- face, as a means of determining its internal resistivity structure (Chave and Jones, 2012). MT sounding as a method of studying the vertical variations in the electrical resistivity of the Earth was first designed by Tikhonov (1950), Rikitake (1951) and Cagniard (1953). A measure of the penetration depth (or skin depth) of diffusing EM fields into the Earth depends on the bulk resistivity of the medium and the period of the signal, which is given by:

$$\delta(T) = \sqrt{\frac{T\rho}{\pi\mu}} \tag{2.1}$$

where $\delta(T)$ is the depth in meters at which the EM fields amplitude are attenuated to e^{-1} (~ 37%) of their amplitude at the surface of the Earth at a given period T, ρ is the bulk resistivity of the medium in $\Omega\,m$ and μ is the magnetic permeability. using $\mu = 4\pi \times 10^{-7} Hm^{-1}$ for free space, this equation can be written as

$$\delta(T) \approx 500\sqrt{T\rho}\,(\mathrm{m})$$

The MT method utilizes global lightening discharges with frequencies predominately above $1\,\mathrm{Hz}$, and interactions between the solar plasma and the Earth's magnetic field with frequencies predominately below $1\,\mathrm{Hz}$ as source signals (Simpson and Bahr, 2005).

2.2 MT theory

2.2.1 EM field equations

The behavior of EM fields for a magnetizable medium can be described by Maxwell's equations in differential form:

$$\nabla \times \vec{E} = -\frac{\partial \vec{B}}{\partial t} \tag{2.2a}$$

$$\nabla \times \vec{H} = \vec{J} + \frac{\partial \vec{D}}{\partial t} \tag{2.2b}$$

$$\nabla \cdot \vec{B} = 0 \tag{2.2c}$$

$$\nabla \cdot \vec{E} = \eta/\epsilon \tag{2.2d}$$

where $\vec{E}$ is the electric field (Vm^{-1}), $\vec{B}$ is the magnetic flux density or magnetic induction (T), $\vec{H}$ is the magnetic intensity or magnetic field (Am^{-1}), $\vec{D}$ is the electric displacement (Cm^{-2}), η is the electric volume charge density of free charges (Cm^{-3}), $\vec{J}$ is the electric current density of free charges (Am^{-2}) and ϵ is the electric permittivity (F/m).

Equation (2.2a) is Faraday's Law and states that a rotating electric field is produced by a magnetic field that changes with time. Equation (2.2b) is Ampere's Law and states that a circulating magnetic field is generated by an electric current and by an electric field that changes with time. Equation (2.2c) is Gauss's Law for magnetic fields and states that no free magnetic charges (or monopoles) exist, and that all magnetic fields are conservative. Equation (2.2d) is Gauss's Law for electric fields and states that the electric field generated by electric charges diverges from a positive charge and converges upon a negative charge.

For a linear isotropic medium, the following constitutive relationships hold:

$$\vec{B} = \mu \vec{H} \tag{2.3}$$

$$\vec{D} = \epsilon \vec{E} \tag{2.4}$$

$$\vec{J} = \sigma \vec{E} \tag{2.5}$$

where σ is the electrical conductivity (Sm^{-1}) which is the reciprocal of electrical resistivity ρ and μ is the magnetic permeability (H/m). σ, ϵ

and μ describe intrinsic properties of the materials through which the EM fields propagate.

The MT method is based on the diffusion of EM energy into the Earth. The three main assumptions for electromagnetic induction in the Earth include (Simpson and Bahr, 2005): (1) Time-varying displacement currents are negligible compared with time-varying conduction currents (a quasi-static approximation). (2) A uniform plane EM wave with source far away from the Earth is assumed. After striking the Earth, the EM fields propagate vertically into the Earth because of the large resistivity contrast at the air-Earth interface. (3) No free charges can accumulate within a layered Earth. Charges can accumulate along discontinuities which cause non-inductive static shifts.

Re-writing equations (2.2a) and (2.2b) using the constitutive relationships and assuming the time dependence $e^{-i\omega t}$ of the fields, with angular frequency $\omega = 2\pi/T$ gives:

$$\nabla \times \vec{E} = -\frac{\partial \vec{B}}{\partial t} = i\omega\mu\vec{H} \tag{2.6}$$

$$\nabla \times \vec{H} = J + \frac{\partial \vec{D}}{\partial t} = (\sigma - i\omega\epsilon)\vec{E} \tag{2.7}$$

Taking the curl of both of these equations, and substituting the values of equations (2.7) and (2.6), yields:

$$\nabla \times \nabla \times \vec{E} = i\omega\mu(\nabla \times \vec{H}) = i\omega\mu(\sigma - i\omega\epsilon)\vec{E} \tag{2.8}$$

$$\nabla \times \nabla \times \vec{H} = (\sigma - i\omega\epsilon)i\omega\mu\vec{H} \tag{2.9}$$

Using the Helmholtz vector identity $\nabla \times \nabla \times \vec{A} = -\nabla^2\vec{A} + \nabla(\nabla \cdot \vec{A})$ and noting that $\nabla \cdot \vec{E} = 0$ for a homogeneous conducting medium with no free charges, equation (2.8) becomes:

$$\nabla \times \nabla \times \vec{E} = -\nabla^2\vec{E} = i\omega\mu(\sigma - i\omega\epsilon)\vec{E}$$

$$\nabla^2\vec{E} + i\omega\mu(\sigma - i\omega\epsilon)\vec{E} = 0 \tag{2.10}$$

In the same way, equation (2.9) can be written as

$$\nabla \times \nabla \times \vec{H} = -\nabla^2\vec{H} = i\omega\mu(\sigma - i\omega\epsilon)\vec{H}$$

$$\nabla^2 \vec{H} + i\omega\mu(\sigma - i\omega\epsilon)\vec{H} = 0 \qquad (2.11)$$

Equations (2.10) and (2.11) are in the form of the vector Helmholtz partial differential equation:

$$\nabla^2 \vec{A} + k^2 \vec{A} = 0 \qquad (2.12)$$

where k is the propagation constant in the medium.

$$k^2 = i\omega\mu\sigma + \omega^2\mu\epsilon = \omega\mu(i\sigma + \omega\epsilon) \qquad (2.13)$$

where σ, μ and ϵ are the uniform conductivity, permeability and permittivity of the medium, respectively, and ω is the angular frequency.

For MT method, variations in ϵ and μ of rocks are generally negligible compared to variations in bulk conductivities and free space values of $\epsilon_o = 8.85 \times 10^{-12}$ F/m and $\mu_o = 1.2566 \times 10^{-6}$ H/m^{-1} are assumed. A typical value of bulk conductivity of subsurface rocks is usually in the range of $\sigma \approx 10^{-4} - 10^0$ S/m. The frequencies used in MT studies are between $f \approx 10^4 - 10^{-4}$ Hz. Taking permittivity of free space $\epsilon_o = 8.85 \times 10^{-12}$ F/m and dielectric susceptibilities of earth materials χ_e in the range 1–100, the maximum value of the product $\omega\epsilon$ in equation (2.13) is

$$(\omega\epsilon)_{max} = 2\pi f \epsilon_o \chi_e \approx 5 \cdot 10^{-5} \qquad (2.14)$$

This indicates that $\sigma \gg \omega\epsilon$ and a quasi-static approximation can be applied in equation (2.13). Hence, the wave propagation k in equation (2.13) reduces to

$$k^2 = i\omega\mu_o\sigma \qquad (2.15)$$

and equation (2.12) reduces to the diffusion equation, which describes the diffusion of EM fields in the medium:

$$\nabla^2 \vec{A} + i\omega\mu_o\sigma\vec{A} = 0 \qquad (2.16)$$

Therefore, equations (2.10) and (2.11) can be re-written as

$$\nabla^2 \vec{E} + i\omega\mu_o\sigma\vec{E} = 0 \qquad (2.17)$$

$$\nabla^2 \vec{H} + i\omega\mu_o\sigma\vec{H} = 0 \qquad (2.18)$$

When a wave is propagating in the vertical direction as uniform plane wave, there is no variation of electric and magnetic fields with respect to the horizontal directions, i.e. $\frac{\partial}{\partial x}=0$ and $\frac{\partial}{\partial y}=0$ and the vertical electric field is $E_z = 0$. The differential forms of equations (2.6) and (2.7) assuming quasi-static approximation are:

$$\frac{\partial E_x}{\partial z} = i\omega\mu_o H_y \tag{2.19}$$

$$\frac{\partial H_y}{\partial z} = -\sigma E_x \tag{2.20}$$

Differentiating equations 2.19 and 2.20 with respect to z, yields

$$\frac{\partial^2 E_x}{\partial z^2} = i\omega\mu_o\frac{\partial H_y}{\partial z} = -i\omega\mu_o\sigma E_x = -k^2 E_x \tag{2.21}$$

$$\frac{\partial^2 H_y}{\partial z^2} = -\sigma\frac{\partial E_x}{\partial z} = -i\omega\mu_o\sigma H_y = -k^2 H_y \tag{2.22}$$

The general solutions for equations 2.21 and 2.22 are in the form:

$$E_x = A\mathrm{e}^{-ikz} + B\mathrm{e}^{ikz} \tag{2.23}$$

$$H_y = \frac{k}{\omega\mu_o}\left(A\mathrm{e}^{-ikz} - B\mathrm{e}^{ikz}\right) \tag{2.24}$$

Only the component of the solution which is exponentially decaying is relevant to MT studies as the EM signal energy decreases with depth.

2.2.2   Impedance tensor, Dimensionality, and Tipper

The complex impedance tensor ($\mathbf{Z}$) describes the relation between the electric ($\mathbf{E}$) and magnetic ($\mathbf{H}$) fields is given by

$$\begin{pmatrix} E_x \\ E_y \end{pmatrix} = \begin{pmatrix} Z_{xx} & Z_{xy} \\ Z_{yx} & Z_{yy} \end{pmatrix} \begin{pmatrix} H_x \\ H_y \end{pmatrix} \tag{2.25}$$

Using the field equations for the propagation in a uniform space, equations (2.23) and (2.24), the impedance within a uniform half space is given by

$$Z = \frac{E}{H} = \frac{\omega\mu_o}{k} \tag{2.26}$$

The apparent resistivity ρ_a for non-uniform Earth is defined by:

$$\rho_a = \frac{1}{\mu_o \omega} |Z|^2 \tag{2.27}$$

Correspondingly, the phase ϕ of the complex impedance tensor is given by:

$$\phi = \tan^{-1}\left(\frac{\text{Im}(Z)}{\text{Re}(Z)}\right) \tag{2.28}$$

One dimensional (1D) resistivity model is a model in which the resistivity varies with depth only, i.e. $\rho = \rho(z)$. For a 1D Earth, $Z_{xx}=Z_{yy}=0$ and $Z_{xy}=-Z_{xy}$.

Two dimensional (2D) resistivity models are models in which the resistivity is constant in one horizontal direction while changing in the vertical and other horizontal direction. The geoelectric strike (electromagnetic strike) is the direction along which the conductivity is constant in a 2D Earth. For a 2D Earth, $Z_{xx}=-Z_{yy}$ and $Z_{xy} \neq -Z_{yx}$. Two independent modes of the impedance are defined for 2D Earth models with x parallel to the geoelectric strike on a Cartesian coordinate system. The component of impedance with electric field parallel to geoelectric strike is the transverse electric (TE) mode and the component of impedance with magnetic field parallel to strike is the transverse magnetic (TM) mode. The impedance elements are rotated to the geoelectric strike direction in which $Z_{x'x'}=Z_{y'y'} = 0$ before 2D inversions.

Three dimensional (3D) resistivity models are models where resistivity changes in all directions, i.e $\rho = \rho(x,y,z)$. For a 3D Earth, all the components of the impedance tensor are non-zero, that is, $Z_{xx} \neq Z_{yy}$ and $Z_{xy} \neq Z_{yx}$ and does not show any symmetry.

The induction vector (Tipper) τ is a complex vector describing the relationship between the horizontal ($\mathbf{H_x}$ and $\mathbf{H_y}$) and the vertical($\mathbf{H_z}$) magnetic field components,

$$\mathbf{H_z} = \tau_{zx}\mathbf{H_x} + \tau_{zy}\mathbf{H_y} \tag{2.29}$$

For a 2D structure with strike in the x direction, equation (2.29) becomes

$$\mathbf{H_z} = \tau_{zy}\mathbf{H_y} \tag{2.30}$$

In the 2D Earth, the tipper is perpendicular to the strike direction. For a 1D structure, $\tau=0$.

Parkinson induction arrows are graphical representation of the tipper components τ_{zx} and τ_{zy} (Parkinson, 1962). In the Parkinson convention, the tipper vectors point towards a conductive body (Parkinson, 1959). Parkinson arrows have a real (in-phase) and quadrature (out-of-phase) parts. Length of the real (M_r) and quadrature (M_q) arrows are given by

$$M_r = \sqrt{\Re\tau_{zx}^2 + \Re\tau_{zy}^2} \tag{2.31}$$

$$M_q = \sqrt{\Im\tau_{zx}^2 + \Im\tau_{zy}^2} \tag{2.32}$$

The orientation of the arrows is determined by

$$\theta_r = \tan^{-1}\left(\frac{\Re\tau_{zy}}{\Re\tau_{zx}}\right) \tag{2.33}$$

$$\theta_q = \tan^{-1}\left(\frac{\Im\tau_{zy}}{\Im\tau_{zx}}\right) \tag{2.34}$$

2.3 Phase tensor analysis

MT data require directionality and dimensionality analysis of the regional resistivity structure before any modeling and inversion of the data. For example, 3D MT data modeled using 2D inversions could result in misinterpretation of resistivity structure under the survey area. Furthermore, the analysis of the data can be hampered by distortion in the MT data. Distortion in MT data is a phenomena caused by the presence of shallow local bodies or heterogeneites, which are much smaller than the target of interest and skin depths (Bahr, 1988; Jiracek, 1990). The phase tensor (Φ) is a property of impedance tensor ($\mathbf{Z}$) that is unaffected by electric field galvanic distortion (Caldwell et al., 2004; Bibby et al., 2005;

Booker, 2014). Therefore, it is an important tool for the analysis of MT data.

The phase tensor is the ratio of the imaginary ($\mathbf{Y}$) and the real ($\mathbf{X}$) parts of the impedance tensor as defined in Caldwell et al. (2004).

$$\Phi = \mathbf{X}^{-1}\mathbf{Y} = \begin{bmatrix} \Phi_{xx} & \Phi_{xy} \\ \Phi_{yx} & \Phi_{yy} \end{bmatrix}, \mathbf{Z} = \mathbf{X} + i\mathbf{Y} \tag{2.35}$$

where $\mathbf{X}^{-1}$ is the inverse of $\mathbf{X}$.

Caldwell et al. (2004) defines three tensor invariants from the matrix of phase tensors in equation 2.35, namely the trace, determinant and skew,

$$\Phi_1 = \frac{\Phi_{xx} + \Phi_{yy}}{2} \qquad \text{Trace} \tag{2.36}$$

$$\Phi_2 = \Phi_{xx}\Phi_{yy} - \Phi_{xy}\Phi_{yx} \qquad \text{Determinant} \tag{2.37}$$

$$\Phi_3 = \frac{\Phi_{xy} - \Phi_{yx}}{2} \qquad \text{Skew} \tag{2.38}$$

Four coordinate system invariants defined in Caldwell et al. (2004) include the maximum (Φ_{max}) and the minimum (Φ_{min}) principal phases, the skew angle (β) and the azimuth angle (α). The four invariants of the phase tensor (Caldwell et al., 2004) in terms of the parameters of an ellipse (Figure 2.1) are given by

$$\Phi_{min} = \left(\Phi_1^2 + \Phi_3^2\right)^{1/2} - \left(\Phi_1^2 + \Phi_3^2 - \Phi_2^2\right)^{1/2} \tag{2.39}$$

$$\Phi_{max} = \left(\Phi_1^2 + \Phi_3^2\right)^{1/2} + \left(\Phi_1^2 + \Phi_3^2 - \Phi_2^2\right)^{1/2} \tag{2.40}$$

$$\beta = \frac{1}{2}\tan^{-1}\left(\frac{\Phi_3}{\Phi_1}\right) = \frac{1}{2}\tan^{-1}\left(\frac{\Phi_{xy} - \Phi_{yx}}{\Phi_{xx} + \Phi_{yy}}\right) \tag{2.41}$$

$$\alpha = \frac{1}{2}\tan^{-1}\left(\frac{\Phi_{xy} + \Phi_{yx}}{\Phi_{xx} - \Phi_{yy}}\right) \tag{2.42}$$

where α is the angle between the reference axis and the coordinate axis.
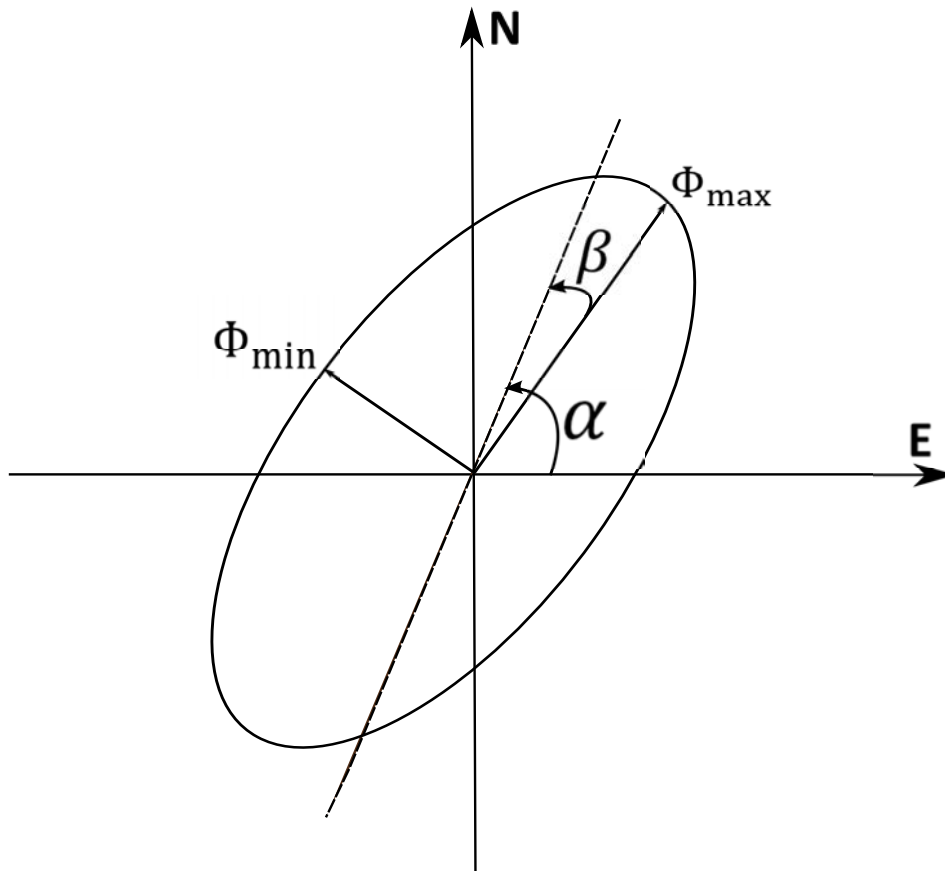
Figure 2.1: Plot of the phase tensor as an ellipse (Caldwell et al., 2004). The lengths of the semi-major and semi-minor axes are Φ_{max} and Φ_{min}, which represent the principal axes of the tensor. The azimuth of the major axis is defined by $\alpha - \beta$. The angle α is measured counterclockwise from East.

Bibby et al. (2005) defines ellipticity (λ), which is a measure of dimensionality as

$$\lambda = \frac{[(\Phi_{xx} - \Phi_{yy})^2 + (\Phi_{xy} + \Phi_{yx})^2]^{1/2}}{[(\Phi_{xx} + \Phi_{yy})^2 + (\Phi_{xy} - \Phi_{yx})^2]^{1/2}} \qquad (2.43)$$

For a perfect 1D structure, $\beta = 0$ and $\lambda = 0$ and $\Phi_{min} = \Phi_{max}$ (a circle). A threshold value of less than 0.2 is used for λ for a 1D real field MT data. For a perfect 2D structure, $\beta = 0$ and one of the principal axes of the phase tensor ellipse is in the strike direction. For 3D structure, all the invariants are non-zero, that is, $\beta \neq 0, \Phi_{min} \neq 0$ and $\Phi_{max} \neq 0$.

A typical example of plots of phase tensor elements for an MT site from the Habanero EGS is given in Figure 2.2.
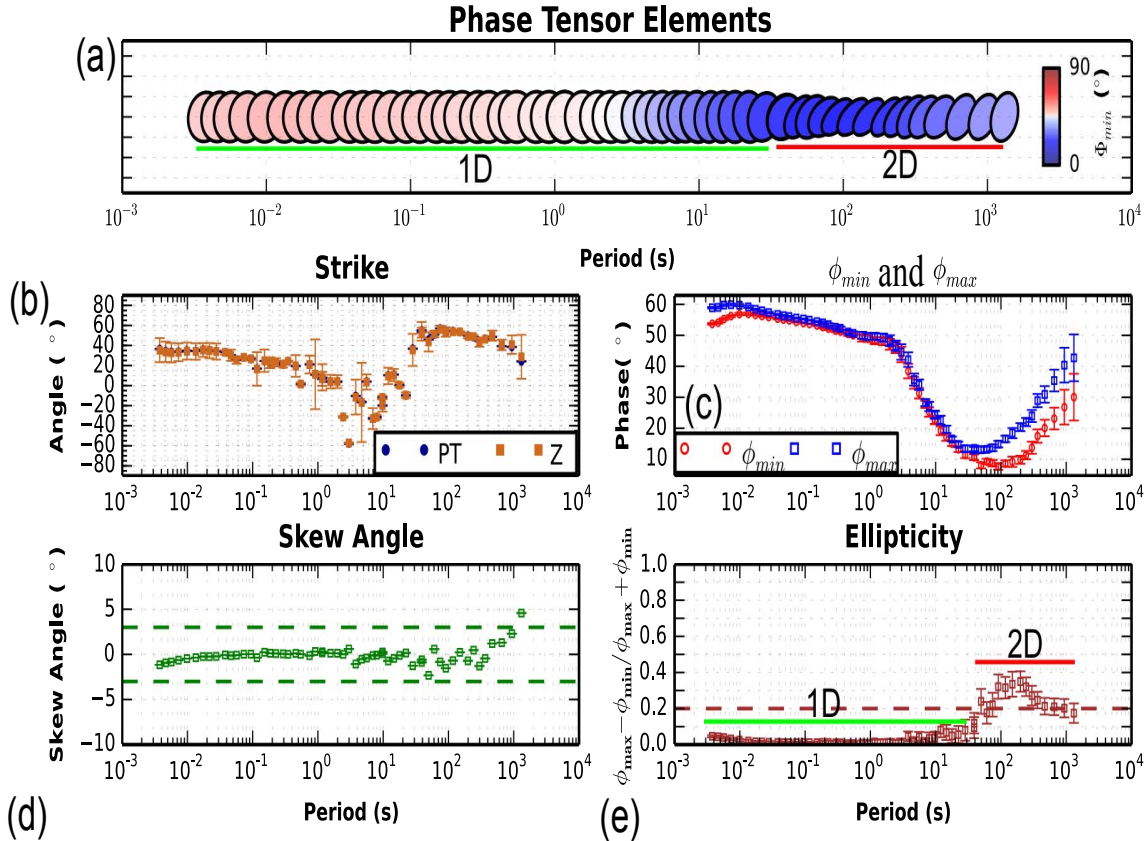
Figure 2.2: An example of plot of phase tensor elements for an MT site from Habanero EGS (Caldwell et al., 2004). (a) Phase tensor plot for periods between 0.003 s-1000 s showing 1D and 2D structures coloured by minimum phase. (b) strike angles estimated from azimuth ($\alpha - \beta$) of phase tensor (PT) (Caldwell et al., 2004) and the invariants of the impedance tensor (Z) (Weaver et al., 2000). (c) maximum (blue squares) and minimum (red circles) phases of phase tensor. (d) skew angles with values less than three degrees show 1D/2D structure. (d) Ellipticity shows 1D structure for periods in the range from 0.003 s-40 s.

Uncertainties of phase tensor parameters can be calculated from impedance and impedance error by propagation of errors and statistical evaluation (Booker, 2014). A large number of phase tensor parameters are generated from the values of impedance Z and its uncertainties in this study. An example of an uncertainty plot of the orientation of the major axis of the ellipse in terms of the angles α and β is given in Figure 2.3.
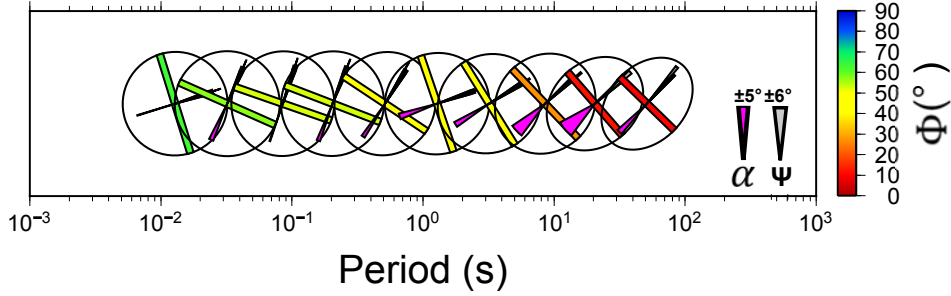
Figure 2.3: Uncertainty plot of phase tensor crosses at selected periods for an MT site from Habanero EGS. The uncertainty in the orientation of the major axis (α) is shown by downward pointing magenta fans. An uncertainty fan with ±5° width is shown at bottom right corner for scale. The uncertainty in normalized skew angles ($\Psi{=}2\beta$) is represented by gray fans. An uncertainty with ±6° is shown at bottom right corner for scale. The map shows the uncertainty in the orientation of the major axis (α) of the phase tensor ellipses increases near the dead band due to low signal-to-noise ratio. The color of the ellipses minor axis indicates the minimum principal phase.

The residual phase tensors ($\Delta\Phi_{12}$) between pre- and post- injection measurements are calculated as (Peacock et al., 2013; Booker, 2014)

$$\Delta\Phi_{12} = \Phi_2 - \Phi_1 \tag{2.44}$$

where Φ_2 and Φ_1 are the phase tensors post-injection and pre-injection, respectively.

Plots of residual Phase tensor ellipses help in identifying the direction of maximum change in conductivity resulting from hydraulic stimulation (Peacock et al., 2013; Booker, 2014). The magnitudes of the change in conductivity are represented by the major ($\Delta\Phi_{max}$) and minor ($\Delta\Phi_{min}$) axes of the ellipse. The major axis of the ellipse indicate the direction of the maximum change in conductivity. The face color of the ellipse is calculated as the geometric mean of $\Delta\Phi_{max}$ and $\Delta\Phi_{min}$ which gives the percentage change between two sets of MT measurements. An example of plots of residual phase tensor from MT monitoring survey at the Habanero EGS is given in Figure 2.4. Equation (2.44) can also be used to calculate the misfit tensor between the observed and predicted phase tensors to assess modeling results (Heise et al., 2007; Booker, 2014).
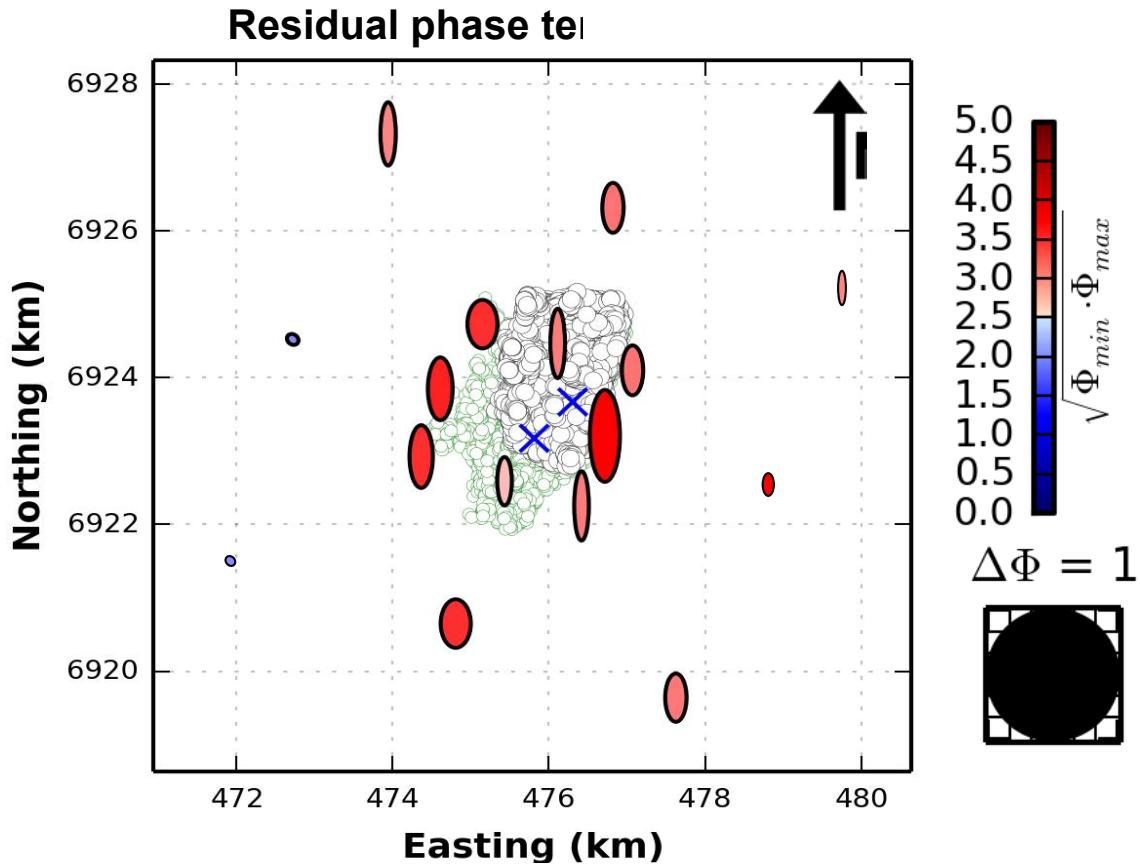
Figure 2.4: Map of phase tensor residuals between pre- and post-stimulation measurements 17 s. The magnitudes of the change in conductivity are represented by the major ($\Delta\Phi_{max}$) and minor ($\Delta\Phi_{min}$) axes of the ellipse. The ellipses are colored by percentage of the geometric mean of change in maximum and minimum phases. The ellipses are normalized by the maximum value of Φ_{max} for the data set. The green and black blobs at the background represent the seismic cloud from micro-seismic data collected during stimulation of the Habanero EGS wells shown by blue × symbols.

2.4   Enhanced crustal conductivity

The purpose of this section is to describe possible causes of enhanced conductivity in the crust in high temperature geothermal systems and ways of estimating volume of partial melt using geophysical, geochemical and borehole information.

Enhanced conductivity in the Earth's crust is associated with saline fluids, clay alteration minerals, metallic minerals and partial melts (Chave and Jones, 2012; Muñoz, 2014). The presence of magma chambers in the lower crust or deep mantle magma sources make partial melts a plausible candidate to explain the high conductivity observed at conventional

high temperature geothermal system in active tectonic settings (Spichak and Manzella, 2009; Pommier and Le-Trong, 2011; Muñoz, 2014). The conductivity of a partial melt depends on its composition, temperature, water content and to less extent on pressure (Tyburczy and Waff, 1983; Li et al., 2003). Using temperature, pressure, SiO_2 and Na_2O, and water content of the melt as input parameters, the web-based application "SIGMELTS" can be used to determine the conductivity of the partial melt (Pommier and Le-Trong, 2011). For the partial melt to enhance conductivity, it must form an interconnected network within the rock matrix (Sato and Ida, 1984; Roberts and Tyburczy, 1999). This requires assumptions regarding the distribution of melts within the host rock before the volume of the melt fraction is estimated.

The bulk conductivity and melt conductivity are related through mixing relationships to determine the volume fraction of melt (Roberts and Tyburczy, 1999). There are many mixing models of two-phase mixture (Roberts and Tyburczy, 1999). The simplest mixing models for the electrical conductivity of a two-phase mixture are the series and parallel models (Roberts and Tyburczy, 1999). The series and parallel models yield maximum and minimum estimates of melt fraction, respectively. Their respective conductivities σ_s and σ_p are

$$\sigma_s{}^{-1} = \frac{x_m}{\sigma_m} + \frac{x_r}{\sigma_r} \tag{2.45}$$

$$\sigma_p = \sigma_m x_m + \sigma_r x_r \tag{2.46}$$

where σ_s is the series conductivity, σ_p is the parallel conductivity, σ_m and σ_r are the conductivities of the melt and host rock, respectively, and x_m and x_r are the respective volume fractions. The Hashin-Shtrikman upper bound model (Hashin and Shtrikman, 1962) assumes interconnected melts with isolated matrix grains which produce higher estimates than the parallel conduction model. The conductivity of Hashin-Shtrikman upper bound (σ_{HS^+}) of two-phase mixture is given by

$$\sigma_{HS^+} = \sigma_m + x_r \left[(\sigma_r - \sigma_m)^{-1} + x_m/(3\sigma_m) \right]^{-1} \tag{2.47}$$

In addition, Archie's law (Archie, 1942) relates empirically bulk conductivity σ_{bulk}, conductivity of pore fluid (melt) σ_f and porosity of a rock ϕ by the formula

$$\sigma_{bulk} = \sigma_f \phi^m \tag{2.48}$$

where m is an empirical constant varying with the inter-connectivity of the pores.

The parallel and Hashin-Shtrikman upper bound conduction models will be used to estimate volume of melt fraction in the upper crust in Chapter 3.

CHAPTER

THREE

MAGNETOTELLURIC IMAGING OF UPPER CRUSTAL PARTIAL MELT AT TENDAHO GRABEN IN AFAR, ETHIOPIA

DIDANA Y. L.[1], THIEL S.[1] AND HEINSON G.[1]

[1]Electrical Earth Imaging Group, Department of Earth Sciences,
School of Physical Sciences, University of Adelaide, Adelaide SA 5005, Australia

Statement of Authorship

Title of Paper	Magnetotelluric imaging of upper crustal partial melt at Tendaho graben in Afar, Ethiopia
Publication Status	☑ Published ☐ Accepted for Publication ☐ Submitted for Publication ☐ Unpublished and Unsubmitted work written in manuscript style
Publication Details	Didana, Y. L., S. Thiel, and G. Heinson (2014), Magnetotelluric imaging of upper crustal partial melt at Tendaho graben in Afar, Ethiopia, Geophysical Research Letters, 41, 3089–3095, doi:10.1002/2014GL060000.

Author Contributions

By signing the Statement of Authorship, each author certifies that their stated contribution to the publication is accurate and that permission is granted for the publication to be included in the thesis.

Name of Principal Author (Candidate)	Yohannes Lemma Didana		
Contribution to the Paper	Planned survey, collected data, processed data, analysed , interpreted and wrote results		
Certification:	This paper reports on original research I conducted during the period of my Higher Degree by Research candidature and is not subject to any obligations or contractual agreements with a third party that would constrain its inclusion in this thesis. I am the primary author of this paper.		
Signature		Date	7/10/15

Name of Co-Author	Stephan Thiel		
Contribution to the Paper	provided valuable supervision of work, aided in data interpretation and manuscript assessment		
Signature		Date	12/10/15

Name of Co-Author	Graham Heinson		
Contribution to the Paper	provided valuable supervision of work, aided in data interpretation and manuscript assessment		
Signature		Date	12/10/15

Abstract

We report on a recent magnetotelluric (MT) survey across the Manda Hararo magmatic segment (MHMS) within the Tendaho graben in the Afar Depression in north eastern Ethiopia. Twenty-two broadband MT sites with ~1 km station spacing were deployed along a profile with the recorded data covering a period range from 0.003 s to 1000 s. A two dimensional (2D) resistivity model reveals an upper crustal fracture zone (fault) and partial melt with resistivity of 1-10 Ω m at a depth of > 1 km. The partial melt has a maximum horizontal width of 15 km and extends to a depth of 15 km within the Afar Stratoid Series basalts. We estimate a melt fraction of about 13% based on geochemical and borehole data, and bulk resistivity from the 2D MT inversion model. The interpreted upper crustal partial melt may have been formed by either a magma intrusion from mantle sources or a large volume of continental crust that has been fluxed by a small amount of mantle melt and heat. Within the MHMS and Tendaho graben, a magma intrusion is a plausible explanation for the upper crustal conductor. The inferred presence of a conductive fracture zone or fault with hydrothermal fluid and shallow heat sourcing magma reservoir also make the Tendaho graben a promising prospect for the development of conventional hydrothermal geothermal energy.

3.1   Introduction

Thinning of the lithosphere associated with continental rifting can potentially lead to decompression melting of the upper mantle (Berckhemer and Baier, 1975; McKenzie, 1978; Hayward and Ebinger, 1996). The Afar Depression in Ethiopia is an ideal location to study the role of magma intrusion in continental extension and rifting. The crust beneath the Afar Depression is ~18-24 km thick and very similar to the crust beneath Iceland (Wright et al., 2006). Previous seismic and magnetotelluric studies in the Ethiopian Main Rift (MER) and the recently active Dabbahu magmatic segment (DMS) in the Afar Depression have revealed partial melts in the lower crust and upper mantle (Mackenzie et al., 2005; Whaler and Hautot, 2006; Desissa et al., 2013; Stork et al., 2013).

The Afar Depression is a rift-rift-rift type triple junction where the MER, the Red Sea Rift and the Gulf of Aden meet in northeast Ethiopia. The Dabbahu and Manda Hararo magmatic segments are located on the southern Red Sea Rift propagator in the Afar Depression (Figure 3.1). In 2005 a mega dike intrusion (length 60 km, volume 2.5 km^3) in the DMS resulted in 8 m of crustal extension (Wright et al., 2006; Rowland et al., 2007; Ebinger et al., 2008; Keir et al., 2009). Integrated geo-scientific studies conducted post diking revealed a significant quantity of melt in the lower crust and upper mantle (Wright et al., 2006; Ebinger et al., 2008, 2010; Hammond et al., 2011; Guidarelli et al., 2011; Desissa et al., 2013). Seismic receiver function studies have identified high v_p/v_s values (above 1.9) at about 6-12 km depth beneath the Afar Depression indicating the presence of partial melt or fluid in the crust (Hammond et al., 2011; Guidarelli et al., 2011). However, a lack of seismic stations directly above the magmatic segments has resulted in reduced resolution across individual rift axes (Hammond et al., 2011). In addition, these studies did not cover the adjoining Tendaho geothermal field located on the Manda Hararo magmatic segment (MHMS) within Tendaho Graben, southeast of DMS (Figure 3.1). The MHMS has not undergone significant tectonic or volcanic activity in the recent past, but significant magmatic eruptions occurred between ~1.8 to ~0.6 Ma (Acocella et al., 2008). The MHMS is an area of increased interest for high temperature

geothermal exploration and development as confirmed by shallow and deep exploratory drilling, with a thick sedimentary basin providing a seal cap (Aquater, 1996a; Battistelli et al., 2002).
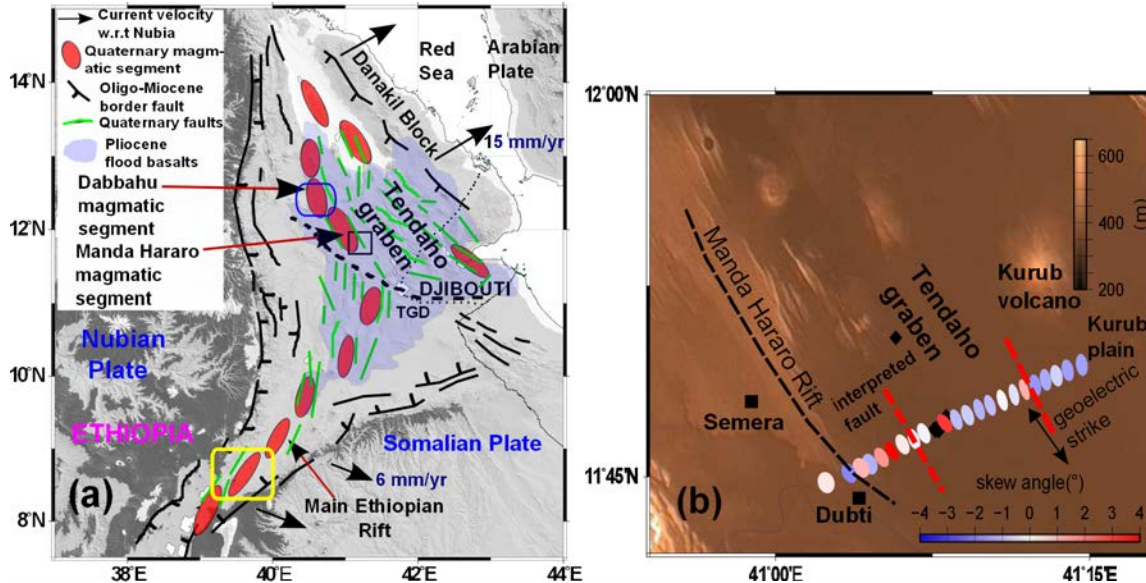
Figure 3.1: Tectonic setting and magnetotelluric (MT) sites of the survey area (redrawn from Hayward and Ebinger (1996)). (a) Map of magmatic segments in the Afar triple junction and the Main Ethiopian Rift, Ethiopia. TGD=Tendaho-Gobaad discontinuity, Rounded corner blue rectangle = MT survey at DMS (Desissa et al., 2013), Yellow rectangle = MT survey at MER (Whaler and Hautot, 2006). The black square survey area is expanded in b. (b) MT station locations crossing the Tendaho geothermal field located within the Tendaho graben. Ellipses indicate MT phase tensor plots at 200 s , Red broken lines=interpreted faults from magnetics, black diamond indicate Geothermal wells.

Here we present results from magnetotelluric (MT) surveys conducted in the Tendaho graben along a SW-NE trending profile perpendicular to the graben's geological strike direction (Figure 3.1). A two dimensional (2D) inversion of the MT data reveals significant partial melt and fluid pathways in the upper crust. We also combine geochemical, borehole and MT information to estimate the melt fraction of the upper crustal magma reservoir.

3.2   Method

Magnetotellurics is a passive electromagnetic method sensitive to electrical conductivity contrasts in the Earth's crust, caused particularly by

conductive materials such as metallic minerals, graphite, molten rock (partial melts) and aqueous fluids (Spichak and Manzella, 2009; Chave and Jones, 2012). The MT technique involves measuring fluctuations in the natural electric ($\mathbf{E}$) and magnetic ($\mathbf{B}$) fields in orthogonal directions on the Earth's surface, as a means of determining its internal conductivity structure (Chave and Jones, 2012). The impedance tensor ($\mathbf{Z}$) describes the relation between the electric ($\mathbf{E}$) and magnetic ($\mathbf{B}$) fields which is given by $\mathbf{E} = \mathbf{Z}\,\mathbf{B}$ or in matrix form:

$$\begin{pmatrix} E_x \\ E_y \end{pmatrix} = \begin{pmatrix} Z_{xx} & Z_{xy} \\ Z_{yx} & Z_{yy} \end{pmatrix} \begin{pmatrix} B_x \\ B_y \end{pmatrix} \tag{3.1}$$

A total of 22 MT stations were acquired by the Geological Survey of Ethiopia along the profile with station spacing of ~1 km (Figure 3.1). Two 5-channel MT data acquisition systems (MTU-5A, Phoenix Geophysics Ltd) were used to record the MT data. A sounding was produced at each site from a 24 hour recording covering a period range from 0.003 s to 1000 s with a remote reference positioned 20 km from the survey area. The MT data were processed using the robust processing program SSMT2000 from Phoenix Geophysics Ltd. Dimensionality analysis was performed using the phase tensor approach (Caldwell et al., 2004). Skew angles are less than three degrees for most sites, which is consistent with a 2D regional conductivity structure beneath the survey area (Figure 3.1). This is further verified using the ellipticity criterion of MT data formulated by Becken and Burkhardt (2004). Subsequently, the data are rotated to a geoelectric strike angle of $x' = -25°$ (supporting information Figure A.2 in Appendix A). The $x'y'$ component of the MT data is assigned as the Transverse Electric (TE) mode and the $y'x'$ component is assigned as the Transverse Magnetic (TM) mode.

We invert the data using the 2D Occam inversion code (de Groot-Hedlin and Constable, 1990) with a grid of 279 horizontal nodes and 100 vertical layers with layer thickness increasing logarithmically with depth. The model space used extends 600 km in the horizontal and 300 km in the vertical directions to avoid boundary effects. A total of 74 periods (0.003 s–1000 s) are used for the inversion. Many 2D joint inversions of TE and TM modes with different starting models were carried out. A

starting model of homogeneous half space of 100 $\Omega\,\text{m}$ was used for the model presented here. Error floors of 10% for resistivity and 3% (equivalent to 1°) for phase were used for the joint inversion of TE and TM modes. The preferred model of the joint inversion achieved a minimum misfit of RMS ~1.9. Pseudo-section plots of the observed data and model response obtained for this model are shown in Figure 3.2 and site-by-site plots of the model fit are given in the supporting information Figures A.3, A.4 and A.5 in Appendix A. At periods >10 s the pseudo-section indicates that the TE and TM mode resistivity and phase are different, which is consistent with the multi-dimensional nature of the MT data identified by the phase tensors. There is asymmetry in the long period phase response (100 s) in the TE and TM modes; this may be explained by the TM mode sensing deeper than the TE mode for similar periods. The TM mode inversion model, which shows similar resistivity structure to the joint inversion, is presented in the supporting information Figure A.6 in Appendix A.
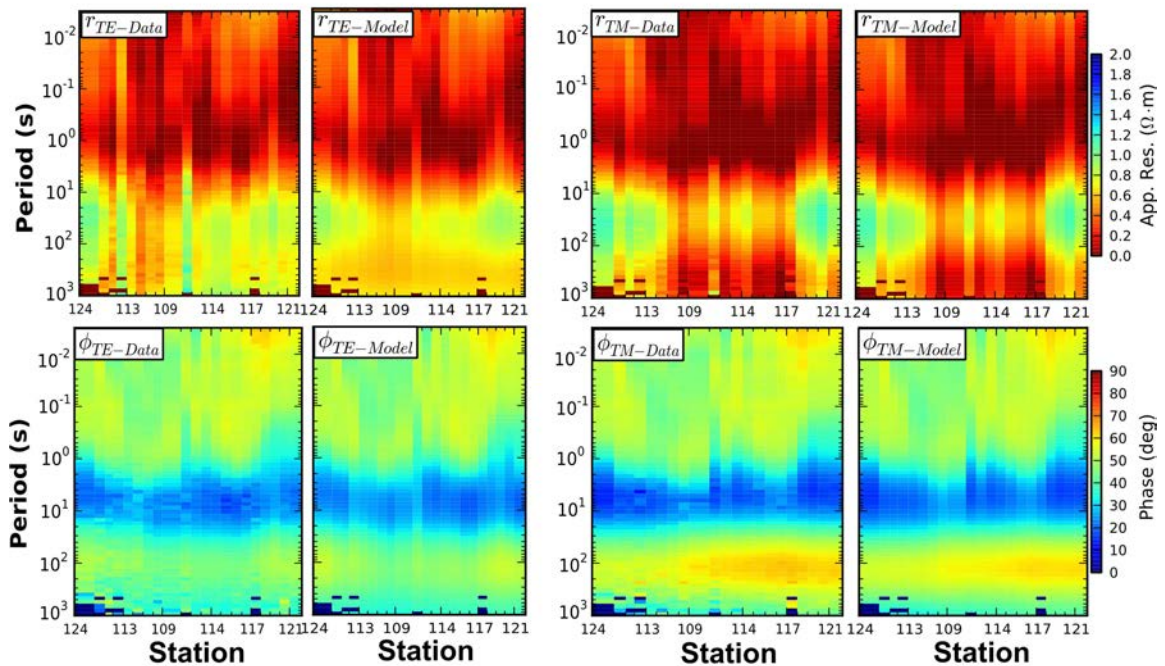
Figure 3.2: Pseudo-section plots of observed and calculated response of apparent resistivity and phase along the profile from southwest to northeast for TE (left) and TM (right) modes. At periods >10 s the pseudo-section indicates that the TE and TM mode resistivity and phase are different, which is consistent with the multi-dimensional nature of the MT data identified by the phase tensors. Top panel, apparent resistivity; bottom panel, phase.

3.3   Results and Discussion

The 2D inversion model reveals five main resistivity zones (Figure 3.3). The surface conductive zone (C1) is $1\,\mathrm{km}$ thick, with resistivity $\leq 10\,\Omega\,\mathrm{m}$, and spans the entire cross-section. This conductive zone is mostly associated with sediments and to some extent saline geothermal fluids and smectite clay alteration (Aquater, 1996a). The high resistivity zone (R1) of $> 10\,\Omega\,\mathrm{m}$ is inferred to be the background resistivity of the Afar Stratoid Series basalts or chlorite-epidote alteration mineralogy (Aquater, 1996a). Values of R1 $> 1000\,\Omega\,\mathrm{m}$ are more realistic and can be seen further away from the inferred fault.
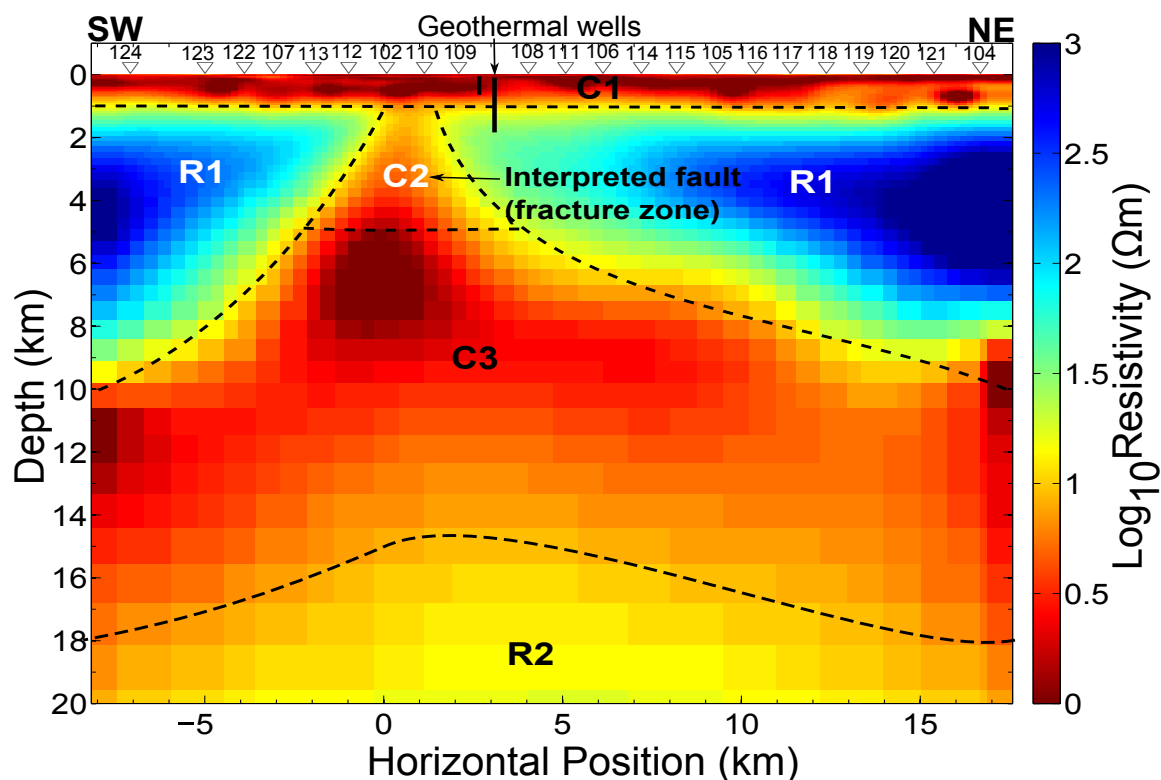
Figure 3.3: Preferred 2D resistivity model obtained by joint inversion of TE and TM mode data for the MT profile with a RMS misfit of 1.9. C1, C2 & C3 are low resistivity zones. R1 and R2 are high resistivity zones. Inverted triangles on top of the model are MT station locations. Black vertical lines are shallow and deep geothermal wells.

The conductive "up-doming" zone (C2) with resistivity $\leq 10\,\Omega\,\mathrm{m}$ at a depth of 1-5 km is interpreted as a fault (fracture zone) filled with a

geothermal fluid plume. Sensitivity tests using forward modeling and inversion indicate that C2 has connection to the surface conductor C1. This structure also coincides with the fault located to the southwest which is inferred from magnetics survey in the area (Figures 3.1b and 3.3 and in the supporting information Figure A.10 in Appendix A). The fault interpreted to the northeast from magnetics is not observed in the MT cross section within the Afar Stratoid basalts (Figure 3.1b and in the supporting information Figure A.10 in Appendix A). This inferred fault has either no fluid within it or it is located in the top sedimentary formation.

The drilling of shallow and deep geothermal wells confirmed two geothermal reservoirs at the Tendaho high temperature geothermal field (Amdeberhan, 1998; Battistelli et al., 2002). These include a shallow reservoir in the sedimentary sequence (temperature 240-250 °C, depth 300 m-500 m) and a deep reservoir in the Afar Stratoid Series basalts (260-270 °C). The deep reservoir is characterized by low permeability (Amdeberhan, 1998; Battistelli et al., 2002). Hence, targeting a fracture zone/fault (C2) in the Afar Stratoid Series basalts by directional drilling will increase the permeability and productivity of the deep reservoir. The discontinuous alignment of the surface geothermal manifestations (fumaroles, boiling mud craters, steaming grounds and hydrothermal deposits) in a NW-SE direction (N125°E) shows that the Tendaho geothermal field is structurally controlled (Aquater, 1996a; Battistelli et al., 2002). Using the simplest form of Archie's law (Archie, 1942) $\rho_b = \rho_f \Phi^{-m}$ (neglecting water saturation and tortuosity factor) with the bulk resistivity $\rho_b = 10\,\Omega\,\mathrm{m}$ of C1 from the resistivity model and the resistivity of fluid $\rho_f = 3.03\,\Omega\,\mathrm{m}$ measured in the geothermal wells (Aquater, 1996a) (cementation factor m=2), the porosity of the shallow sedimentary reservoir is 55%.

The low resistivity body (C3) at a depth of $> 5\,\mathrm{km}$, which has a horizontal width of 15 km, and is interpreted as partial melt within the Afar Stratoid Series basalts. Within the MHMS and Tendaho graben, the presence of a partial melt is a plausible explanation for the enhanced conductivity. The conductive body C3 can also be considered as the heat source of the Tendaho high temperature geothermal system. A similar upper crustal

magma reservoir is also observed at Krafla and Hengill high temperature geothermal fields in Iceland (Mid-Oceanic Ridge) (Árnason et al., 2010; Gasperikova et al., 2011). The structure (R2) at the bottom of the cross section has high resistivity compared to C3. However, only the TM mode of the MT measurements is sensitive to the increase in resistivity and long period MT measurement is needed to fully resolve the actual resistivity of R2.

In order to explain the high conductivity of the observed structure C3 at depth, it is necessary to estimate the volume fraction of the melt which causes the anomalous response. For the partial melt to enhance conductivity, it must form an interconnected network within the resistive rock matrix (Sato and Ida, 1984; Roberts and Tyburczy, 1999). The conductivity of a partial melt depends on its composition, temperature, water content and to a small extent on pressure (Tyburczy and Waff, 1983; Li et al., 2003). Given constraints on the above, the web-based application SIGMELTS can be used to determine the conductivity of the melt (Pommier and Le-Trong, 2011).

In order to estimate the composition of the melt, geochemical data from ten rock samples from the survey area from Barrat et al. (2003) were used. Estimates of SiO_2 and Na_2O contents are $47.83 \pm 1.02\%$ and $2.5 \pm 0.3\%$, respectively. The water content of the rock samples was not reported in Barrat et al. (2003) and was estimated to be 0.4 wt. % based on melt inclusions in rock samples from the DMS of Field et al. (2013). The temperature of the melt is estimated from a mean surface temperature of 35 ℃ and the bottom-hole temperature of five geothermal wells in the study area (Amdeberhan, 1998; Battistelli et al., 2002). Using a temperature gradient of $132 \, ℃ \, km^{-1}$, the temperature of the melt was estimated to be 1188 ℃ at 9 km depth where C3 spreads out (Figure 3.3). The pressure was estimated to be 225 MPa based on pressure data determined at the DMS (Desissa et al., 2013). We tested different combinations of composition, temperature, water content, and pressure to infer their influence on estimated melt conductivity using SIGMELTS (supporting information Table A.1 in Appendix A). The results of our tests suggest that the conductivity of the melt is highly sensitive to variation of water content, composition and temperature, but not pressure.

To estimate the minimum melt fraction required to explain the crustal conductor C3 (predominantly with bulk resistivity of 3-10 Ω m), we assume a parallel conduction model (Roberts and Tyburczy, 1999; ten Grotenhuis et al., 2005) given by

$$\sigma_p = \sigma_m x_m + \sigma_r x_r \tag{3.2}$$

where σ_p is the parallel conductivity, σ_m and σ_r are the conductivities of the melt and host rock, respectively, and x_m and x_r are the respective volume fractions. The parallel model of a stack of layers gives a lower estimate of melt fraction than the Hashin-Shtrikman upper bound model. The Hashin-Shtrikman upper bound model (Hashin and Shtrikman, 1962) assumes interconnected melts with isolated matrix grains which produce higher estimates than the parallel conduction model.

A melt conductivity of σ_m=2.5 S m^{-1} (corresponding to 0.4 wt.% water content) for the basaltic melt and a fixed host rock conductivity value of σ_r=5×10^{-4} S m^{-1} (equivalent to 2000 Ω m) were used to estimate melt fraction. A plot of the corresponding electrical resistivity versus melt fraction by volume is shown in Figure 3.4. The parallel model gives volume melt fractions of 4-13 Vol.% for the crustal conductive body C3 with bulk resistivity suggested by the MT model (Figure 3.4). Therefore, a melt fraction between 4 and 13 Vol.% for σ_m=2.5 S m^{-1} can be taken as a minimum estimate of the partial melt to explain the enhanced conductivity of C3.
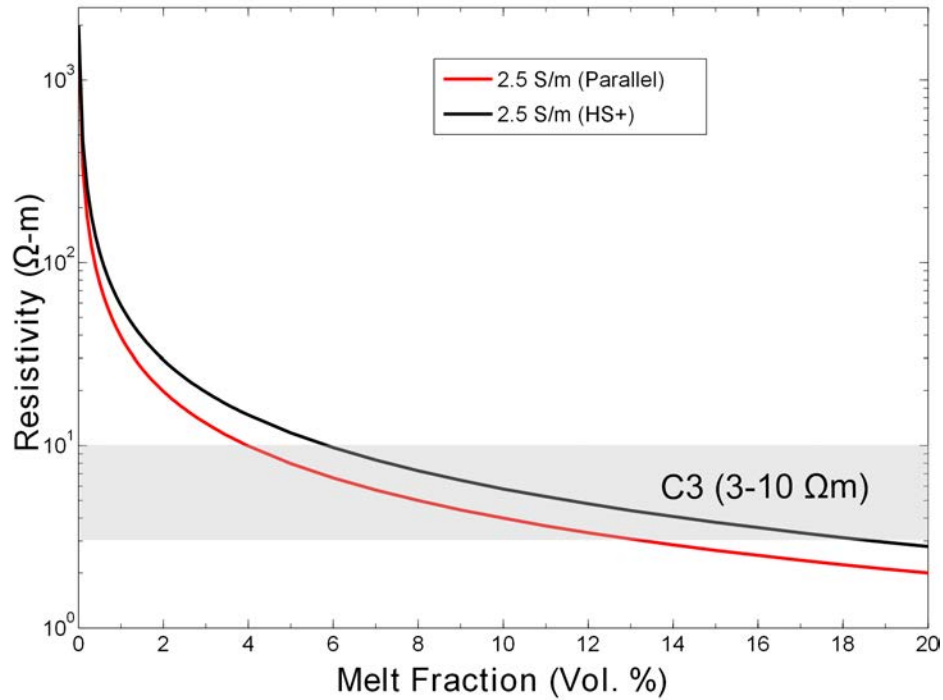
Figure 3.4: Calculated electrical resistivity of a partially molten rock as a function of melt fraction for parallel model (red curve) (Roberts and Tyburczy, 1999) and the Hashin-Shtrikman upper bound ($HS+$) with conductivity of $2.5\,S\,m^{-1}$ (black curve) (Hashin and Shtrikman, 1962); the conductivity of the solid phase is set to $0.0005\,S\,m^{-1}$. A melt fraction between 13% and 4% is a minimum estimate that may reasonably describe the enhanced conductive body C3 in the upper crust at Tendaho graben, Afar, with bulk resistivity values (shaded region) $3\,\Omega\,m$ & $10\,\Omega\,m$, respectively.

The upper crustal partial melt can be explained by either a magma intrusion from mantle sources or a large volume of continental crust which has been fluxed by a small amount of mantle melt and heat. Geophysical studies conducted in the MER and the DMS have indicated that magma intrusions and diking play a more significant role than faulting in strain accommodation in the late stages of continental rifting (Casey et al., 2006; Wright et al., 2006; Ebinger et al., 2008, 2010; Hammond et al., 2011; Hamling et al., 2014). Similar results were obtained in Natron rift, Tanzania (East African continental rift) (Calais et al., 2008) and the Lucky Strike segment of the low spreading Mid-Atlantic Ridges (Singh et al., 2006).

3.4   Conclusions

The surface conductive structure in the model is associated with sediments, geothermal fluids and smectite clay alteration (Aquater, 1996a). The high background resistivity at a depth of about 2 km is interpreted as Afar Stratoid Series basalts or chlorite-epidote alteration mineralogy (Aquater, 1996a). Targeting the inferred fracture zone (fault) in the Afar Statoid basalts by directional drilling will likely increase the permeability and temperature of the deep reservoir. The low resistivity structure at a depth of >5 km is related to partial melt in the Afar Stratoid Series basalts. A melt fraction of about 13% by volume is a minimum estimate for this structure, based on geochemical and borehole information and a bulk resistivity from the 2D resistivity model. There is inherent uncertainty in this estimation, caused by uncertainties in composition, temperature, the true melt geometry and water content. However, this estimated melt fraction is comparable to the melt fraction determined for the lower crust and upper mantle conductor at the DMS (Desissa et al., 2013). Regional seismic tomography studies also indicate the presence of significant melt in the crust beneath the Afar Depression as a whole (Hammond et al., 2011; Guidarelli et al., 2011). Diking and magmatic intrusions fed by upper mantle sources play a significant role in the creation of new oceanic crust in the late stages of continental break up, as observed at the MER, the DMS and other continental rifts and slow spreading Mid-Oceanic Ridges (Casey et al., 2006; Singh et al., 2006; Wright et al., 2006; Calais et al., 2008; Ebinger et al., 2010; Hammond et al., 2011; Desissa et al., 2013; Hamling et al., 2014). The inferred presence of a fault with hydrothermal fluid plumes and shallow magma reservoirs, which act as heat sources, make the Tendaho graben a promising prospect for the development of conventional hydrothermal geothermal energy. Integrating long period MT data with seismic data will help to resolve the deep mantle source for the shallow magma reservoirs.

Acknowledgments

THREE DIMENSIONAL CONDUCTIVITY MODEL OF THE TENDAHO HIGH ENTHALPY GEOTHERMAL FIELD, NE ETHIOPIA

DIDANA Y. L.[1], THIEL S.[1] AND HEINSON G.[1]

[1]Electrical Earth Imaging Group, Department of Earth Sciences,
School of Physical Sciences, University of Adelaide, Adelaide SA 5005, Australia

Statement of Authorship

Title of Paper	Three dimensional conductivity model of the Tendaho High Enthalpy Geothermal Field, NE Ethiopia.
Publication Status	☑ Published ☐ Accepted for Publication ☐ Submitted for Publication ☐ Unpublished and Unsubmitted work written in manuscript style
Publication Details	Didana, Y. L., Thiel, S., & Heinson, G. (2015). Three dimensional conductivity model of the Tendaho High Enthalpy Geothermal Field, NE Ethiopia. *Journal of Volcanology and Geothermal Research, 290*, 53-62, doi:10.1016/j.jvolgeores.2014.11.013

Author Contributions

By signing the Statement of Authorship, each author certifies that their stated contribution to the publication is accurate and that permission is granted for the publication to be included in the thesis.

Name of Principal Author (Candidate)	Yohannes Lemma Didana		
Contribution to the Paper	Planned survey, collected data, processed data, analysed , interpreted and wrote results		
Certification:	This paper reports on original research I conducted during the period of my Higher Degree by Research candidature and is not subject to any obligations or contractual agreements with a third party that would constrain its inclusion in this thesis. I am the primary author of this paper.		
Signature		Date	7/10/15

Name of Co-Author	Stephan Thiel		
Contribution to the Paper	provided valuable supervision of work, aided in data interpretation and manuscript assessment		
Signature		Date	12/10/15

Name of Co-Author	Graham Heinson		
Contribution to the Paper	provided valuable supervision of work, aided in data interpretation and manuscript assessment		
Signature		Date	12/10/15

Abstract

Tendaho is one of the high enthalpy geothermal fields at advanced stage of exploration which is located in the Afar Depression in north eastern Ethiopia. Six deep and shallow geothermal wells were drilled in the field between 1993 and 1998. Here we present the first 3D conductivity model of the Tendaho high enthalpy geothermal field obtained from 3D inversion of magnetotelluric (MT) data. MT data from 116 sites at 24 selected periods in the period range from 0.003 s to 1000 s were used for the 3D inversion. The 3D conductivity model reveals three main resistivity structures to a depth of 20 km. The surface conductive structure ($\leq 10\,\Omega\,\mathrm{m}$ and > 1 km thick) is interpreted as sediments, geothermal fluids or hydrothermally altered clay cap. The underlying high resistivity structure in the Afar Stratiod basalts is associated with the deep geothermal reservoir. At a depth > 5 km, a high conductivity is observed across the whole of the Tendaho geothermal field. This structure is inferred to be the heat source (partial melt) of the geothermal system. The most striking feature in the 3D model is a fracture zone (upflow zone) in the Afar Stratoid basalts at the Dubti area, which acts as a pathway for geothermal fluids. Targeting the inferred fracture zone by directional drilling will likely increase the permeability and temperature of the deep reservoir in the basalts. Hence, the inferred presence of a fracture zone and shallow magma reservoir suggest there is huge potential (with temperature exceeding 270℃ at 2 km depth) at Tendaho for conventional hydrothermal geothermal energy development.

4.1   Introduction

The Afar Depression is an area of active extensional tectonics and volcanism where the Main Ethiopian Rift (MER), the Red Sea rift and the Gulf of Aden meet in north eastern Ethiopia (McKenzle and Morgan, 1969; Abbate et al., 1995). Tendaho is a high enthalpy geothermal field in the Afar Depression. The Tendaho geothermal field consists of three geothermal localities: Dubti, Ayerobera and Allalobeda (Aquater, 1996a). Geothermal exploration in the Afar depression and the MER was started in the 1970s (UNDP, 1973).

Several integrated geo-scientific studies have been conducted in the Tendaho geothermal field to investigate the geothermal potential of the area (UNDP, 1973; Aquater, 1979, 1980, 1996a,b). The methods used include surface geological mapping, geochemical and geophysical investigation, hydrogeological exploration and drilling temperature gradient wells (Aquater, 1996a; Battistelli et al., 2002). Exploratory drilling of six shallow (500 m) and deep wells (2100 m) confirmed the existence of a geothermal resource with bottom-hole temperature in excess of 270 °C at depth of about 2 km (Aquater, 1996a; Battistelli et al., 2002). However, the geoelectric sounding technique used lacked depth of penetration beyond one kilometer for delineating the deep geothermal reservoir in the Afar Stratoid basalts (Aquater, 1980).

Magnetotellurics (MT) is a method which can reliably probe to the depths needed to target geothermal reservoirs at about 2-3 km depth (Heise et al., 2007; Spichak and Manzella, 2009; Chave and Jones, 2012; Peacock et al., 2013; Muñoz, 2014). Geothermal systems are ideal targets for electromagnetic geophysical methods as saline geothermal fluids, partial melts and clay alteration minerals create higher conductivity that contrasts with the low conductivity of the host rock (Spichak and Manzella, 2009; Bertrand et al., 2012; Chave and Jones, 2012; Muñoz, 2014). Recent advances in 3D MT modelling and inversion codes (Mackie et al., 1994; Farquharson et al., 2002; Siripunvaraporn et al., 2005; Egbert and Kelbert, 2012) and the availability of high performance parallel computing makes it possible to undertake 3D inversions of MT data. Here we present 3D inversion results from 116 MT sites along seven

profiles acquired at the Tendaho high enthalpy geothermal field (Figure 4.1).
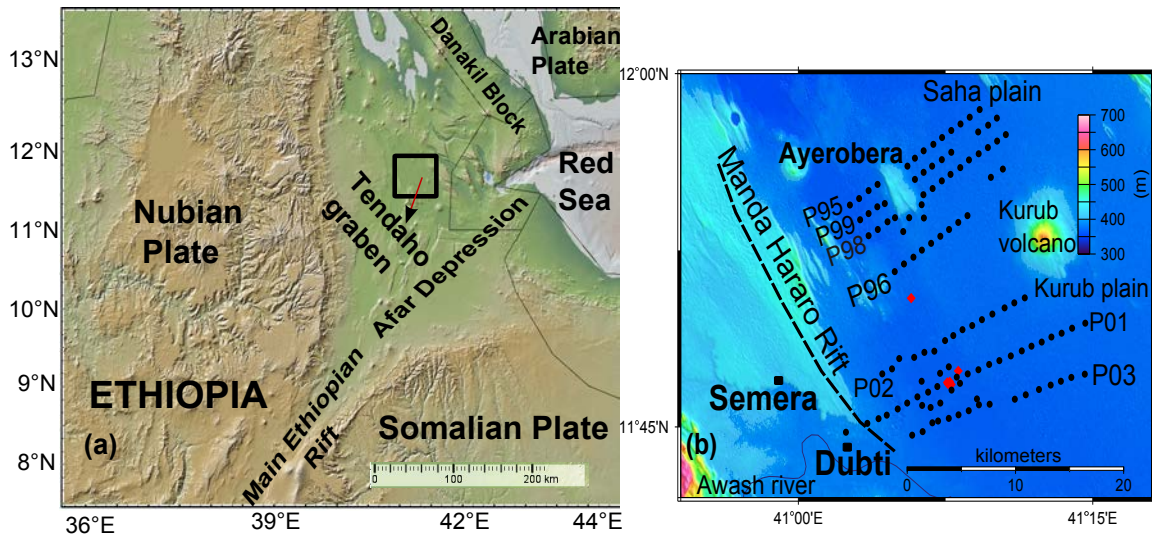
Figure 4.1:   Digital Elevation map of Ethiopia and magnetotelluric (MT) sites of the survey area (a) Afar Depression and the Main Ethiopian Rift (Image from http://www.geomapapp.org). The black square survey area is expanded in Figure 4.1b. (b) Seven MT profiles crossing the Tendaho geothermal field located within the Tendaho graben, red diamonds indicate geothermal wells.

4.2   Materials and Methods

4.2.1   Geologic and tectonic setting

Tendaho graben is a NW-SE trending structural trough situated in the southern portion of the Erta-Manda Hararo rift system in the Afar depression (Figure 4.1; UNDP, 1973; Abbate et al., 1995; Aquater, 1996a). It is 50 km wide and more than 100 km long from NW-SE (UNDP, 1973; Abbate et al., 1995). The margins of the Tendaho graben are comprised of the Afar Stratoid Series basalts and the rift centre is filled with lacustrine and alluvial deposits and post stratoid basalt flows (Figure 4.2a; UNDP, 1973; Abbate et al., 1995; Aquater, 1996a). In the Tendaho region, NW and NNE trending normal faults predominate (Figure 4.2a; Abbate et al., 1995; Aquater, 1996a); however, strike-slip faults are also observed in the area (Abbate et al., 1995; Aquater, 1996a).
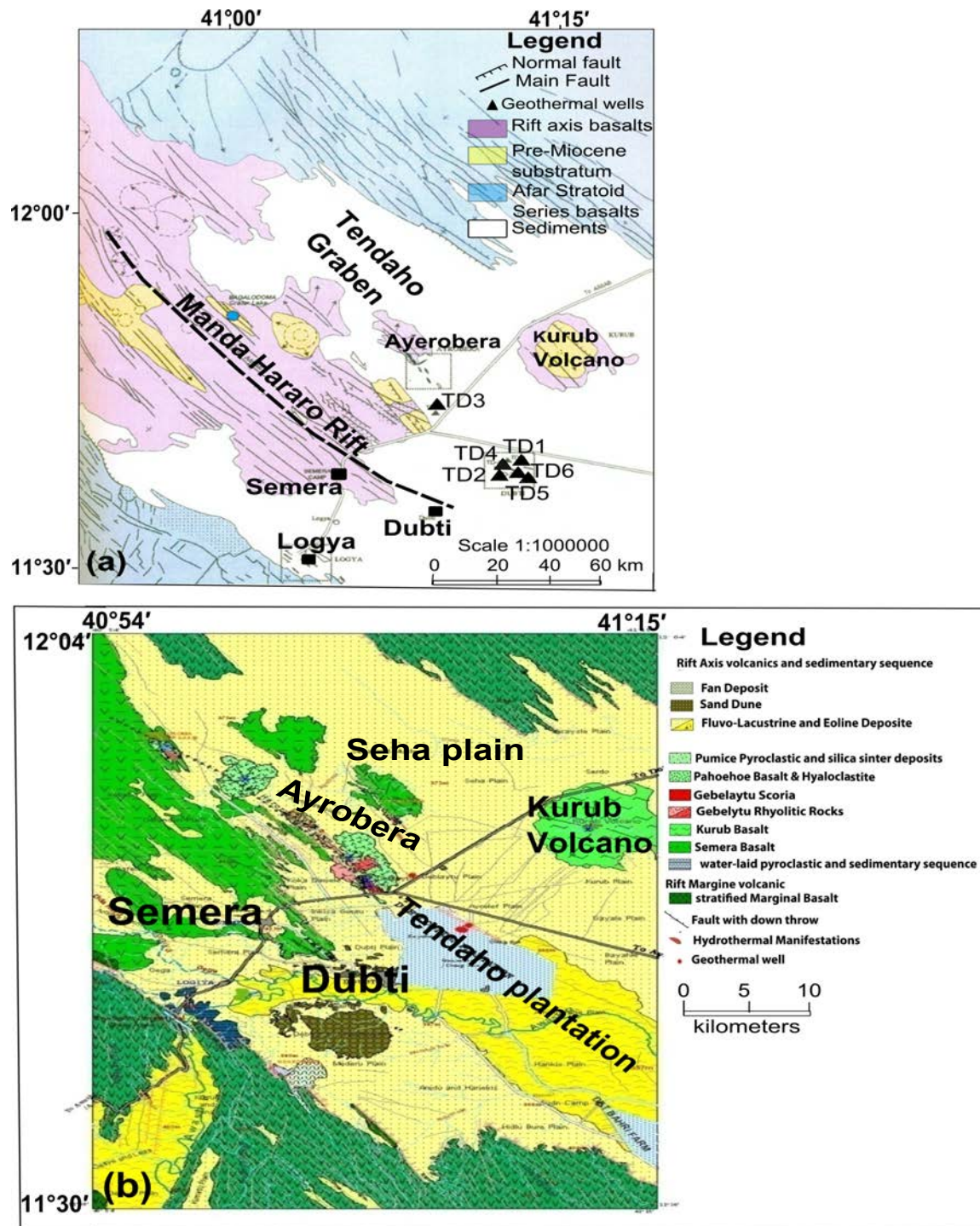
Figure 4.2: Tectonic and geologic setting of Tendaho geothermal area (a) Structural map of Tendaho (Abbate et al., 1995; Aquater, 1996a). (b) Local geology of NW Tendaho (Megersa and Getaneh, 2006).

The NNE trending faults most likely have played only a minor role in the evolution of the Tendaho graben, as the dominant structural elements are

NW trending (UNDP, 1973). However, the intersection of these two fault trends appears to coincide with the locations of current hydrothermal activity (UNDP, 1973). Evidence for active NW striking faults includes aligned steaming grounds, fumaroles and hydrothermal deposits in the sediments within the Dubti area (Figure 4.2b; Aquater, 1996a).

The detailed surface geology of the Tendaho high temperature geothermal field and its surrounding was mapped at a scale of 1:50,000 with the following units identified by Megersa and Getaneh (2006): (i) a rift margin complex which consists of stratified rift margin basalts; and (ii) a rift axis complex comprised of volcanic and sedimentary sequences (Figure 4.2b).

The rift axis volcanic complex includes the Ayrobera-Semera water-laid pyroclastic and sedimentary sequence, Semera basalt, Kurub basalt, Gebelaytu rhyolitic rocks, Geblaytu scoria and Geblaytu-Asboda fresh pahoehoe basalt and hyaloclastite. Fluvial, lacustrine and eoline sedimentation have been simultaneously carried with the axial volcanic activity, mainly in the graben area (Megersa and Getaneh, 2006). The measured surface temperatures on geothermal manifestations mainly fall in the range 65-100.3°C (Megersa and Getaneh, 2006).

Six wells were drilled in the Tendaho geothermal field from 1993 to 1998 (Aquater, 1996a; Battistelli et al., 2002). Wells TD1, TD2 and TD3 are deep wells with depths of 1550 m, 1881 m and 1989 m, respectively (Figure 4.2a). Wells TD4, TD5, and TD6 are shallow wells with depths of 466 m, 516 m and 505 m, respectively (Figure 4.2a). Wells TD2, TD4, TD5 and TD6 are productive. The recorded bottomhole temperature in the shallow and deep wells is in the range of 235-270°C (Aquater, 1996a; Amdeberhan, 1998; Battistelli et al., 2002). A production test and feasibility study conducted on the shallow productive wells indicated electric power potential of about 5 MW$_e$ and the potential of the deep reservoir in the basalts is estimated about 20-30 MW$_e$ (Battistelli et al., 2002; Teklemariam and Beyene, 2005). According to the stratigraphy under the Tendaho graben floor revealed by geophysics and drilling, there are two major rock units (Aquater, 1996a). These are an upper unit of a thick sedimentary sequence consisting of fine to medium-grained

sandstone, siltstone and clay, intercalated by basaltic lava sheets ($>1\,$km thick); and a lower unit of basaltic lava flows of the Afar Stratoid Series.

4.2.2   Geophysical Setting

Geophysical studies have been carried out at the Tendaho geothermal field, with the aim to investigate the deep structures and to delineate the geothermal reservoir. The methods used include vertical electrical sounding (VES), magnetics and gravity survey (e.g. UNDP, 1973; Aquater, 1980) and transient electromagnetics and magnetotellurics (MT) (Lemma, 2007; Kalberkamp, 2010; Didana et al., 2014).

A VES survey conducted at the Tendaho geothermal field reached a maximum depth of penetration of about $1\,$km. The data lacked resolution required to differentiate layers within the sedimentary and basaltic sequences (Aquater, 1980). In addition, Aquater (1980) acquired 2086 gravity stations in the Tendaho field. The NW-SE trending gravity low observed near Tendaho plantation (refer to Figure 4.2b for location) is related to a depression of the high-density substratum. A strong positive Bouguer gravity anomaly centered over the Ayrobera area may be due to a dense intrusive body in the fluvial-lacustrine sediment system (Aquater, 1980).

A total field magnetic survey showed a general NW-SE magnetic anomaly in the Tendaho geothermal field (Aquater, 1980). The anomaly extends from NW to SE following the Tendaho graben axis with minor anomaly interruptions attributed to near surface inhomogeneities.

Nine temperature gradient wells were drilled to map the subsurface temperature distribution in the Tendaho graben and Logiya area (Aquater, 1980). However, due to shallow depths of the boreholes (76.6-173.5 m) the reservoir temperature is masked by thick sediment layers and the presence of hot or cold shallow aquifers. A micro-seismic survey in the Tendaho graben indicated that the hypocenters of seismic events are distributed in a NW-SE direction and to a depth between 5 and 10 km (Aquater, 1995). Two-dimensional MT models reveal what is interpreted as an upper crustal fracture zone (fault) and shallow magma

reservoir (partial melt) at depth of 5 km at Tendaho geothermal field (Kalberkamp, 2010; Didana et al., 2014).

4.2.3   Method

Magnetotellurics is a passive electromagnetic method used to investigate the electrical conductivity of the Earth (Chave and Jones, 2012). The MT method is sensitive to electrical conductivity contrasts in the Earth's crust caused particularly by conductive materials, such as metallic minerals, graphite, geothermal fluids, and molten rocks (partial melts)(Chave and Jones, 2012; Muñoz, 2014). The MT technique involves measuring natural ($\mathbf{E}$) and magnetic ($\mathbf{H}$) in orthogonal directions on the Earth's surface. The complex impedance tensor ($\mathbf{Z}$) describes the relationship between the ($\mathbf{E}$) and magnetic ($\mathbf{H}$); mathematically $\mathbf{E} = \mathbf{Z}\,\mathbf{H}$ or in matrix form

$$
\begin{pmatrix} E_x \\ E_y \end{pmatrix} = \begin{pmatrix} Z_{xx} & Z_{xy} \\ Z_{yx} & Z_{yy} \end{pmatrix} \begin{pmatrix} H_x \\ H_y \end{pmatrix} \tag{4.1}
$$

The geomagnetic transfer function (Tipper) τ is a complex vector describing the relationship between the horizontal ($\mathbf{H_x}$ and $\mathbf{H_y}$) and the vertical ($\mathbf{H_z}$) magnetic fields, i.e.

$$
\mathbf{H_z} = \tau_{zx}\mathbf{H_x} + \tau_{zy}\mathbf{H_y} \tag{4.2}
$$

Data was acquired from a total of 116 MT stations with spacing of about 1 km along seven profiles by the Geological Survey of Ethiopia within the Tendaho geothermal field between 2010 and 2012. The directions of the profiles were chosen to be approximately perpendicular to the known geologic strike direction of the Tendaho graben (Figure 4.1). An MTU-5A MT unit (Phoenix Geophysics Ltd) was used to acquire the MT data. At each station 24 hours of recording was made covering a period range from 0.003 s to 1000 s with a remote reference positioned 20 km from the survey area. The vertical component of the magnetic field data were also recorded at most stations. The MT data were processed using the robust processing program SSMT2000 (Phoenix Geophysics Ltd). The MT data acquired at Tendaho graben, which is a sedimentary basin filled with alluvial and lacustrine sediments, is not affected by static

shift. This was also demonstrated by Lemma (2007) using collocated transient electromagnetic (TEM) and MT surveys in the area.

We inverted the MT data from Tendaho using the parallelized 3D inversion code ModEM (Meqbel, 2009; Egbert and Kelbert, 2012; Kelbert et al., 2014). The inversion algorithm is based on standard minimum structure non-linear conjugate gradients. The 3D inversion was run on a high performance computing facility, Dell R810, with 32 processing cores and 512 GB RAM. Different ModEM 3D inversions were tested in order to select the best approach for the inversion process. Many 3D inversions were run to get a plausible conductivity model for Tendaho which included full impedance components (in geographic coordinate and rotated to geo-electric strike direction), off-diagonal impedance components, joint full impedance and vertical transfer functions with different grid discretization, smoothing parameters, and different starting models (homogeneous half space and layered earth). All inversion runs resulted in similar resistivity structures.

The MT data from Tendaho have skew angle of phase tensor less than three degrees (Caldwell et al., 2004) for most sites which is consistent with a 2D regional resistivity structure (Figure 4.3). Tietze and Ritter (2013) demonstrated that if the resistivity structure in a survey area is predominately 2D in nature, rotation of MT data to geo-electric strike direction before 3D inversion helps resolve deep geologic structures. Hence, the 3D inversion result presented here is a 3D model of full impedance tensor obtained by rotating the MT data to the dominant geoelectric strike of −21°. The geoelectric strike direction was obtained using the phase tensor and ellipticity criterion of the MT data (Caldwell et al., 2004; Becken and Burkhardt, 2004). We inverted the full impedance tensor for 24 periods in the period range of 0.003 s to 1000 s. Error floors of 5% of the geometric mean of off-diagonal components were set for the impedance tensor elements. The model space extends 100 km in the E-W and N-S directions and to a depth of 100 km. The model grid is discretised into $60 \times 60 \times 65$ cells in x, y and z directions, respectively. The model grid is rotated to align with the profile direction. The central part of the mesh grid has a cell size of 800 m $\times$ 800 m and a padding which increases by a factor of 1.3 was used at the edges of the grid. The
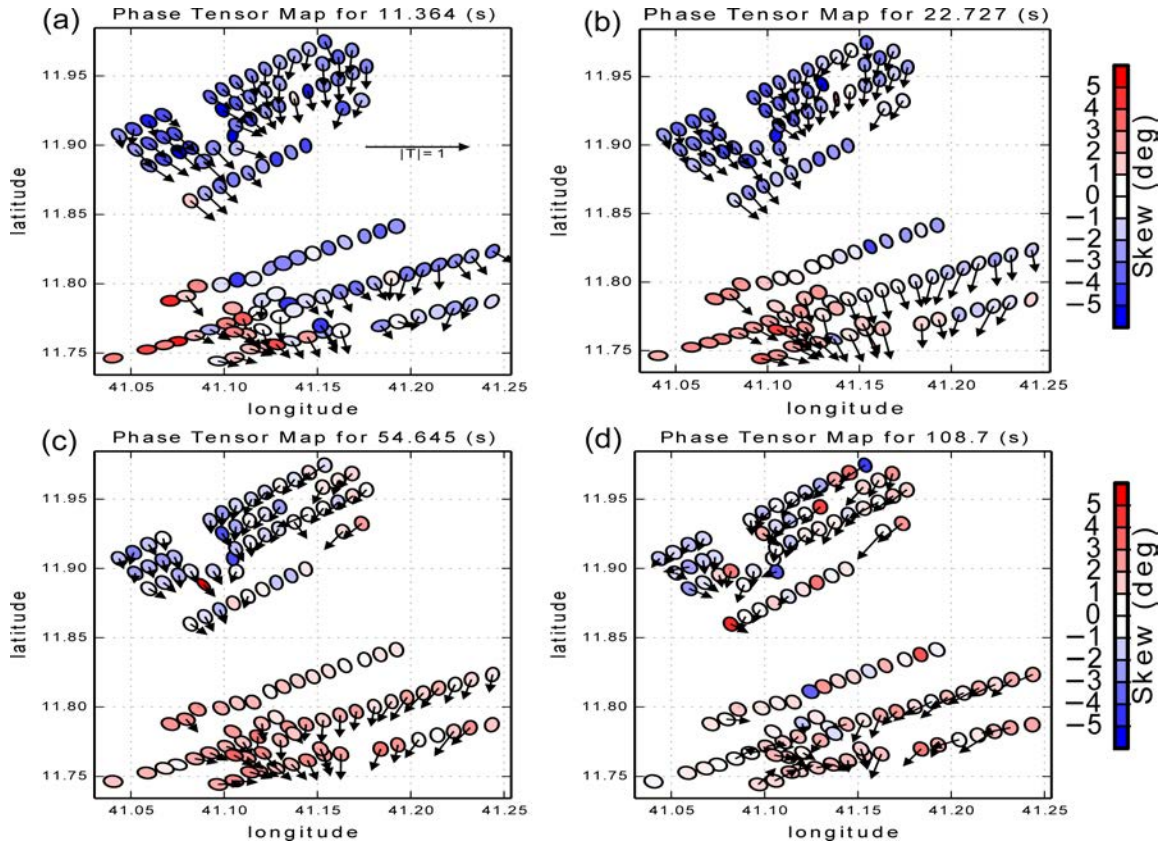
Figure 4.3: Phase tensor ellipse and real induction arrows at four different periods (11.3 s, 22.2 s, 54.6 s and 108.7 s) colored by beta angle. For most sites at the selected periods the skew angle is less than 3 degrees which consistent with 2D regional conductivity structure. The induction arrows point toward a conductor (Parkinson, 1962).

thickness of the first layer is 20 m and increases with depth by a factor of 1.1 for each subsequent layer. A starting model of homogeneous half space of 30 Ω m was used. The final 3D model from 30 Ω m half space was rerun to obtain the preferred 3D model of Tendaho. The preferred 3D conductivity model fits the entire data set to an overall RMS of 1.13 after 80 NLCG total iterations (starting from initial RMS of 20.57 for half space model). The misfit phase tensor map for selected periods as defined in Heise et al. (2008) and Booker (2014) is presented in Figure 4.4 to show the residual phase tensor between the measured and calculated phase tensors. The small size of the misfit ellipses in Figure 4.4 shows that the model fits the data well (fits of resistivity and phase curves from selected sites and misfit phase tensor maps for the remaining periods are also given in the supporting information Figure B.2 and Figures B.3-B.7 in Appendix B, respectively).
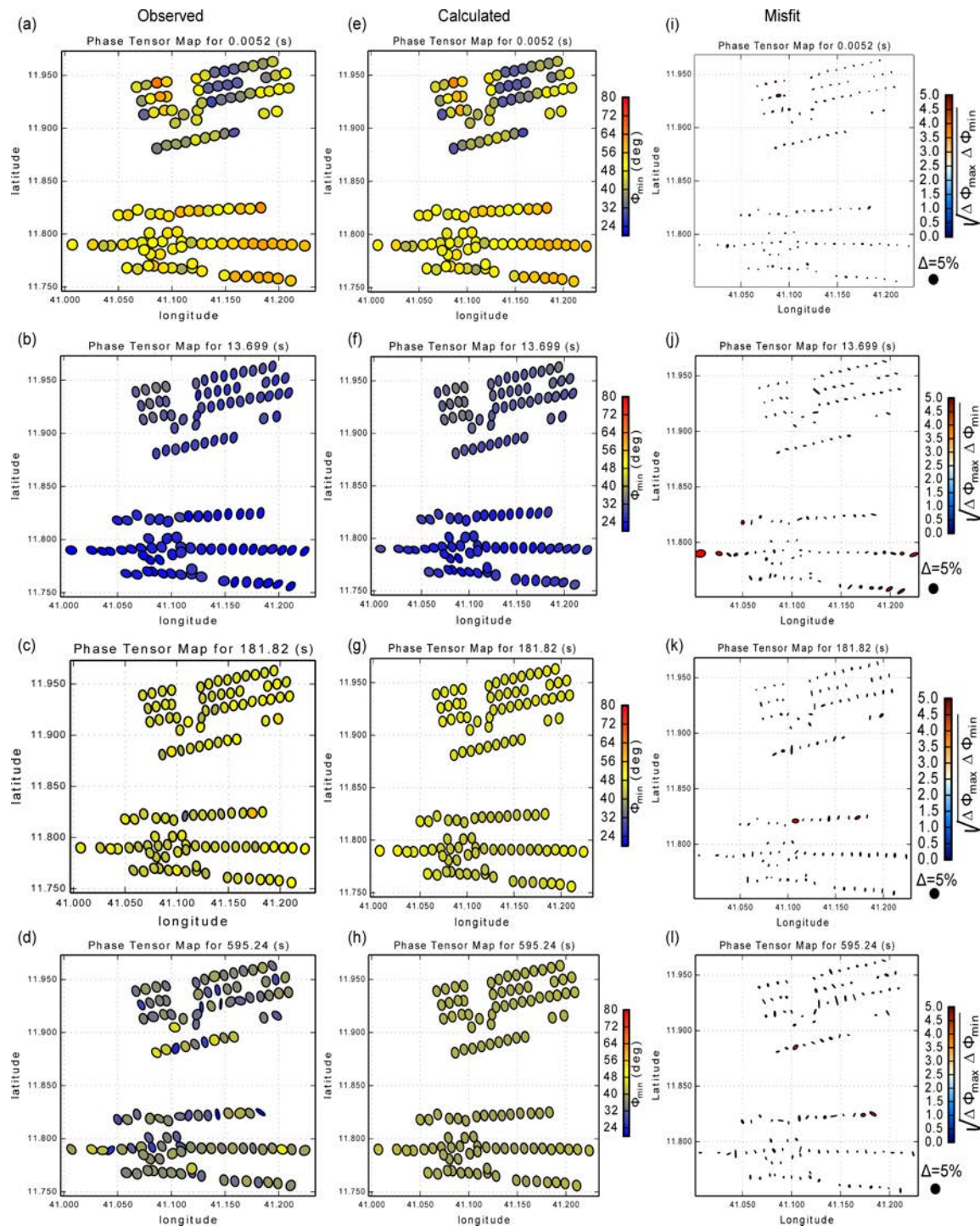
Figure 4.4: (a)-(d) phase tensor ellipses for selected periods of 0.05 s, 13.6 s, 181.5 s and 595.2 s. (e)-(h) calculated phase tensor ellipses from 3D inversion for respective periods in (a)-(d). The ellipses are colored by the minimum principal phase. (i)-(l) Tensor misfit ellipses for the observed and calculated inversion model. The ellipses are colored by percentage of the geometric mean of changes in maximum and minimum phases of observed and calculated phase tensors. The small size of ellipse indicates the misfit is small (reference ellipse is given on the legend).

4.3   Results and Discussion

The 3D preferred resistivity model of the Tendaho field is presented as resistivity cross sections and depth slices (maps). In Figures 4.5 and 4.6a, a surface layer can be identified that has very low resistivity ($< 10\,\Omega\,\text{m}$). This layer can be associated with thick sedimentary formation containing geothermal fluids and smectite and zeolite alteration mineralogy (Aquater, 1996a; Didana et al., 2014). The high resistivity zone (R1) at depth of $> 1.5\,\text{km}$ is interpreted as being due to the background resistivity of the Afar Stratoid Series basalts or chlorite-epidote alteration mineralogy (Figures 4.5 and 4.6b; Aquater, 1996a). The structure R1 is the deep reservoir of Tendaho geothermal system as confirmed by drilling of deep geothermal wells to a depth of $2\,\text{km}$ (Aquater, 1996a,b; Battistelli et al., 2002). A typical high temperature geothermal system is characterized by a high conductivity cap rock (smectite-zeolite zone, temperature $< 150\,\text{\textcelsius}$) underlain by a high resistivity reservoir (chlorite-epidote zone, temperature $> 220\,\text{\textcelsius}$) (Pellerin et al., 1996; Spichak and Manzella, 2009; Árnason et al., 2010; Muñoz, 2014). The Tendaho geothermal system also shows similar resistivity structure to other high enthalpy geothermal systems with thick sediments acting both as cap rock and shallow reservoir (Aquater, 1996a).
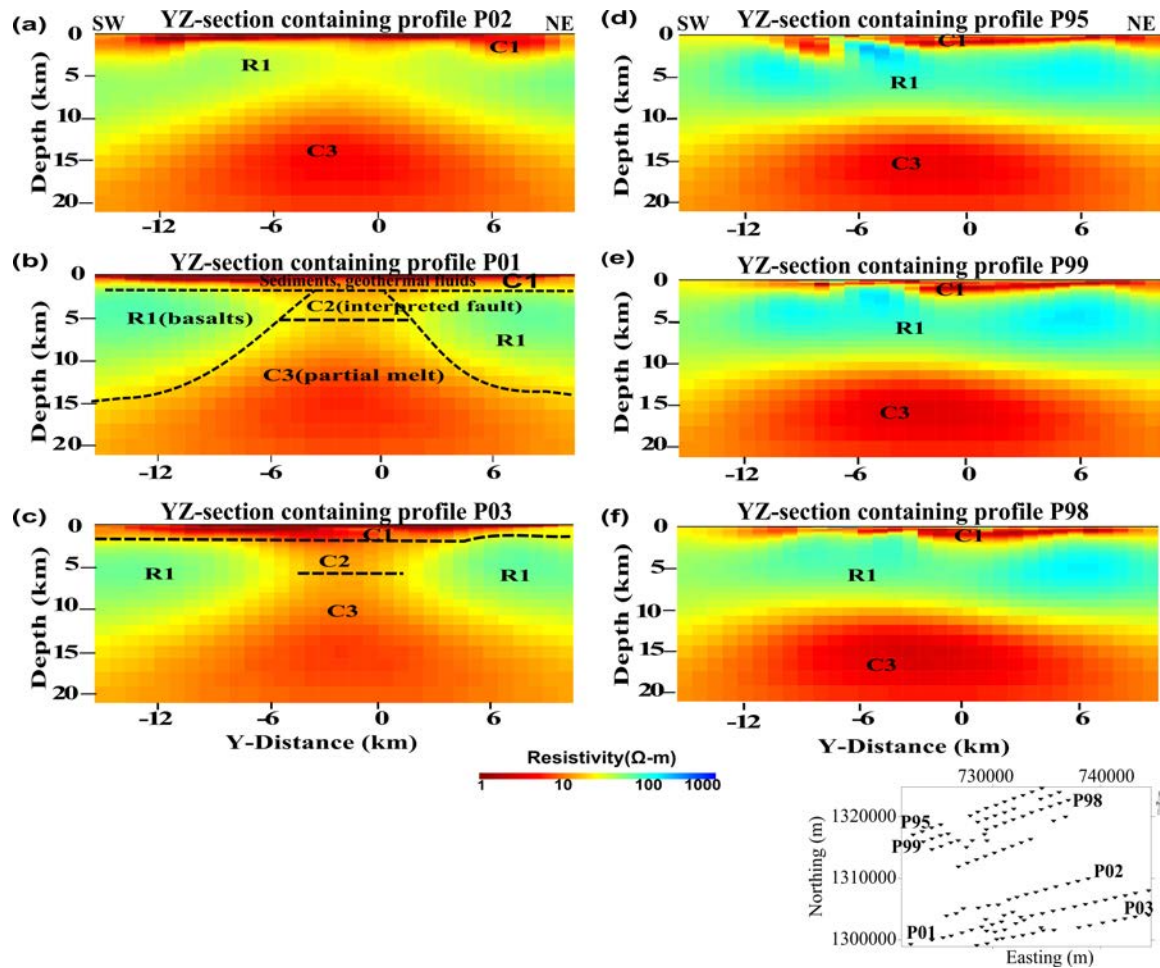
Figure 4.5: (a)-(c). Vertical resistivity sections through the 3D model which contain the southern profiles P02, P01 and P03, respectively. (d)-(f) vertical section which include the northern profiles P95, P99 and P98, respectively. The location map of the profiles is shown at bottom right corner.
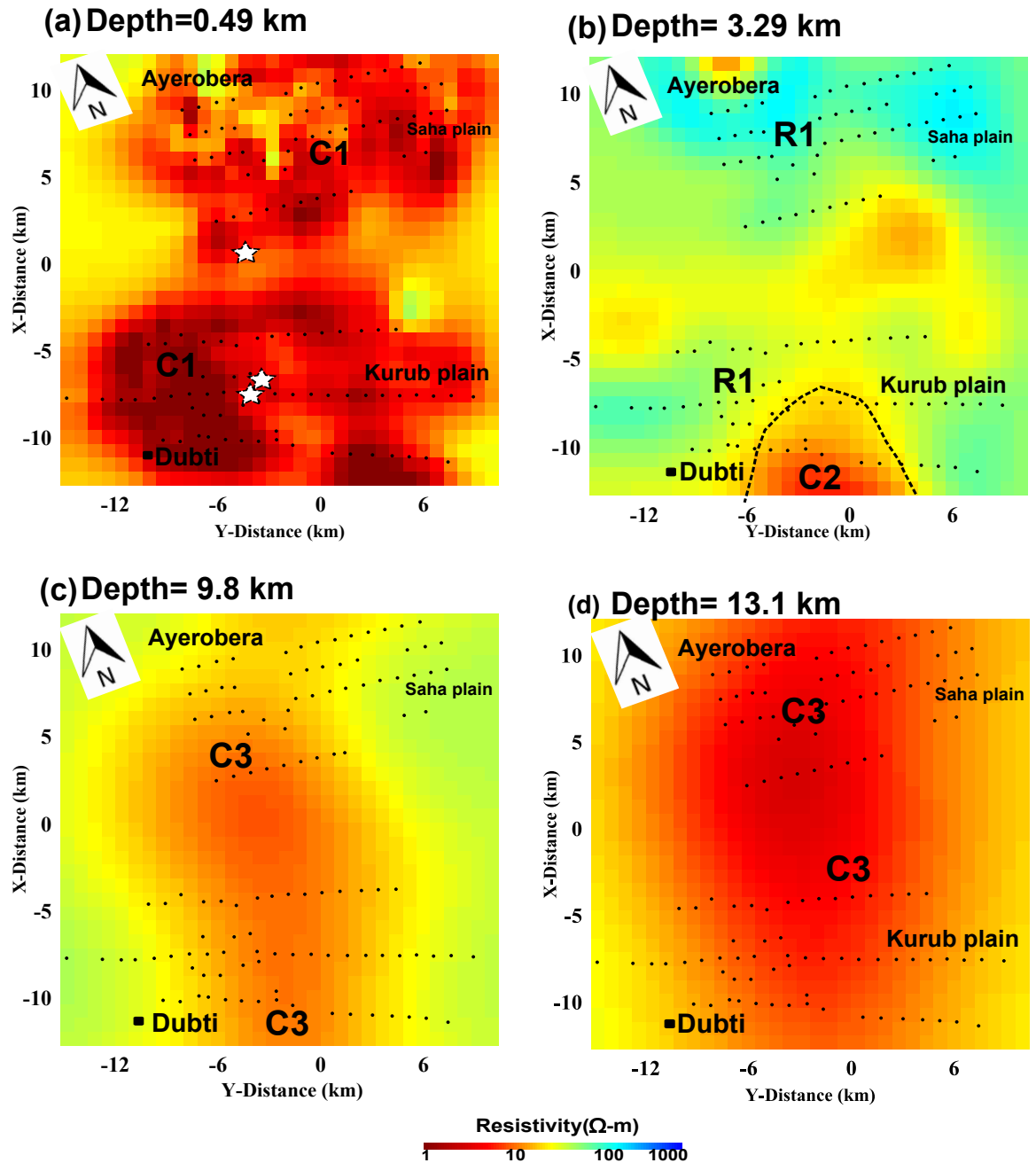
Figure 4.6: Model resistivity maps for layers at depth of (a) 0.49 km with thickness of 69 m (b) 3.29 km with thickness of 349 m (c) 9.8 km with thickness of 996 m and (d) 13.1 km with thickness of 1.325 km. C1, C2 and C3=high conductivity and R1=low conductivity. White stars=geothermal wells, black dots=MT sites.

The conductive structure (C2) with resistivity $<20\,\Omega\,\mathrm{m}$ at a depth of 1-5 km is interpreted as a fracture zone (fault) filled with hydrothermal fluid plumes or an upflow zone of the geothermal system (Figures 4.5b,c and 4.6b). The induction arrows in Figure 4.3 also show the presence of a

very conductive body southeast of the southern profiles (Parkinson convention). A conceptual model of Dubti geothermal field was constructed by Aquater (1996b) and Battistelli et al. (2002) using geochemical and geophysical data, reservoir engineering data and tectonic features (surface geothermal manifestations) (Figure 4.7a). The conceptual model indicated the presence of two upflow zones (fluid pathways) in the Afar Stratoid Series basalts in the vicinity of the exploratory wells TD2 and TD4 and well TD1 controlled by the regional fault structure "Dubti fault" (N125°E) and another inferred fault (N155°E) (Figure 4.7a). According to the model, the deep main fluid pathways are sub-vertical faults and these fluids recharge the shallow sedimentary sequence through sub-horizontal permeable zones (Aquater, 1996b; Battistelli et al., 2002). However, the 3D MT resistivity model reveals only one upflow zone (C2) SE of the exploratory wells, which coincides with the Dubti fault (Figure 4.7b). This regional structure was also identified by magnetic survey conducted at Tendaho (magnetics map of the survey area is given in the supporting information Figure B.8 in Appendix B).
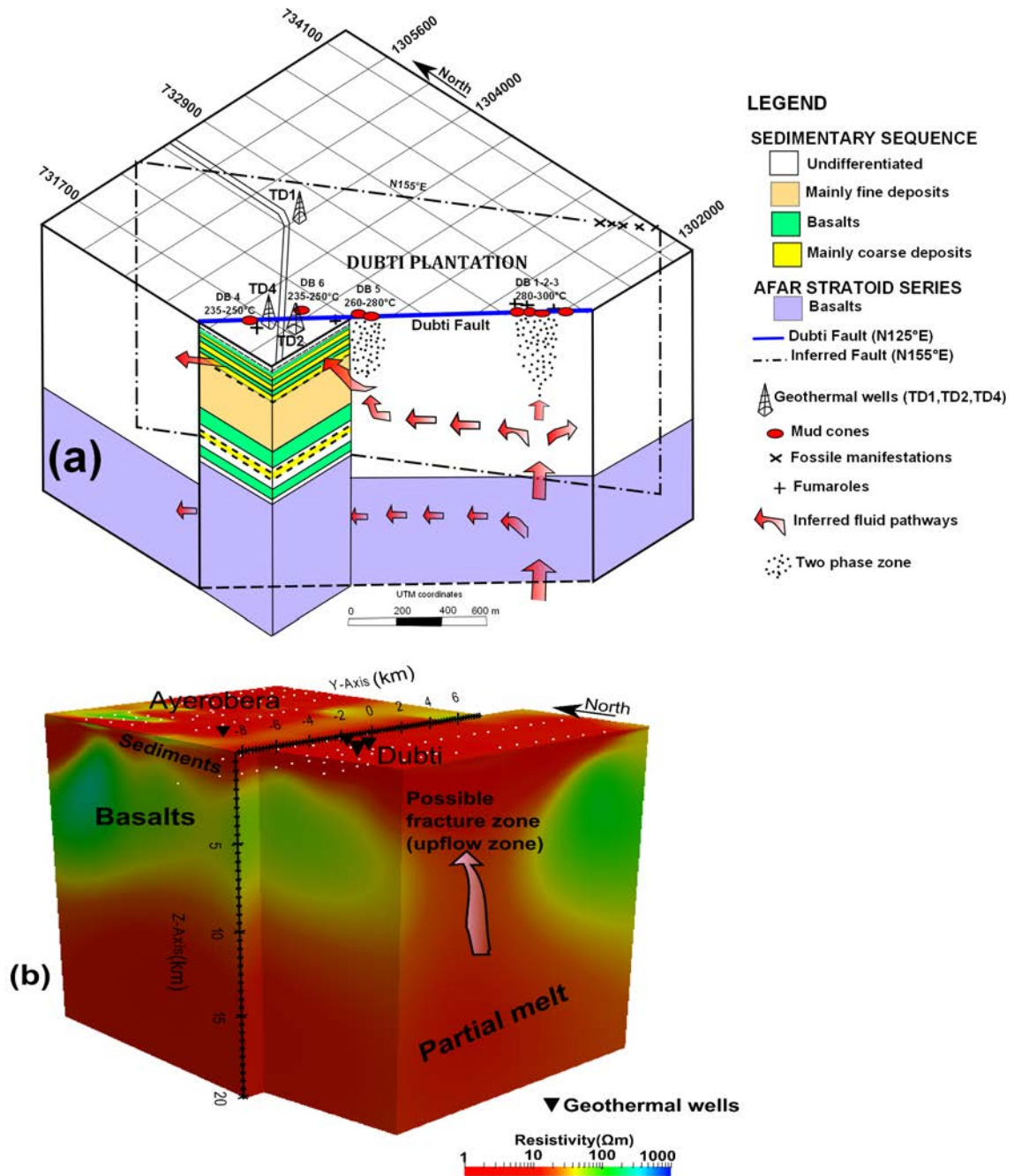
Figure 4.7: (a) Conceptual model of the Dubti geothermal system redrawn from (Aquater, 1996b; Battistelli et al., 2002) showing the inferred main fluid pathways. (b) 3D perspective view of the final 3D inversion model showing the possible fracture zone in the Afar Stratoid series basalts in Dubti area. White dots = MT sites.

The horizontal extent of C2 in the depth slice shown in Figure 4.6b shows that the exploratory wells at Dubti field were drilled in the outflow zone. In addition, the drilling of shallow and deep exploratory wells proved the

existence of two geothermal reservoirs in the Tendaho geothermal field (Amdeberhan, 1998; Battistelli et al., 2002). These comprise a shallow reservoir in the sedimentary formation (temperature 240-250 °C, depth 300 m–500 m) and a deep reservoir in the Afar Stratoid basalts (260-270 °C) (Amdeberhan, 1998; Battistelli et al., 2002). The deep reservoir in the basalts was found to be of low permeability due to deposition of hydrothermal alteration products in the rock matrix (Amdeberhan, 1998; Battistelli et al., 2002). Therefore, targeting the fracture zone or fault (C2) in the Afar Stratoid Series basalts by directional drilling is likely to increase the permeability and productivity of the deep reservoir. The lateral boundaries of C2 in the SE direction are not resolved with the current MT data set.

The high conductivity body (C3) at a depth of > 5 km is interpreted as being correlated with partial melt in the Afar Stratoid Series basalts (Figures 4.5 and 4.6c,d). This structure can be considered as the heat source of Tendaho geothermal system. Within the Tendaho graben, partial melt is a plausible explanation for the enhanced conductivity (Desissa et al., 2013; Didana et al., 2014). A melt fraction of about 13% by volume was estimated for C3 from the 2D resistivity model, and geochemical and borehole information (Didana et al., 2014). The geochemical analysis of gases in the geothermal fluids show carbon dioxide (CO_2) as the predominant species indicating a strong magmatic origin (Aquater, 1996a). A similar upper crustal partial melt is also observed at Krafla and Hengill high enthalpy geothermal fields in Iceland (mid-oceanic ridge) (Árnason et al., 2010; Gasperikova et al., 2011).

The 3D resistivity structure reveals similar structures in the Ayerobera and Dubti areas. However, the localized nature of the inferred fault (fracture zone) in the Dubti area suggests that the geothermal systems in the two areas are not connected. This argument is reinforced by the nature of the geothermal fluids observed in the two areas. The geothermal fluids from the Dubti area are of a water dominated sodium chloride type with high concentrations of sulphates, whereas the fluids from the Ayrobera area are steam dominated (lacking liquid phase) (Aquater, 1996a; Battistelli et al., 2002). According to isotopic study, the main recharge for the Dubti deep geothermal wells originates from the western Ethiopian

escarpments (2000-3000 m a.s.l elevations) (Aquater, 1996a; Battistelli et al., 2002). The gas composition studies at the Ayerobera area show lack of species such as H_2 and H_2S and predominance of CO and He which indicates stronger component of magmatic origin of geothermal fluids compared to the Dubti area (Aquater, 1996a; Battistelli et al., 2002). However, this does not necessarily mean that the two geothermal systems have separate heat sources.

4.4 Conclusions

The 3D MT conductivity model of Tendaho mostly resolves the deep geothermal reservoir under sedimentary cover not reached by previous DC resistivity surveys. The surface conductive layer (>1 km thick) is associated with sediments, lateral flow of geothermal fluids, and low temperature clay alteration (Aquater, 1996a). This conductive structure acts both as cap rock and shallow geothermal reservoir replenished by the deep basaltic reservoir. The high resistivity at a depth >1.5 km is correlated with the deep reservoir of the geothermal system (Aquater, 1996b; Battistelli et al., 2002; Muñoz, 2014). The 3D model confirmed the existence of a fracture zone (upflow zone) SE of the exploratory wells at the Dubti area which is associated with the "Dubti fault". Low permeability was encountered in the deep geothermal wells in the basalts due to deposition of hydrothermal alteration products in the rock matrix (Aquater, 1996a; Battistelli et al., 2002). The inferred fracture zone in the basalts represents an ideal target for future drilling due to its high permeability and high temperature. The lateral extent of the fracture zone is not resolved by the current MT data set. The other striking feature of the 3D MT model is the presence of the mid crustal conductor at depth of 10 km which spans the whole survey area. This structure indicates the presence of a large intrusive magmatic body under the Tendaho graben and Manda Hararo rift fed by deep mantle sources (Wright et al., 2006; Hammond et al., 2011; Desissa et al., 2013). A similar upper crustal magma reservoir is observed in other high temperature volcanic geothermal systems in extensional regimes (Árnason et al., 2010; Gasperikova et al., 2011). The presence of a geothermal fluid pathway via the inferred upflow zone, temperatures in excess of 270 °C at 2 km depth and

shallow magma reservoir makes the Tendaho geothermal fields an area of enormous potential for hydrothermal geothermal energy development (Battistelli et al., 2002; Teklemariam and Beyene, 2005). Densely spaced MT sites (300–500 m station spacing) and additional MT profiles SE of the inferred fracture zone will help in resolving the lateral boundaries of Tendaho geothermal field.

Acknowledgments

CHAPTER

FIVE

MAGNETOTELLURIC MONITORING OF PERMEABILITY ENHANCEMENT AT AN ENHANCED GEOTHERMAL SYSTEM PROJECT

DIDANA Y. L.[1], HEINSON G.[1], THIEL S.[1], AND KRIEGER L.[1].

[1]Electrical Earth Imaging Group, Department of Earth Sciences,
Department of Earth Sciences, University of Adelaide, Adelaide SA 5005, Australia

Statement of Authorship

Title of Paper	Magnetotelluric Monitoring of Permeability Enhancement at Enhanced Geothermal System Project
Publication Status	☐ Published ☐ Accepted for Publication ☑ Submitted for Publication ☐ Unpublished and Unsubmitted work written in manuscript style
Publication Details	Didana, Y. L., S. Thiel, G. Heinson, L. Krieger (2015), Magnetotelluric Monitoring of Permeability Enhancement at Enhanced Geothermal System Project, submitted to Journal of Geophysical Research: Solid Earth.

Author Contributions

By signing the Statement of Authorship, each author certifies that their stated contribution to the publication is accurate and that permission is granted for the publication to be included in the thesis.

Name of Principal Author (Candidate)	Yohannes Lemma Didana
Contribution to the Paper	Processed data, analysed , interpreted and wrote the manuscript
Certification:	This paper reports on original research I conducted during the period of my Higher Degree by Research candidature and is not subject to any obligations or contractual agreements with a third party that would constrain its inclusion in this thesis. I am the primary author of this paper.
Signature	Date 7/10/15

Name of Co-Author	Graham Heinson
Contribution to the Paper	provided valuable supervision of work, aided in data interpretation and critical analysis
Signature	Date 12/10/15

Name of Co-Author	Stephan Thiel
Contribution to the Paper	Planned survey, collected part of data, provided valuable supervision of work, aided in data interpretation and manuscript evaluation
Signature	Date 12/10/15

Name of Co-Author	Lars Krieger
Contribution to the Paper	Collected portion of data, provided Python scripts for data analysis
Signature	Date 12.10.15

Abstract

Magnetotelluric (MT) data were collected across the Habanero Enhanced Geothermal System (EGS) project in the Cooper Basin, South Australia. A baseline regional MT survey consisting of two profiles were collected to delineate the resistivity structure of the area. The second MT monitoring survey was conducted during fluid injection of the Habanero-4 well. Two dimensional (2D) inversions of the MT data reveal three main resistivity structures to a depth of $5\,\text{km}$. The low resistivity surface layer (about $1.5\,\text{km}$ thick) is interpreted as poorly consolidated sediments of Lake Eyre and Eromanga Basins. Below the conductive layer, a zone with relatively high resistivity with thickness of $2\,\text{km}$ can be correlated to consolidated Cooper Basin sediments. A high resistivity zone below depths of $3.5\,\text{km}$ is interpreted as the hot intrusive granodiorite (granite) of the Big Lake Suite with low porosity and permeability. This structure is also related to the Habanero EGS reservoir. The second MT survey was conducted during stimulation of Habanero-4, where about $36.5\,\text{ML}$ of water with a resistivity of $13\,\Omega\,\text{m}$ (at $25\,℃$) was injected at a relatively continuous rate of between 27–$53\,\text{L/s}$ over 14 days. Analysis of pre- and post-injection residual phase tensors show possible conductive fractures oriented in a N/NNE direction for periods greater than $10\,\text{s}$. Apparent resistivity maps also revealed that injected fluids possibly propagated towards N/NNE direction. This result is consistent with the propagation direction of micro-seismic events observed during fluid injection at the Habanero EGS, as well as the orientation of pre-existing N-S striking sub-horizontal fractures susceptible to slip on stimulation. The MT responses close to injection show on average a 5% decrease in apparent resistivity for periods greater than $10\,\text{s}$. The main reasons for observing subtle changes in resistivity at Habanero EGS are the screening effect of the conductive thick sedimentary cover (about $3.6\,\text{km}$ thick) and the presence of pre-existing saline fluids with a resistivity of $0.1\,\Omega\,\text{m}$ (equivalent to a salinity of $16.1\,\text{g/L}$ at $240\,℃$) in the natural fractures in the EGS reservoirs. This is further compounded by the physics of the problem, that is, the small volume of injected fluid compared to the large volume averaging by an MT sounding at the depth of interest. Analysis of time-lapse inversion models indicate an increase in total cumulative con-

ductance of about 25 S over a depth range of 2–5 km in the N-S direction compared to E-W direction for MT sites close to the EGS well, which likely indicate anisotropic permeability generated by the hydraulic stimulation. In conclusion, the MT monitoring at Habanero EGS highlights the need for favorable geological settings and/or controlled source methods and down-hole methods to measure significant changes in resistivity in EGS reservoirs.

5.1 Introduction

Enhanced geothermal systems (EGS) are unconventional geothermal resources with low permeability and relatively high temperature (typically $>200\,℃$), which require fluid stimulation to enhance hydraulic connectivity in existing fracture system (Audigane et al., 2002; Evans et al., 2005; Muñoz, 2014). A significant number of EGS potential resources occur around the world in varying geological settings (DiPippo, 2012; Ziagos et al., 2013; Bendall et al., 2014; Chamorro et al., 2014). The productivity of EGS reservoirs critically depends on the permeability of the fractures in the host rock.

Micro-seismics is the main geophysical method used to investigate fractures opened during hydraulic stimulation (Wohlenberg and Keppler, 1987; Baria et al., 2004; Cuenot et al., 2008; Cladouhos et al., 2013; Baisch et al., 2015). It gives information about opening of fractures; however, it does not provide information about fluid movement or fracture inter-connectivity (Cladouhos et al., 2013). On the other hand, magnetotellurics (MT) has been used to image electrically conductive fluid-filled fractures in EGS reservoirs to a depth of 4-5 km (Geiermann and Schill, 2010; Peacock et al., 2012, 2013; MacFarlane et al., 2014; Kirkby et al., 2015).

Peacock et al. (2012) and Peacock et al. (2013) used MT for monitoring the injection of 3.1 ML of saline fluids into an EGS reservoir at a depth of 3.6 km at Paralana, South Australia, over a period of 4 days. The MT responses from the pre- and post-injection data showed an average decrease of 10% and 5% in the two principal modes of impedance (Peacock, 2012; Peacock et al., 2013). Furthermore, using residual phase tensor analysis, Peacock et al. (2013) demonstrated that the injected fluids propagated along pre-existing fault system oriented in a NNE direction. The micro-seismic survey conducted at Paralana EGS showed fractures were inferred to have opened preferentially in a direction parallel to pre-existing fault systems (Hasting et al., 2011; Albaric et al., 2014). These studies showed the complementarity of MT and micro-seismics in characterizing fluid injection into EGS reservoirs. The current study is

building on previous studies at Paralana, to show that the technique can work in different geologic settings.

The Habanero EGS project is Australia's most advanced deep geothermal project and is located in South Australia about $800\,\mathrm{km}$ NE of Adelaide (Figure 5.1). The area is characterized by relatively high surface heat flow, with an average heat flow of $100\,\mathrm{mW}/m^2$ ascribed to high heat producing granites (Beardsmore, 2004; Meixner et al., 2012). Four EGS wells have been drilled into the hot granitic basement to a maximum depth of $4.3\,\mathrm{km}$ with a maximum downhole temperature of $244\,°\mathrm{C}$ (Hogarth et al., 2013). The Cooper and Eromanga sedimentary basins ($\sim 3.6\,\mathrm{km}$ thick) act as an insulating cap over the granitic EGS reservoir (Holl and Barton, 2015). The project area is characterized by a compressive stress field oriented approximately in E-W direction (Reynolds et al., 2005, 2006).
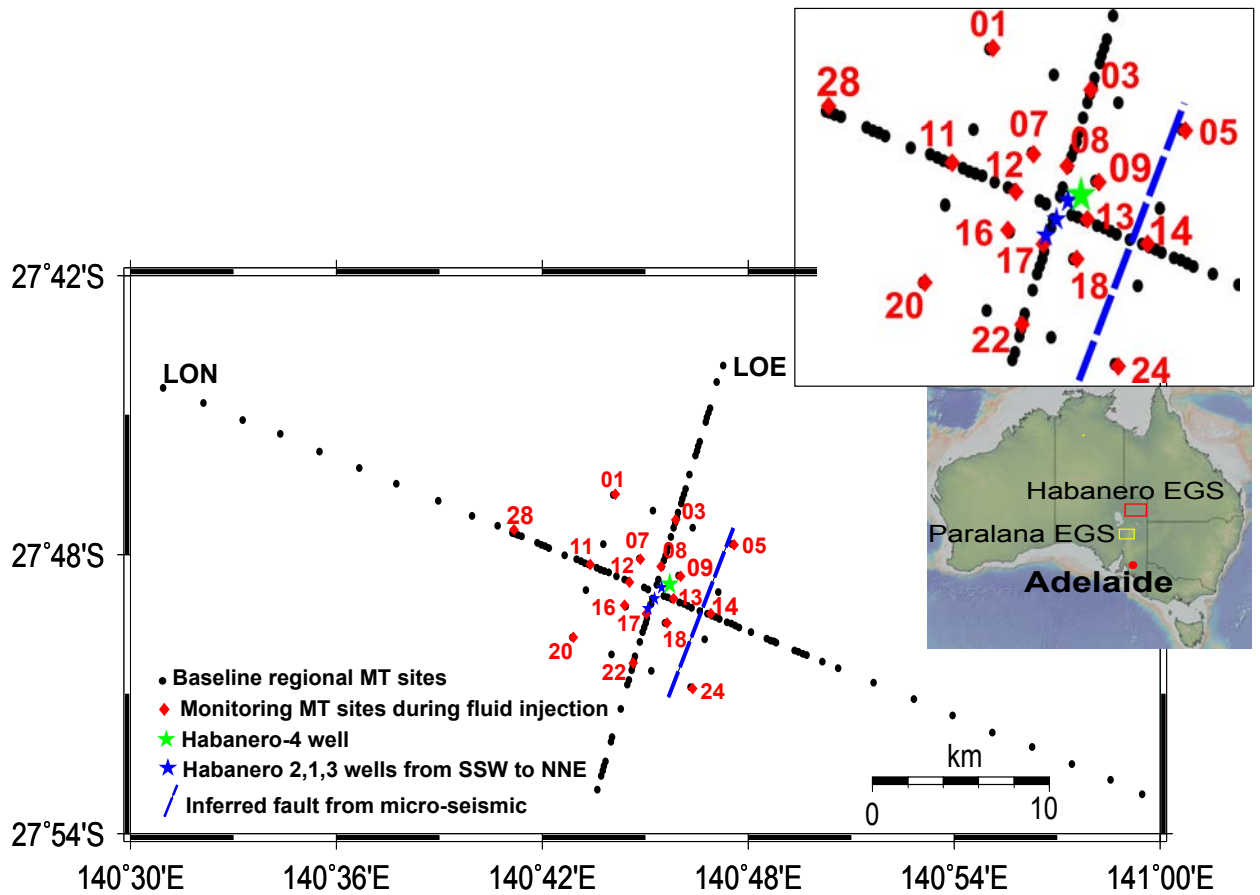
Figure 5.1: Location map of MT sites at the Habanero EGS located in South Australia. Black dots denote baseline regional MT stations acquired before stimulation by Quantec Geoscience Ltd in August, 2012. The red diamonds denote broadband MT stations acquired by University of Adelaide during fluid injection of the Habanero-4 well, which lasted for 19 days (November 15–December 3, 2012). Green star is the Habanero-4 well and blue stars are Habanero-2, 1, 3 wells from SSW to NNE, respectively. The red square on the inset map of Australia is the Habanero EGS project area. The yellow square on the inset map of Australia is the Paralana EGS project area. The central part of the location map is enlarged in size on the inset for visualization.

In November 2012, the Habanero-4 well was stimulated by injecting about 36.5 ML of near-surface aquifer-sourced water ($13\,\Omega\,\text{m}$ at $25\,°\text{C}$) over 14 days (Hogarth et al., 2013; McMahon and Baisch, 2013; Baisch et al., 2015; Holl and Barton, 2015). During the extended stimulation, 20200 micro-seismic events were located (McMahon and Baisch, 2013). The main target of the stimulation was a sub-horizontal fracture zone (~5–10 m thick and dipping 10° to the west south west) at a depth of

4077 m in the hot granitic reservoir (Bendall et al., 2014; Baisch et al., 2015; Holl and Barton, 2015; McMahon and Baisch, 2015). This sub-horizontal fracture zone (Habanero fault) is crossed by all Habanero EGS wells (McMahon and Baisch, 2013; Bendall et al., 2014; Baisch et al., 2015) and is the permeable reservoir of the Habanero EGS system.

The goal of this project is to use MT to monitor temporal and spatial changes in subsurface bulk resistivity structure caused by enhanced permeability due to injected fluids. We first collected a baseline regional survey along two profile lines before the fluid injection and created 2D resistivity models. Then we set out stations just before the injection and continuously collected data till 3 days after the hydraulic stimulation for a total of 19 days. We analyzed the monitoring data using resistivity maps versus periods, residual phase tensor and time-lapse inversion.

5.2 Geological and geophysical setting

The Cooper Basin is an intracratonic basin which contains late Carboniferous to middle Triassic fluvial and shallow marine sedimentary rocks and is located in the eastern part of central Australia (Hill and Gravestock, 1995; Meixner et al., 2014). The Cooper Basin sediments overlay the Warburton Basin (granitic basement) and are overlain by the Eromanga Basin and Lake Eyre Basin (Figure 5.2; Gatehouse et al., 1995). Together, Lake Eyre-Eromanga and Cooper Basins are about 3.6 km thick and act as a regional top seal (insulating cap rock) for the Habanero EGS, as revealed by geothermal and petroleum drilling (Delhi, 1984; Geodynamics, 2004). The Toolachee and Patchawarra units in the Cooper Basin, which have low mean thermal conductivities of 1.63 and 2.10 W/mK, respectively, act as the main insulating units (Figure 5.2; Meixner et al., 2012). The heat source for the Habanero EGS reservoir is the high-heat-producing granite of Big Lake suite characterized by a prominent low gravity anomaly in the Nappamerri Trough at about 3.6 km depth (Meixner et al., 2000; Moeck and Beardsmore, 2014; Meixner et al., 2014).
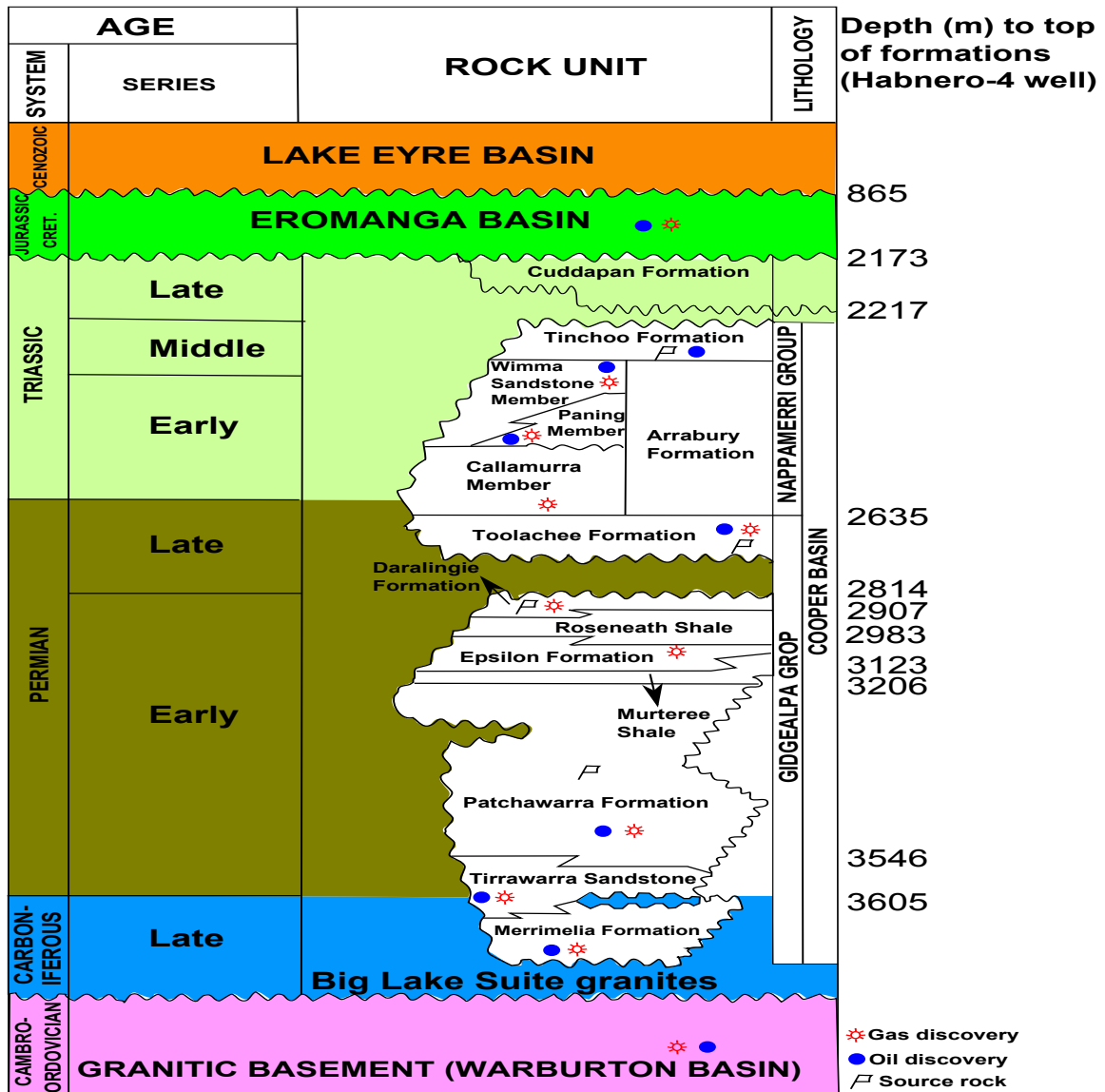
Figure 5.2: Stratigraphic summary of the Lake Eyre, Eromanga, Cooper, and Warburton Basins in South Australia modified from Hill and Gravestock (1995).

Four EGS wells (Habanero-1,2,3, and 4) were drilled to a depth greater than 4 km as part of the Habanero EGS project (Figure 5.1; McMahon and Baisch, 2013; Bendall et al., 2014). Intersecting the top of granitic formation at a depth of about 3.6 km; fluid injections have been run in all four Habanero wells with the volume of fresh and saline water totaling 79 ML (Hogarth et al., 2013). The natural permeable fractures encountered in the granitic basement during drilling contained over-pressured brine with resistivity of 0.1 Ω m (equivalent to a salinity of 16.1 g/L at

240 ℃) pressure in excess of about 34 MPa (Yanagisawa et al., 2011; Hogarth et al., 2013; Holl and Barton, 2015). Such over-pressured fluids caused mud-loss during drilling in the Habanero EGS wells. Tracer test analysis between the Habanero-1 and Habanero-4 doublet (700 m apart) indicated about 56% tracer recovery while the analysis between the Habanero-1 and Habanero-3 doublet (560 m apart) showed about 70% tracer recovery (Ayling et al., 2015). This test demonstrated the anisotropic nature of permeability in the reservoir, or that the Habanero reservoir is an open system (Ayling et al., 2015).

Orientation of maximum horizontal stress is variable in the Australian continent; it is not aligned parallel to the N-NNE absolute motion of the Indo-Australian plate and is likely controlled by plate boundary forces (Hillis and Reynolds, 2000; Sandiford et al., 2004; Hillis et al., 2008). The Cooper Basin region is characterized by a compressive stress field with maximum horizontal stress oriented in the east-west direction (Hillis and Reynolds, 2000; Reynolds et al., 2005). Image log and drilling data analysis at Habanero wells indicate a reverse faulting or over-thrust regime at the reservoir depth where the magnitude of the minimum horizontal stress, SH_{min}, is between the maximum horizontal stress, SH_{max}, and the vertical stress, S_v (Barton et al., 2013; Holl and Barton, 2015). The azimuth of the maximum horizontal stress, SH_{max}, is 82 ± 5° (Holl and Barton, 2015).

The hydraulic stimulation of Habanero-4 EGS well, which started on 17th November 2012, generated a seismic cloud with maximum area of about 3.8 km² and the thickness of the cloud was 100-150 m with location uncertainty of 68 m in the vertical direction at a depth of 4 km as shown in Figure 5.3 (McMahon and Baisch, 2013; Bendall et al., 2014; Holl and Barton, 2015; Baisch et al., 2015). The maximum recorded event magnitude was three. A linear boundary to the east of Habanero-4 well across which no micro-seismic event recorded was interpreted as the eastern boundary fault (Figure 5.3; Bendall et al., 2014; Baisch et al., 2015; Holl and Barton, 2015).
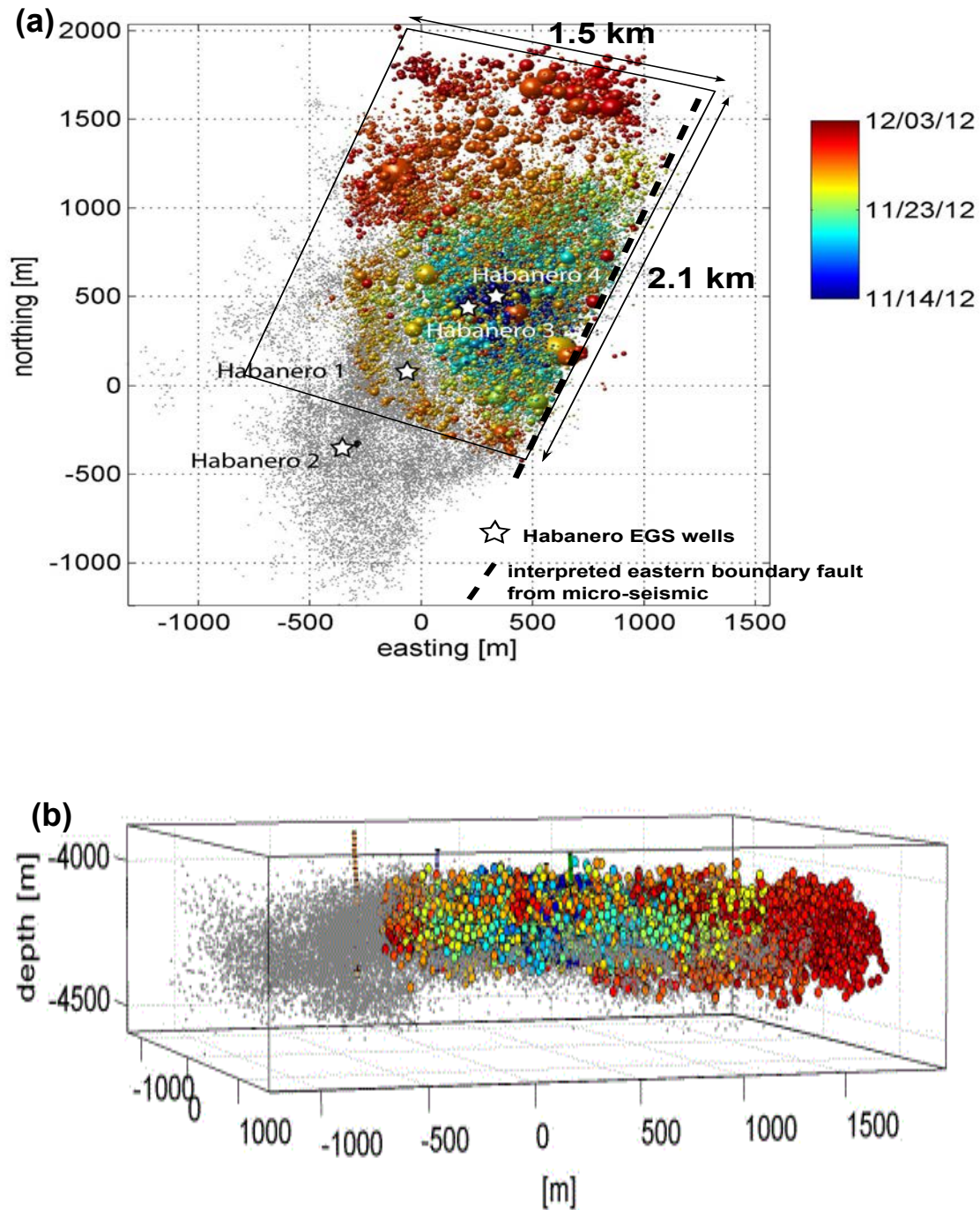
Figure 5.3: Hypocenter of the induced seismicity from the 2012 stimulation in the Habanero-4 well (McMahon and Baisch, 2013; Bendall et al., 2014; Baisch et al., 2015). (a) Lateral extent of the cloud propagating towards the north. (b) Vertical extent of the cloud. Color code denotes occurrence time in days. Previous seismic events (2003/05) are indicated by gray dots. The rectangular region in (a) was used in 3D forward modeling in Figure 5.9. The dashed line shows interpreted fault from micro-seismics.

5.3   Method

Magnetotellurics is a passive electromagnetic geophysical method used to investigate the distribution of electrical resistivity of the Earth (Chave and Jones, 2012). In the MT method, orthogonal components of natural horizontal electric $\mathbf{E}$ and magnetic $\mathbf{H}$ fields are measured simultaneously as a function of time and converted to frequency domain using Fourier transformation in order to determine the resistivity structure under the survey area. The horizontal electric and magnetic fields are related by the impedance tensor $\mathbf{Z}$ given by $\mathbf{E} = \mathbf{ZH}$. Apparent resistivity ρ_a as a function of frequency f is given by $\rho_a = (1/\mu\omega)|E_i/H_j|^2$, with $\omega = 2\pi f$ where μ is magnetic permeability and ω is angular frequency of the source signal. The electromagnetic skin depth (depth of investigation) is approximately $\delta(T) \approx 0.5\sqrt{T\rho_a}$ km, where ρ_a is apparent resistivity, or the average resistivity of an equivalent half space and T is the period in seconds. The complex impedance tensor can be written in terms of its real $\mathbf{X}$ and imaginary $\mathbf{Y}$ parts as $\mathbf{Z} = \mathbf{X} + i\mathbf{Y}$. Another way of representing the MT response is by the MT phase tensor, which is defined by the relation $\mathbf{\Phi} = \mathbf{X}^{-1}\mathbf{Y}$ and is not affected by galvanic distortion (Caldwell et al., 2004; Booker, 2014).

The electrical conductivity of rocks depends on many parameters such as water content, porosity, temperature, pore fluid salinity, alteration mineralogy, surface conductivity, and pressure (Sen and Goode, 1992; Ussher et al., 2000; Spichak and Manzella, 2009). In sedimentary rocks, the bulk electrical conductivity (σ_{bulk}) is empirically related to conductivity of water (σ_w) and porosity (ϕ) (Archie, 1942). The simplest form of Archies law is given by $\sigma_{bulk} = \sigma_w \, \phi^m = (1/F) \, \sigma_w$ where m is cementation factor varying between 1.4 to 2.2 and F is the formation factor ($F = \phi^{-m}$). Waxman et al. (1968), Flóvenz et al. (1985) and Flóvenz et al. (2005) demonstrated additional conductivity contribution due to clay minerals (for example, smectites, chlorite and montmorillonite) called surface (interface) conductivity (σ_s). The bulk conductivity equation can be rewritten as $\sigma_{bulk} = (1/F) \, \sigma_w + \sigma_s$. The bulk electrical conductivity (σ_{bulk}) of a consolidated formation with undamaged interconnected pore spaces during rock deformation can be estimated from the electrical conductivity of a fluid (σ_w) and the hydrologic permeability (k) by

using $\sigma_{bulk} = \sigma_w \, (k/\alpha)^{2/3} + \sigma_s$ with $\alpha = 1 \times 10^{-12} \, \mathrm{m}^2$ (Zhang et al., 1994; Spichak and Manzella, 2009).

Phase tensor residuals give information about geoelectric strike transformation during fluid injection and help to identify the direction of maximum change in current flow (Peacock et al., 2013; Booker, 2014). The residual phase tensor is calculated as

$$\Delta \Phi_{12} = I - \Phi_2^{-1} \Phi_1$$

where Φ_2, Φ_1, I are the phase tensor post-injection, the phase tensor pre-injection and the identity matrix of rank two, respectively.

A total of 135 MT soundings were acquired by Quantec Geoscience Ltd at the Habanero EGS project of Geodynamics in August 2012 as a baseline regional measurement (Figure 5.1). The MT sites were set up in two perpendicular profiles with infill sites in a square grid at the center of the Habanero EGS field (Figure 5.1). The MT soundings cover broadband frequencies in the range of 0.004 to 1000 s. Remote reference sites were established at a distance of 20 km to the NE of the survey area. The electric dipole length used was 200 m. High quality MT data were acquired from the Habanero Quantec survey. A typical resistivity and phase curve from the baseline regional survey is shown in Figure 5.4. The resistivity and phase curve show the 1D nature of the sounding and very small error bars. Static shifts observed on very few sites were corrected by moving a resistivity curve up or down by comparing it with neighboring sites and sticking the off-diagonal component resistivity curves together at the highest frequencies in WinGLink program (Rodi and Mackie, 2001).
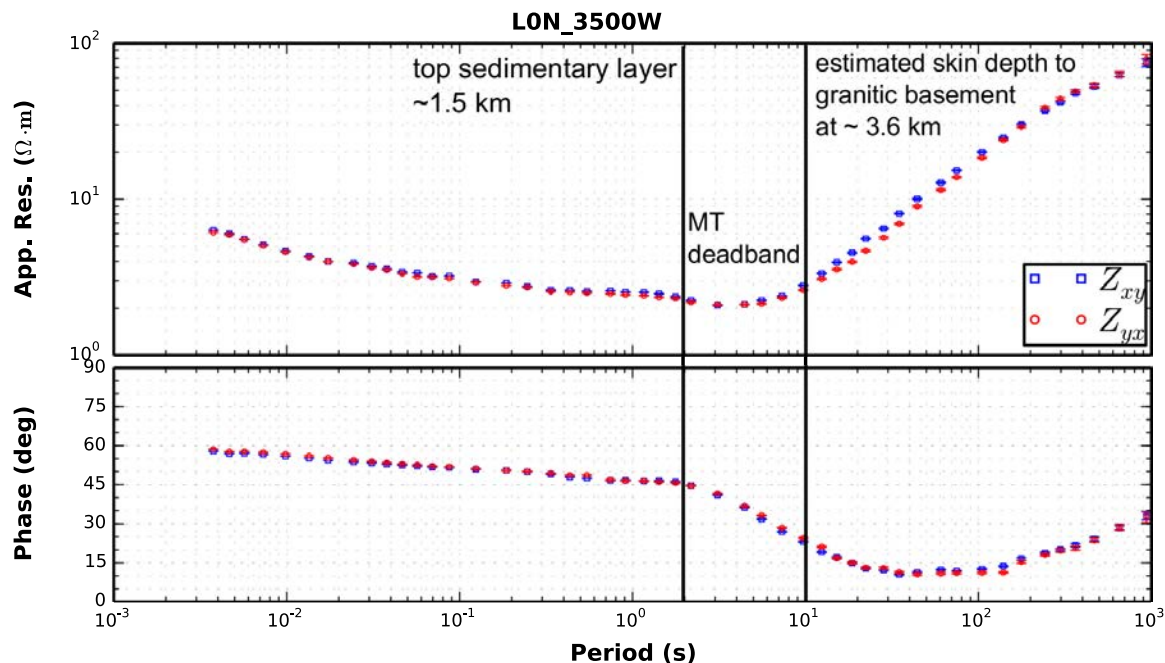
Figure 5.4: Example of resistivity and phase curves from the baseline regional survey. The blue squares and the red circles denote xy and yx components of resistivity and phases, respectively. The resistivity and phase curve show the 1D nature of the sounding.

The second time-lapse MT survey was conducted during fluid injection of the Habanero-4 well by Geodynamics Ltd over 14 days. The MT data recording was started two day before the fluid injection. The data were acquired from a total of 17 MT sites in a rectangular grid by the University of Adelaide using the AUSCOPE MT broadband instrument (Figure 5.1). At each site, data were continuously recorded at a sampling rate of 500 Hz covering a period range from 0.01 to 1000 s including pre-injection, during injection and post-injection for 19 days (15 November–3 December, 2012). The electrodes are Cu-$CuSO_4$ porous pots that hold an aqueous solution of $CuSO_4$ and they drain in few days after installation. The sites were briefly stopped for electrode replenishment every three days. The electric dipole length used was 50 m. The time series were processed using the robust remote reference processing BRIPP5 code (Chave and Thomson, 2004) resulting in good impedance estimates for periods of 0.01 s to 100 s except low quality data at the dead band for some sites. The processed MT data have a good repeatability across the successive days and small measurement error in

resistivity (about 1–2%) and phase (about 1–3%). However, few days of recordings of site 13, which is 650 m away from the Habanero-4 well, was affected by noise from the fluid injection operation. For this reason, the segments of the time series, where the activity of the operation was minimal, were selected for processing of site 13 MT data set. Static shifts observed at a single site on successive days were corrected by sticking the off-diagonal resistivity curves together at high frequencies in WinGLink program (Rodi and Mackie, 2001). A typical sounding curve from the time-lapse monitoring survey is shown in Figure 5.5.
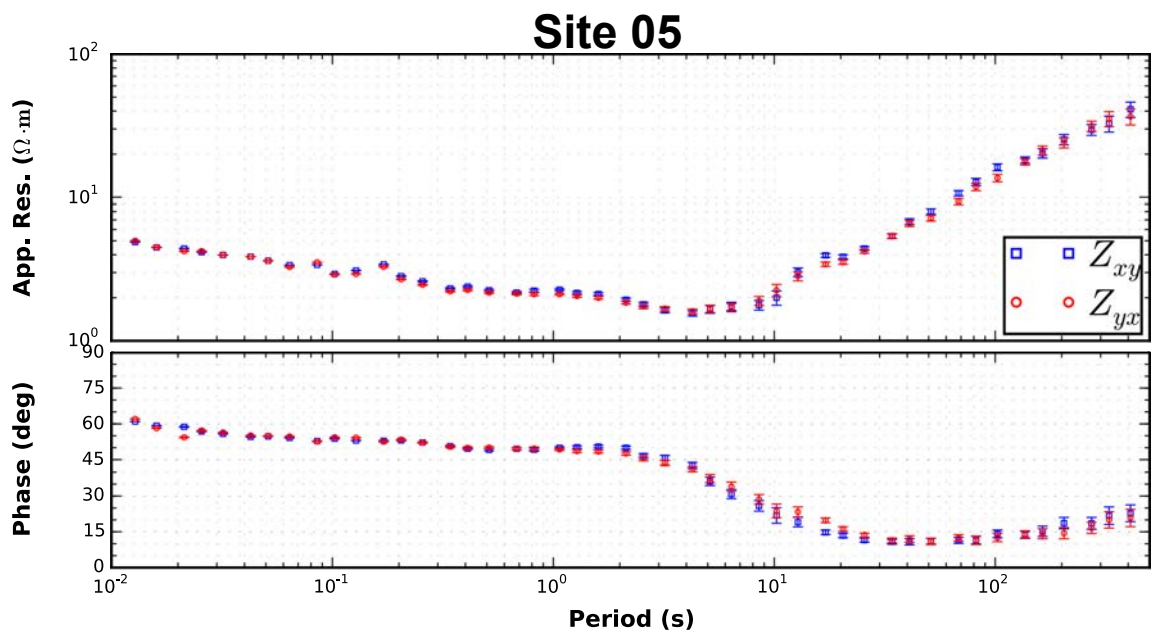
Figure 5.5: Example of a sounding curve for site 05 from the time-lapse MT monitoring survey. The blue squares and the red circles denote xy and yx components of resistivity and phases, respectively.

5.3.1   Dimensionality and strike direction analysis

The phase tensor pseudo-section of profile LON of the baseline regional survey at short periods of < 10 s (Figure 5.6a) shows circular ellipses with skew angles close to zero which is consistent with 1D resistivity structure (Caldwell et al., 2004). At periods of > 100 s, the major axes of the ellipses are aligned in NE direction and the skew angles are less than three degrees which suggests 2D resistivity structure (Caldwell et al., 2004).
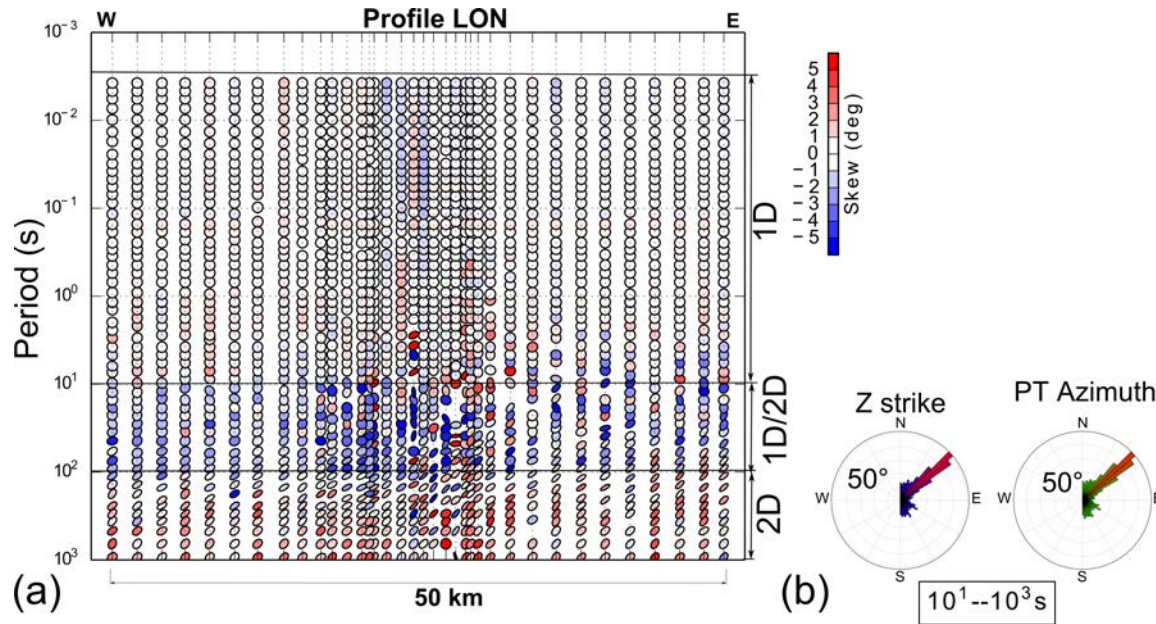
Figure 5.6: Phase tensor pseudo-section plot of profile LON shown in Figure 5.1 colored by the skew angles. For most sites, at long periods the skew angle is less than 3°, which is consistent with 2D regional conductivity structure. The major axis of the ellipse at long periods is aligned in a NE direction, which implies a possible geoelectric strike direction. (b) Rose diagram of strike angles showing strike estimated from the invariants of the impedance tensor (Z) (Weaver et al., 2000) and azimuth of phase tensor (PT) (Caldwell et al., 2004). 0° is north and 90° is east.

The geoelectric strike direction of the MT soundings was determined using the invariants of the impedance tensor (Z) (Weaver et al., 2000) and azimuth of the phase tensor (PT) (Figure 5.6b; Caldwell et al., 2004). The MT data show consistent strike of N50°E for the period range from 10–1000 s, as shown in Figure 5.6b.

5.4 Results

5.4.1 2D inversion of the baseline regional survey

The MT data were rotated to a strike direction of 50° for profile LON before the 2D inversions. The $x'y'$ component of the MT data is the transverse electric (TE) mode and the $y'x'$ component of the MT data is the transverse magnetic (TM) mode.

The MT data were inverted using the MARE2DEM 2D inversion code, which is a goal-oriented adaptive finite element code for MT that allows

an unstructured model grid (Key and Ovall, 2011). A total of 53 periods (0.004 s–655 s) were used for the inversion. Error floors of 5% and 3% were used for resistivities and phases for the inversion, respectively. Different 2D inversions of the MT data with different starting models were carried out. These include homogeneous half space of $5\,\Omega\,m$, $10\,\Omega\,m$ and a three layered Earth model based on resistivity logs (with resistivities and thicknesses of $3\,\Omega\,m/1600\,m$, $20\,\Omega\,m/1000\,m$ and a $100\,\Omega\,m$ half space). All the inversions resulted in similar models. At a depth of 3–4.5 km in the central part of the profile, a fine mesh grid was used in order to resolve possible structures in the EGS reservoir. The preferred model using a starting model of homogeneous half space of $10\,\Omega\,m$ from the joint inversion of TE and TM mode for profile LON with overall RMS of 1.5 is presented in Figure 5.7 (refer to Figure 5.1 for location of profile LON). The pseudo-section plots of the observed data and the model response from the inversions are given in the supporting information Figure C.2 in Appendix C. The model reveals three main resistivity structures to a depth of 5 km. The low resistivity structure surface layer (C), which is about 1.5 km thick, is associated with areas of poorly consolidated sands, siltstones and clay stones of Lake Eyre and Eromanga Basins. The intermediate resistivity structure (R1) can be correlated to consolidated sandstones, siltstones and shales of the Cooper Basin (natural gas and petroleum reservoir rocks). The high resistivity structure at depth of about 3.5 km (R2) is interpreted as the intrusive granodiorite (granite) of the Big Lake Suite with low porosity and permeability in the Warburton Basin (Meixner et al., 2000; Holl and Barton, 2015; McMahon and Baisch, 2015). This structure is also associated with the Habanero EGS reservoir. Results from the inversion of profile LOE, which was inverted using a geoelectric strike of N40°W, are given in the supporting information Figures C.3 and C.4 in Appendix C.
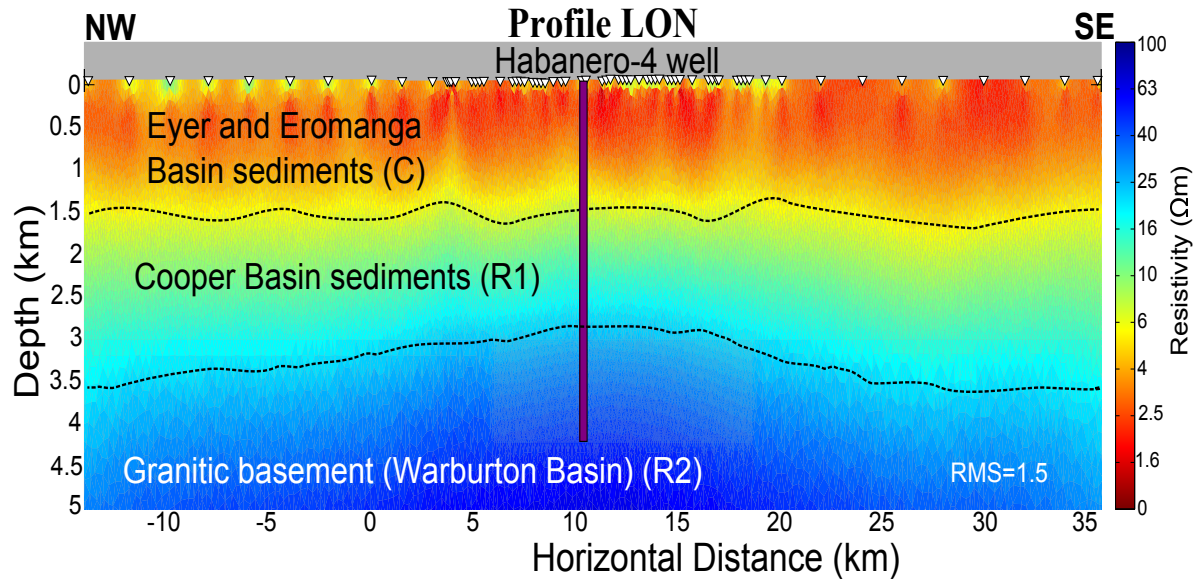
Figure 5.7: Preferred 2D resistivity model obtained by joint inversion of TE and TM modes data for profile LON with a RMS misfit of 1.5. C is a low resistivity layer. R1 is intermediate resistivity layer and R2 is a high resistivity layer.

5.4.2 Magnetotelluric monitoring of fluid injection

5.4.2.1 1D forward modeling and inversion

A 1D forward model was generated to test the sensitivity of MT to changes in conductance (product of conductivity and thickness) due to fluid injection at 4 km depth using the code OCCAM1DCSEM (Key, 2009). The resistivity logs from boreholes at Habanero were used to generate the base forward model (Delhi, 1984) (Figure 5.8a). The resistivity log data show an approximately three-layered Earth to a depth of about 3.8 km, and the trend was extrapolated to depth to generate the forward model (Figure 5.8a). The resulting resistivity and phase curves from the forward modeling are shown by the black curves in Figure 5.8b. To simulate the targeted fracture zone during fluid injection, a second forward model was run incorporating a layer with conductance of 100 S to the base model at 4 km depth (Figure 5.8a) and the resulting resistivity curve shows an average decrease in resistivity of about 10% after 10 s as shown in Figure 5.8b. The phase curve predicts the change at a period of about 3 s, as expected from the dispersion relation of resistivity and phase (Simpson and Bahr, 2005).
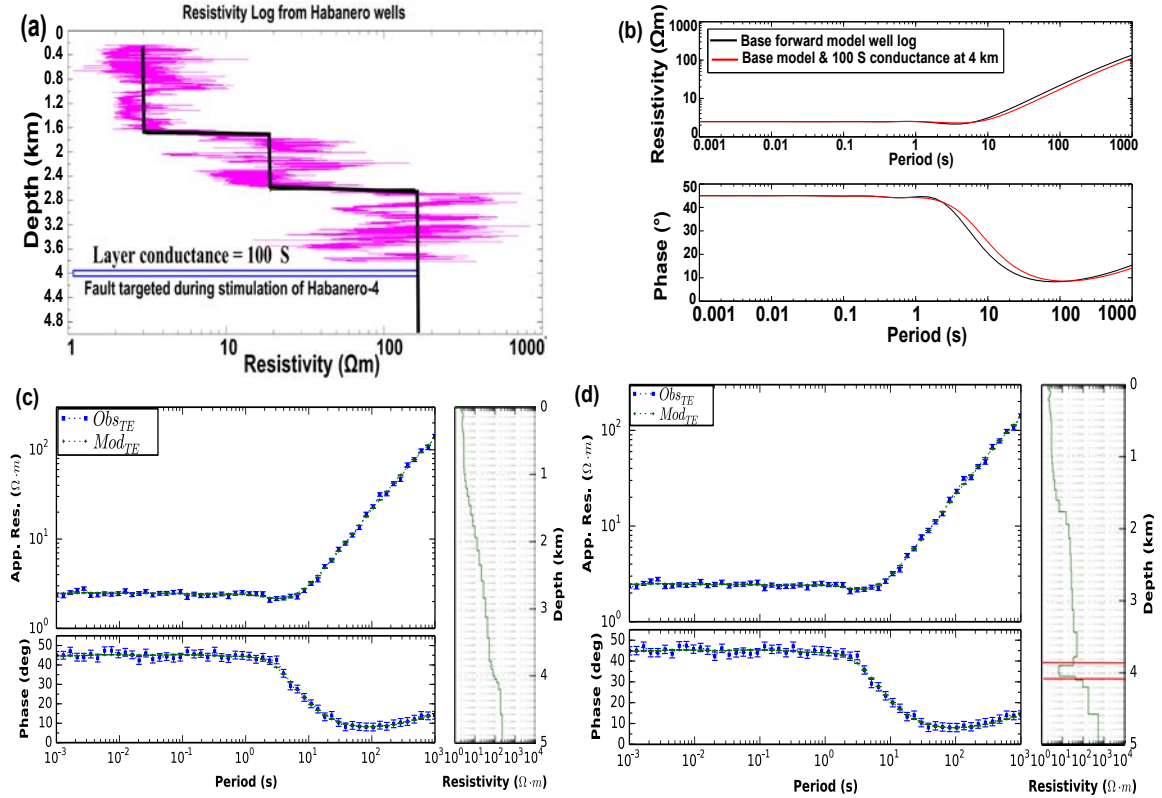
Figure 5.8: (a) Resistivity log used as a base model and a layer of conductance $100\,\mathrm{S}$ used to simulate a fracture zone at $4\,\mathrm{km}$. (b) Resistivity and phase curves from forward modeling (the black curve is the base model from well log, the red curve is base model plus a layer of conductance $100\,\mathrm{S}$ at $4\,\mathrm{km}$). (c) 1D unconstrained Occam inversion result from the resistivity and phase data from the base model and a layer of conductance $100\,\mathrm{S}$, shown by red curve in (b). (d) 1D constrained inversion result from the resistivity and phase data from base model and a layer of conductance $100\,\mathrm{S}$ shown by red curve in (b). The constrained inversion model, in which a preferred resistivity is set, recovers a layer with conductance of $100\,\mathrm{S}$ at $4\,\mathrm{km}$.

One dimensional unconstrained inversion and constrained Occam inversions were carried out on the base model data and $100\,\mathrm{S}$ layer in order to investigate the possibility of recovering the change in resistivity observed (Figure 5.8b red curve). Gaussian noise of 5% was added to the resistivity and phase data. The one dimensional unconstrained model using a starting resistivity of homogenous half space of $10\,\Omega\,\mathrm{m}$ with overall RMS of 1.0 shown in Figure 5.8c right panel failed to recover conductance of the stimulated fracture zone at a depth of $4\,\mathrm{km}$. However, the 1D constrained inversion model with overall RMS of 1.0, in which a preferred starting resistivity of $1\,\Omega\,\mathrm{m}$ with a thickness of $100\,\mathrm{m}$ was set at $4\,\mathrm{km}$ depth, recovers the conductive layer due to fluid injection at $4\,\mathrm{km}$ depth

(Figure 5.8d). These sensitivity tests show the difficulty of resolving resistivity changes at depth using smooth inversion routines.

5.4.2.2 3D forward modeling

A 3D forward modeling was carried out to investigate the amount of resistivity change expected in the Habanero EGS reservoir due to fluid injection. We used the parallelized 3D MT code ModEM (Meqbel, 2009; Egbert and Kelbert, 2012; Kelbert et al., 2014) for the forward modeling. The fluid injection was assumed to connected larger volume than the actual dimension of the targeted fracture zone (Habanero fault). Hence, the dimension of micro-seismic cloud was used as an anomalous volume for the forward modeling. The starting background resistivity model used was a four layer Earth obtained from the 2D models and borehole resistivity log data. The resistivities and thicknesses include layers of $3\,\Omega\,\mathrm{m}/1600\,\mathrm{m}$, $20\,\Omega\,\mathrm{m}/1000\,\mathrm{m}$, $30\,\Omega\,\mathrm{m}/1000\,\mathrm{m}$ and a $400\,\Omega\,\mathrm{m}$ half space (Figure 5.9a). A rectangular region corresponding to the seismic cloud of dimension $2.1\,\mathrm{km} \times 1.5\,\mathrm{km} \times 0.1\,\mathrm{km}$ in Figure 5.3 at $4\,\mathrm{km}$ depth was used to define the anomalous region created by fluid injection. The two tested scenarios for the anomalous region included an isotropic body of resistivity $0.1\,\Omega\,\mathrm{m}$ (assuming conductive formation fluids at 240℃) and an anisotropic body with maximum and minimum resistivities of $50\,\Omega\,\mathrm{m}/0.1\,\Omega\,\mathrm{m}$ embedded at $4\,\mathrm{km}$ depth (Figures 5.8a, b and c).
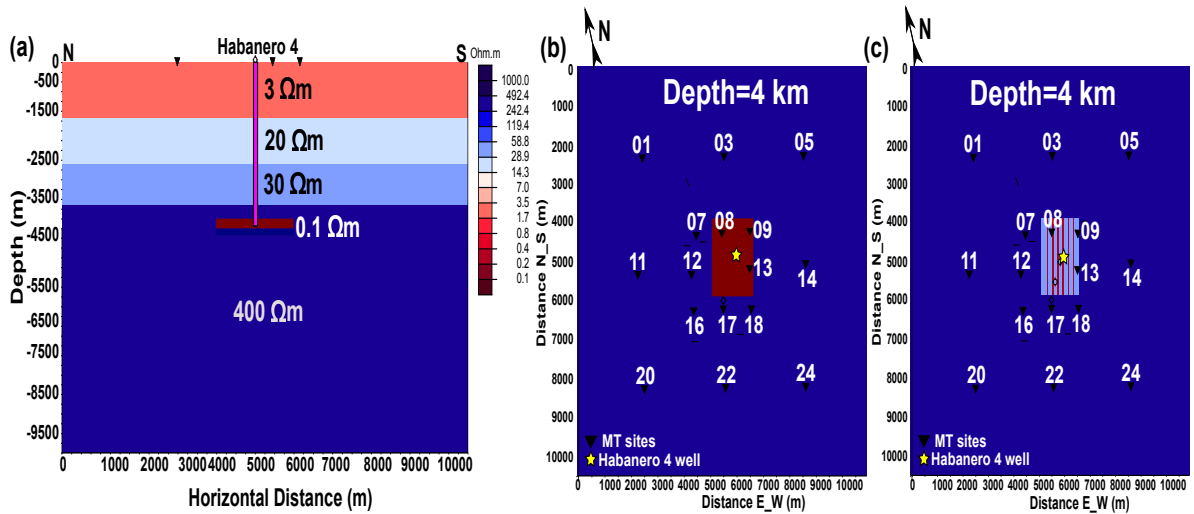
Figure 5.9: Resistivity model used in 3D forward modeling (a) xz section with $0.1\,\Omega\,m$ isotropic body embedded at $4\,km$. (b) xy slice of model for xz section shown in (a). (c) xy slice of anisotropic body with maximum and minimum resistivities of $50\,\Omega\,m/0.1\,\Omega\,m$ embedded at $4\,km$ depth.

A typical residual phase tensor map at a period of $17\,s$ for isotropic and anisotropic bodies embedded at $4\,km$ depth shown in Figure 5.9 is given in Figure 5.10. The residual phase tensor plots reveal the orientation, shape and magnitude of maximum change in the MT response that could be measured on the surface of the earth (Figure 5.10). The maps show maximum MT response change above the conductive isotropic block compared to the anisotropic block with ellipses oriented in the NNE direction.

A calculated maximum resistivity change of 6.7% and 2.7% is observed due to the presence of a conductive isotropic body and an anisotropic body embedded at $4\,km$ depth near the stimulated well, respectively (Figures 5.11a and b). In order to quantify the screening effect of the conductive sedimentary cover, a highly conductive $3\,\Omega\,m$ surface layer in Figure 5.9a was replaced with a $10\,\Omega\,m$ layer. The forward model run resulted in an 8% maximum change in resistivity close to the stimulated well for the isotropic model and a wider horizontal extent of change as shown in Figure 5.11c compared to Figure 5.11a.
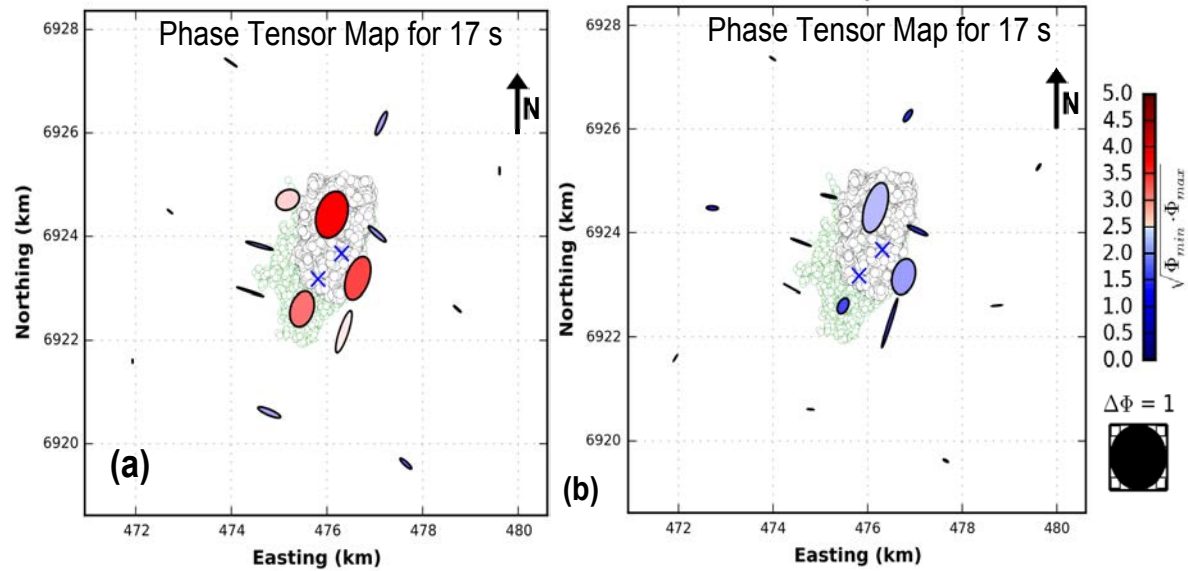
Figure 5.10: Residual phase tensor maps at a period of 17 s for: (a) $0.1\,\Omega\,$m isotropic body embedded at $4\,$km (b) anisotropic body with maximum and minimum resistivities of $50\,\Omega\,$m/$0.1\,\Omega\,$m embedded at 4 km depth. The maps show maximum MT response change above the isotopic body compared to the anisotropic block with ellipses oriented in the NNE direction. The ellipses are colored by percentage of the geometric mean of change in maximum and minimum phases. The ellipses are normalized by the maximum value of Φ_{max} for the data set. The green and black blobs at the background represent the seismic cloud from micro-seismic data collected during stimulation of Habanero-1 and Habanero-4, respectively. The blue × symbols are Habanero-1 (injection well towards southwest) and Habanero-4 (producer) wells.
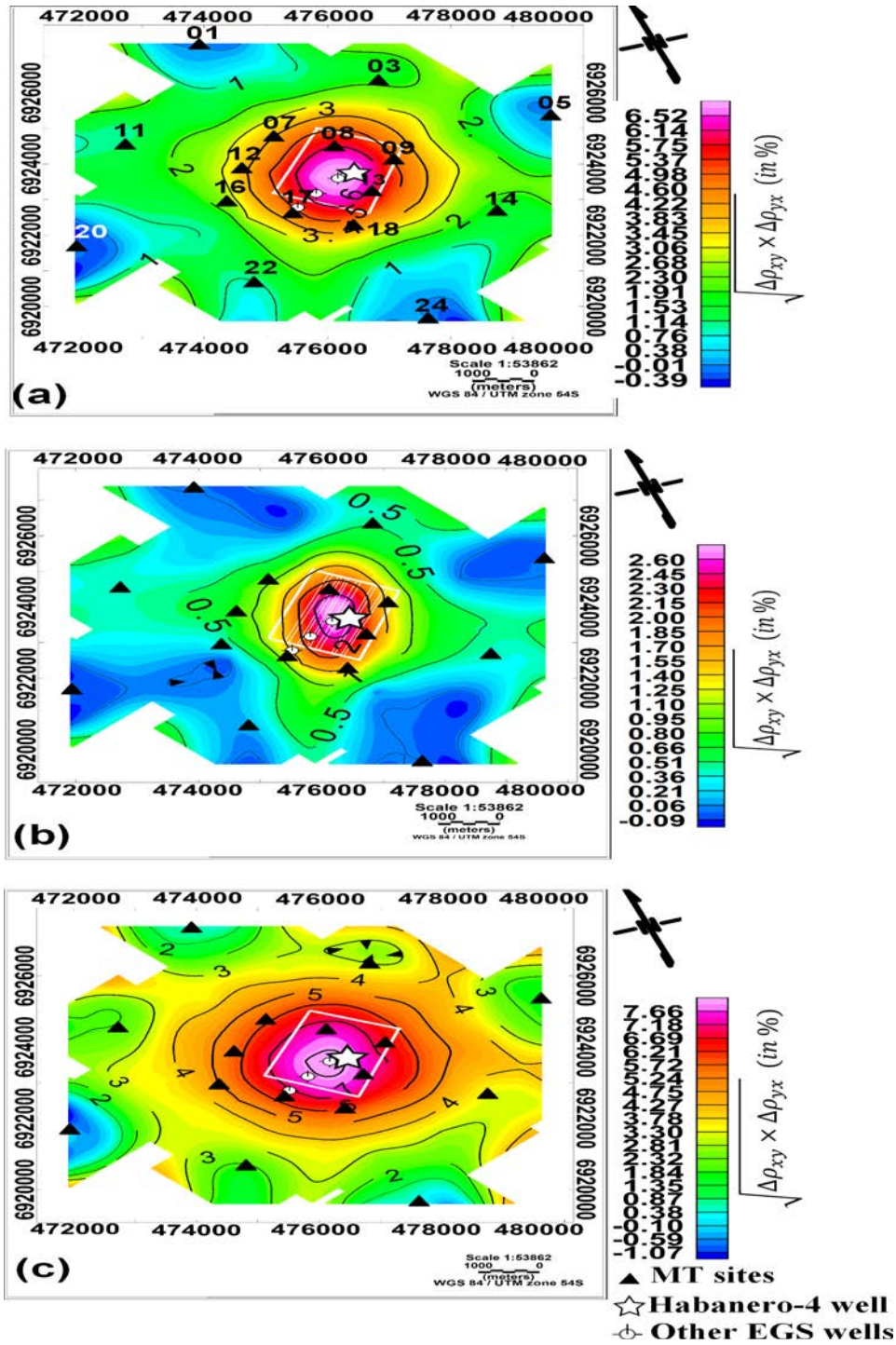
Figure 5.11: Contour map of percent change in resistivity at a period of 100 s: (a) 6.7% maximum resistivity change is observed close to the well due to presence of a conductive isotropic block $(0.1\,\Omega\,\mathrm{m})$ shown in Figure 5.9a, and b. (b) 2.7% maximum change in resistivity due to anisotropic body shown in Figure 5.9c. (c) A surface layer of resistivity $3\,\Omega\,\mathrm{m}$, in Figure 5.9a is replaced by $10\,\Omega\,\mathrm{m}$, and the resulting forward model for the isotropic body in Figure 5.9b shows 8% maximum change in resistivity near the well and wider horizontal extent of change compared to Figure 5.11a. The white rectangle shows the horizontal dimension of the anomalous body.

5.4.2.3   MT monitoring of Habanero EGS

A decrease in resistivity due to simulation of Habanero-4 well at $4\,\mathrm{km}$ depth is expected to occur at a period greater than $10\,\mathrm{s}$ using skin depth approximation. A typical resistivity phase curve for pre- and post-injection for site 09 which is located $870\,\mathrm{m}$ NE of Habanero-4 is shown in Figure 5.12 (refer to Figure 5.1 for location of site 09). The xy component of the resistivity curve shows on average a 5% decrease in resistivity values at periods greater than $10\,\mathrm{s}$ post-injection (Figure 5.12a). However, the yx component of resistivity curve shows on average a 1.5% decrease in resistivity in these periods post-injection (Figure 5.12b). This demonstrates the directional nature of the maximum current flow in the fractures.
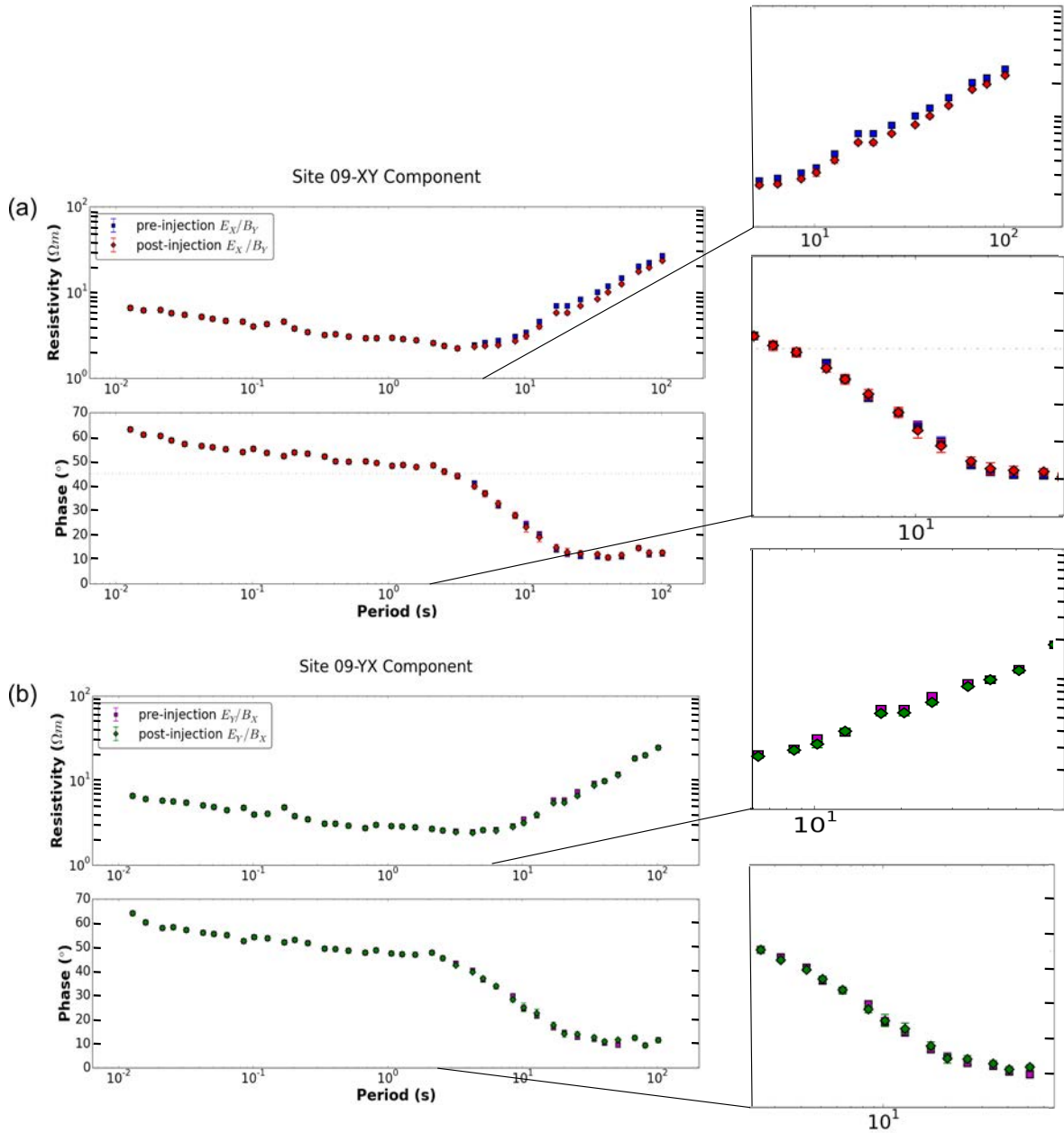
Figure 5.12: Resistivity phase curves pre- and post-injection for site 09. (a) xy component resistivity phase curve (b) yx component resistivity phase curve. The average decrease in resistivity for site 09 is about 5% in the xy component and 1.5% in the yx component at periods greater than 10 s post-injection. The blue and magenta squares are pre-injection curves. The red and green diamonds are post-injection curves.

Apparent resistivity maps of the xy component at selected periods of 0.05 s, 17 s, and 34 s for days 1, 5, 10 and 19 of time-lapse monitoring is shown in Figure 5.13. At a period of 0.05 s, all the resistivity maps of

the respective days show similar resistivity structure (Figure 5.13a-d). Regions labeled **"B"** with apparent resistivities of $< 3.3\,\Omega\,\mathrm{m}$ at period of $17\,\mathrm{s}$ and $< 6\,\Omega\,\mathrm{m}$ at period of $34\,\mathrm{s}$ in the NE sector on the resistivity maps show a decrease in resistivity for day 5, day 10 and day 19 (Figure 5.13f-h, k-m) compared to day 1 (Figure 5.13e,i) of the fluid injection monitoring surveys . However, regions labeled **"A"** with apparent resistivities $> 3.8\,\Omega\,\mathrm{m}$ at period of $17\,\mathrm{s}$ and $> 7\,\Omega\,\mathrm{m}$ at period of $34\,\mathrm{s}$, which are located in the NW and SE sector, do not reveal change in resistivity for day 5, day 10 and day 19 (Figure 13f-h,k-m) compared to day 1 (Figure 5.13e,i) of the monitoring surveys. The apparent resistivity maps show possible direction of propagation of the injected fluid towards N/NNE despite the change in resistivity is marginal.
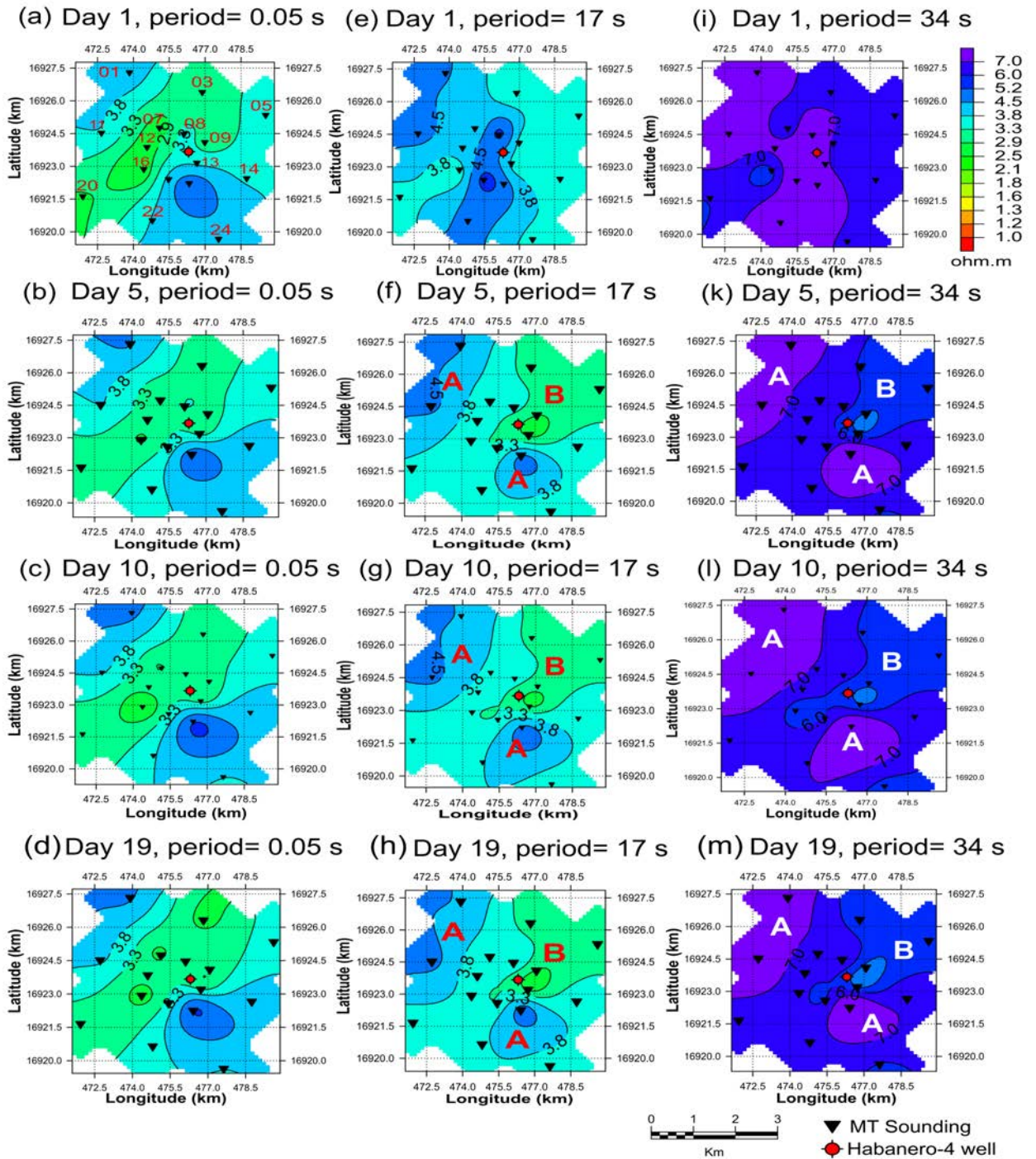
Figure 5.13: Apparent resistivity maps of the xy component for days 1, 5, 10 and 19 of time-lapse monitoring at selected periods of (a-d) 0.05 s, (e-h) 17 s, and (i-m) 34 s. Regions labeled **"B"** show change in resistivity for day 5, day 10 and day 19 compared to day 1. However, regions labeled **"A"** do not reveal change in resistivity for day 5, day 10 and day 19 compared to day 1. The inverted triangles are MT sites of time-lapse monitoring. The red circle is Habanero-4 well.

The calculated residual phase tensor maps reveal changes due to stimulation at periods of about 10 s and later. The residual phase tensor plots reveal the direction of maximum current flow with the major axis of the ellipses aligned in N/NNE direction for most sites (Figure 5.14). This result is consistent with the propagation direction of micro-seismic events during hydraulic stimulation of Habanero-4 as shown in Figure 5.3 (Bendall et al., 2014; Baisch et al., 2015; Holl and Barton, 2015; McMahon and Baisch, 2015).
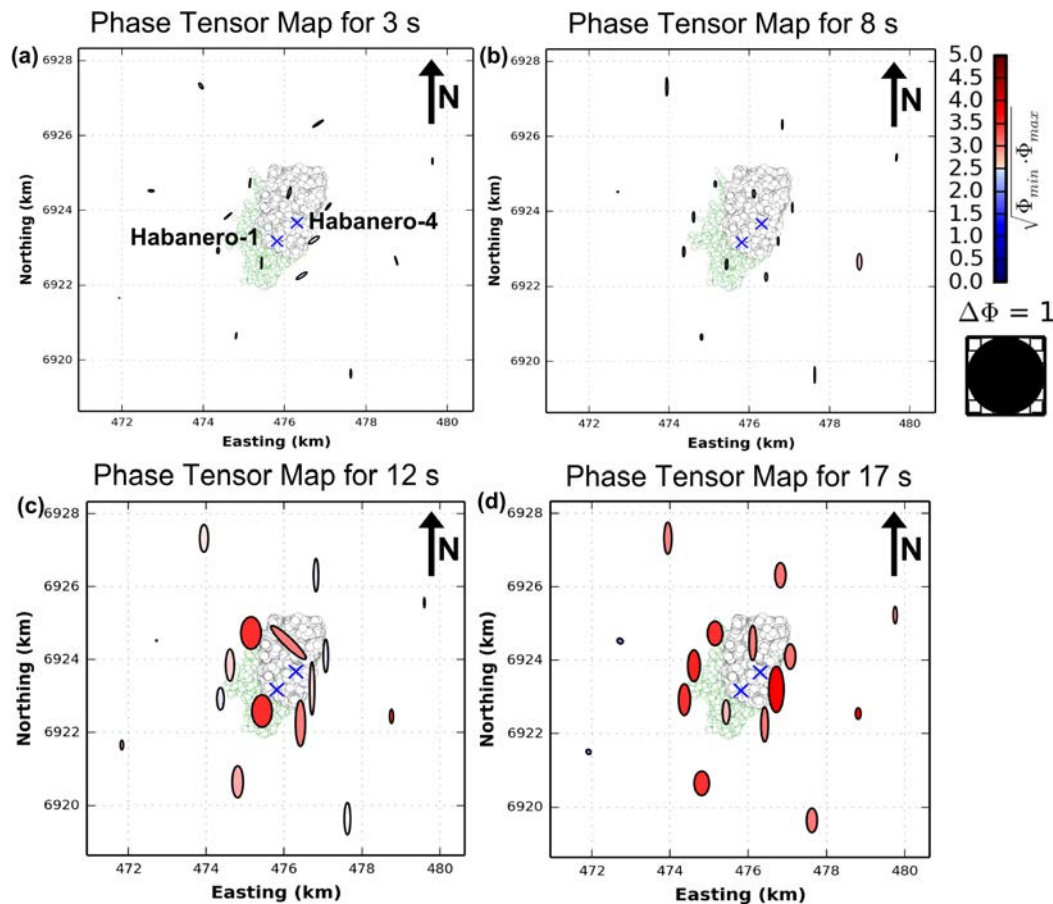
Figure 5.14: Maps of phase tensor residuals between pre- and post-stimulation measurements (a) at period of 3 s (b) 8 s (c) 12 s (d) 17 s. The green and black blobs at the background represent the seismic cloud from micro-seismic data collected during stimulation of Habanero-1 and Habanero-4, respectively. The seismic clouds of the two hydraulic stimulations overlap, with the 10% increment in north direction in 2012 (McMahon and Baisch, 2015). The blue × symbols are Habanero-1 (injection well towards southwest) and Habanero-4 (producer) wells. The ellipses are colored by percentage of the geometric mean of change in maximum and minimum phases. The ellipses are normalized by the maximum value of Φ_{max} for the data set.

There is uncertainty in the orientation of the major axis (α) of the ellipses as they are affected by the noise level in the data, especially in the dead band, where the signal strength is low. A typical example of the phase tensor uncertainty (Booker, 2014), that is calculated using propagation of errors on MT data recorded pre-injection and during fluid injection is given in Figure 5.15.
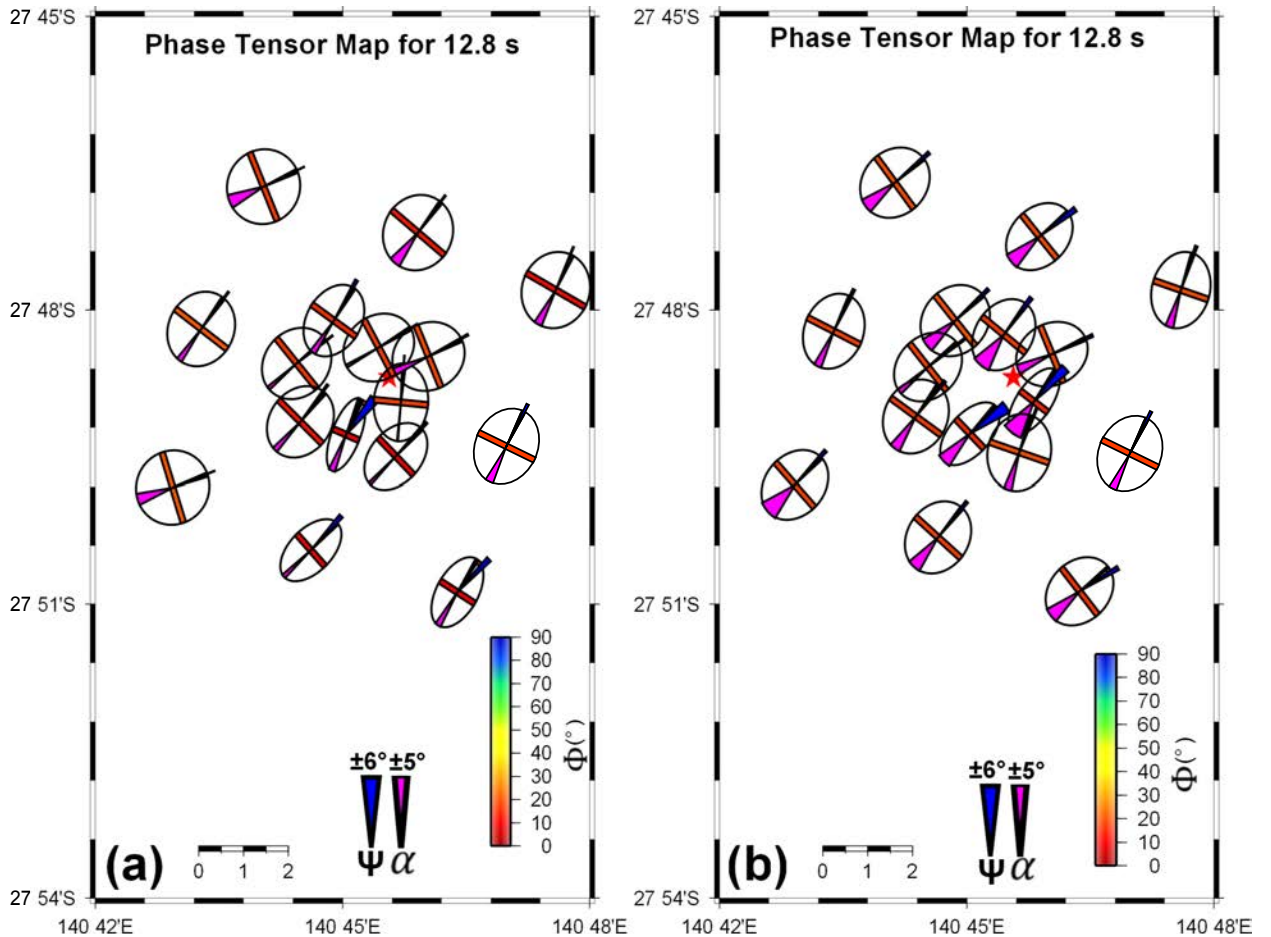
Figure 5.15: Phase tensor uncertainty maps at period of 12.8 s (a) pre-injection (b) during fluid injection. The uncertainty in normalized skew angles ($\Psi=2\beta$) is represented by blue fans. An uncertainty fan with ±6° is shown at bottom right corner for scale. The uncertainty in the orientation of the major axis (α) is shown by downward pointing magenta fans. An uncertainty fan with ±5° width is shown at bottom right corner for scale. The maps show the uncertainty in the orientation of the major axis (α) of the phase tensor ellipses increase due to low signal-to-noise ratio at the dead band during the fluid injection as shown in (b). The color of the ellipses minor axis indicate the minimum principal phase. The red star is Habanero-4 well.

5.4.2.4   Time-lapse MT inversions

A time-lapse 2D inversion of the MT data was carried out to gauge changes in resistivity due to fluid injection at a depth of 4 km. We inverted the time-lapse data from a single station (site 09), which is located 870 m NE of Habanero-4 well, using the 2D MT code MARE2DEM (Key and Ovall, 2011). To accommodate the fact that we are simulating resistivity with depth as a function of time, we incorporated the observed MT response in xy and yx components as the TE modes. Because almost all of the MT response change occurs in the electric field, and we are modeling this as being perpendicular to the time axes, the model best simulates 1D inversions smoothed with time. A total of 49 periods (0.01 s–600 s) were used for the inversion. An error floor of 10% for resistivity and 5% for phase was used for the inversion. Two dimensional inversions of the time-lapse MT data with different starting models were carried out and resulted in similar resistivity structure. Time-lapse inversion model using a starting model of three layered Earth from the resistivity logs is presented here. A differenced resistivity section between post-injection and pre-injection calculated from the final time-lapse model for the xy component resistivity for site 09 with RMS misfit of 1.2 is given in Figure 5.16 (the fit of the model site by site is given in the supporting information Figure C.5 in Appendix C). The resistivity section shows a decrease in resistivity of about $2\,\Omega\,\mathrm{m}$ above the measurement error between depths of 2 and 5 km post-injection (Figure 5.16). The smooth inversion used spreads the changes in resistivity over depths.
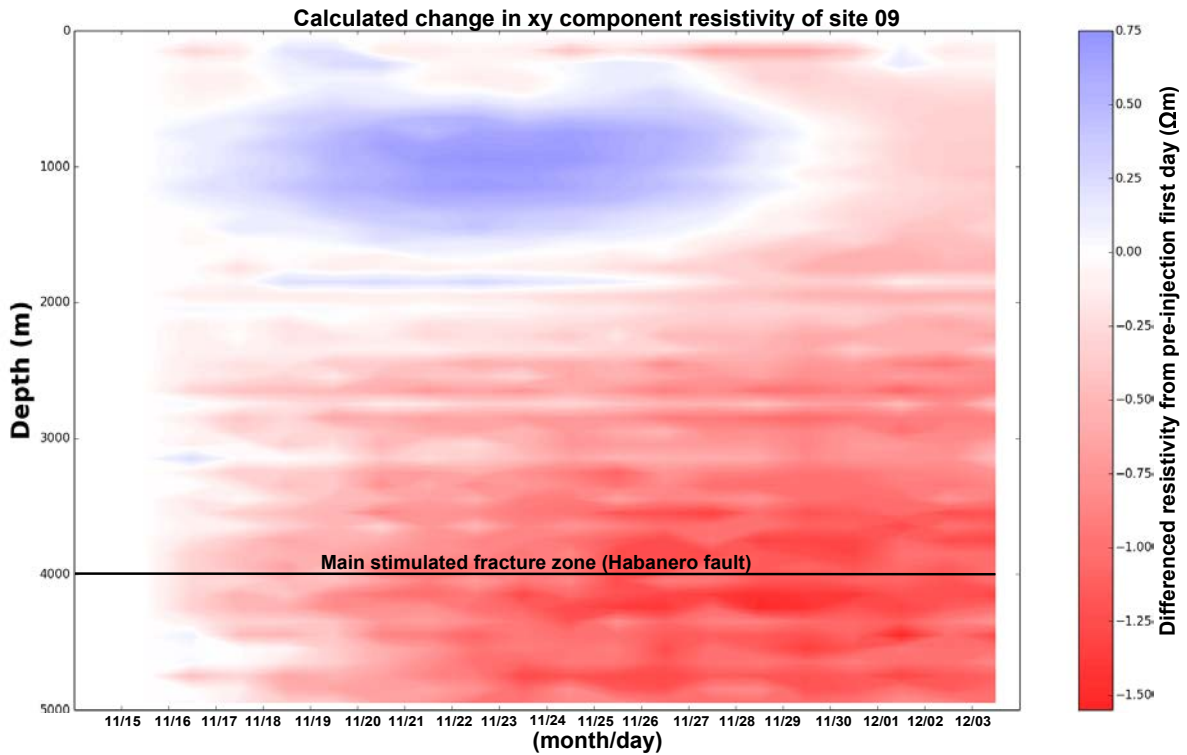
Figure 5.16: Calculated change in resistivity obtained from time-lapse 2D model of the xy component of resistivity by subtracting the consecutive days resistivity values from the pre-injection value (first day) for station 09 located 870 m NE of Habanero-4 EGS well.

Analysis of change in total conductance for the model obtained by subtracting from the first day pre-injection conductance values for depths between 2 and 5 km reveals 25 S increase in total conductance for the xy component of resistivity as shown in Figure 5.17a. The change in total conductance for the yx component remains stable for the overall injection period as shown in Figure 5.17a (the fit of the model is given in the supporting information Figure C.6 in Appendix C). This variation indicates the anisotropic nature of permeability in the fractures generated by the hydraulic stimulation. However, the change in total conductance of site 28 (which is located 7 km W of Habanero-4) obtained from a time-lapse model remains steady for both the xy and yx components of resistivity between depths between 2 and 5 km as shown in Figure 5.17b (refer to Figure 5.1 for location of site 28 and the fit of the models is shown in the supporting information Figures C.7 and C.8 in Appendix C). Tears and fixing resistivity layers above and below the injection depth smooth inversions were also tested. The models failed to converge and at the

same time did not recover the change in resistivity at the targeted EGS reservoir at 4 km depth. During the extended stimulation of Habanero-4, injection rates in the range from 27–53 liters per second (L/s) were achieved using injection pressures of 6300–7000 psi (Baisch et al., 2015; McMahon and Baisch, 2015) (Figure 5.17c).
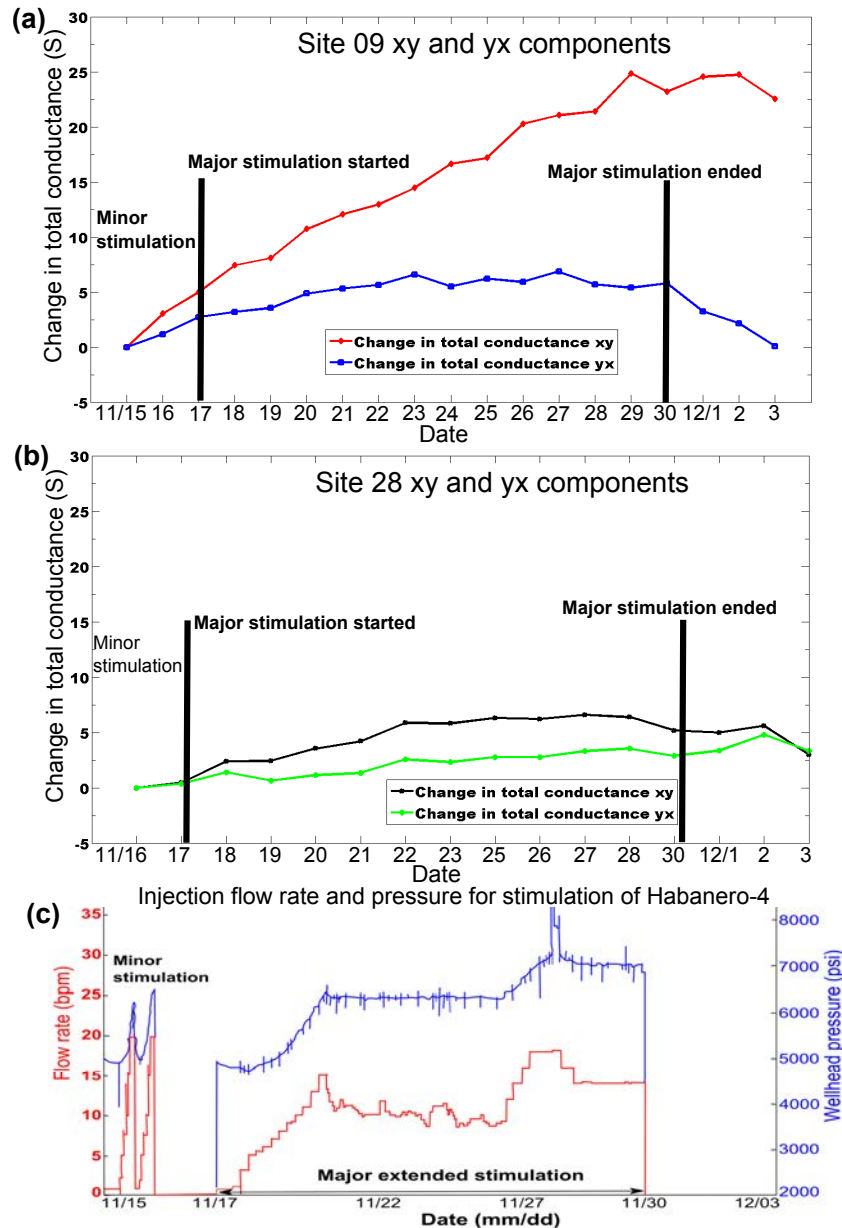
Figure 5.17: (a) and (b) Change in total conductance versus date calculated from xy and yx vertical columns of the 2D time-lapse resistivity models for depth range between 2 and 5 km for site 09 (which is located 870 m NE of Habanero-4 well) and site 28 (which is located 7 km W of Habanero-4 well), respectively. (c) Injection pressure and flow rate for the extended stimulation of Habanero-4 EGS well.

5.5   Discussion of results

The two dimensional model reveals three main resistivity layers to a depth of 5 km at Habanero EGS. The conductive surface layer (C) is associated with poorly consolidated sedimentary basins (Lake Eyre and Eromanga Basins) (Meixner et al., 2000). The relatively high resistivity layer (R1) is interpreted as consolidated sandstones, siltstone and shale of the Cooper Basin (Meixner et al., 2000). The high resistivity layer (R2) is related to the granitic basement EGS reservoir in the Warburton Basin (McMahon and Baisch, 2013). The 2D resistivity model did not uncover conductive faults to a depth of 5 km. This could be due to the small size of the natural fractures in the granitic basement which makes it difficult to be resolved by MT method. The resolution of MT decreases with increasing depth, as it is a diffusive geophysical method. This means that it is difficult to resolve small geological structures (fractures) at great depths which can sometimes be characterized better with anisotropic modeling (MacFarlane et al., 2014; Kirkby et al., 2015). The Habanero MT data do not exhibit an anisotropic nature. However, the micro-seismic survey indicated the presence of a possible eastern boundary fault or contact across which no micro-seismic event occurred (Holl and Barton, 2015).

The most crucial factor to continuous time-lapse MT monitoring survey is acquiring an accurate data with high signal-to-noise ratio (Peacock et al., 2013). Good quality MT data were acquired from the Habanero EGS monitoring survey with measurement error of less than 2% in resistivity in the period range from 0.01 s to 100 s. Static shifts observed in few MT sites were also corrected.

The micro-seismics survey showed the growth of the Habanero EGS reservoir towards the N/NNE by 4 km^2 due to the 2012 hydraulic stimulation (McMahon and Baisch, 2013; Baisch et al., 2015; Holl and Barton, 2015; McMahon and Baisch, 2015). Both the continuous monitoring MT data from Habanero EGS and forward modeling tests suggest that a decrease in resistivity of less than 10% due to stimulation. The Habanero monitoring MT data showed on average a 5% decrease in apparent resistivity values for periods greater than 10 s. Forward modeling of the

observed micro-seismic cloud dimensions using isotropic and anisotropic bodies embedded at 4 km depth showed 6.7% and 2.7% maximum change in resistivity in the EGS reservoir, respectively. The most likely expected reservoir permeability is anisotropic with ratio of 2:1 in N-E directions at Habanero EGS (Holl and Barton, 2015; Llanos et al., 2015). Analysis of the 2D time-lapse inversion models of MT sites also show a greater increase in total cumulative conductance following injection in the xy component of resistivity compared to the yx component of resistivity.

The main reasons for observing subtle changes in resistivity at Habanero EGS are the screening effect of the conductive thick sedimentary cover (about 3.6 km thick) and pre-existing saline fluids with resistivity of $0.1\,\Omega\,\mathrm{m}$ (equivalent to salinity of 16.1 g/L at 240 ℃) in the natural fractures in the EGS reservoirs reducing the achievable resistivity contrast from the hydraulic stimulation (Yanagisawa et al., 2011; Hogarth et al., 2013; Meixner et al., 2014; Holl and Barton, 2015). In addition, the overall resolution of MT decreases with increasing depth. A similar MT monitoring survey conducted at Paralana EGS resulted in a 10% average decrease in resistivity at a 3.6 km depth using a saline fluid of resistivity $0.3\,\Omega\,\mathrm{m}$ (Peacock et al., 2013). The stimulated reservoir in Paralana EGS consists of neo-Proterozoic meta-sediments and Mesoproterozoic basement rocks which are different from the granitic formation with low porosity and permeability targeted at Habanero (Meixner et al., 2000; Peacock et al., 2013; Meixner et al., 2014; Holl and Barton, 2015; Llanos et al., 2015).

Residual phase tensor ellipse plots indicate a N/NNE orientation as the direction of maximum fluid filled fracture connectivity due to fluid injection. Apparent resistivity maps at periods of 17 s and 34 s also show the injected fluids likely propagated towards N/NNE direction. This result is consistent with the propagation direction of seismic events and the orientation of pre-existing N-S striking sub-horizontal fractures susceptible to slip on stimulation in the over-thrust stress regime at Habanero reservoir depth (McMahon and Baisch, 2013; Holl and Barton, 2015; McMahon and Baisch, 2015; Llanos et al., 2015). Furthermore, the N/NNE orientation of the ellipses is perpendicular to the orientation of the maximum

horizontal stress in the area (Reynolds et al., 2005; Holl and Barton, 2015).

5.6   Conclusions

Residual phase tensor analysis of MT measurements during a fluid injection show possible fluid-filled fractures oriented in a N/NNE direction. Apparent resistivity maps also reveal the injected fluids likely propagated towards N/NNE direction. Furthermore, analysis of the time-lapse models show an increase in cumulative conductance in the N-S direction compared to the E-W direction for MT site close to Habanero-4 well. This is consistent with the propagation direction of seismic events observed during fluid injection and the orientation of pre-existing N-S striking horizontal fractures susceptible to slip in the over-thrust stress regime at the Habanero reservoir depth (McMahon and Baisch, 2013; Bendall et al., 2014; Baisch et al., 2015; Holl and Barton, 2015; McMahon and Baisch, 2015). The observed decrease in resistivity at Habanero is small in magnitude compared to the 10% average decrease in resistivity at Paralana during hydraulic stimulation (Peacock et al., 2013). The main reasons for observing small changes in resistivity at Habanero EGS are the screening effect of the conductive sedimentary basin in the area (about 3.6 km thick) and the presence of pre-existing saline fluids with resistivity of $0.1\,\Omega\,$m in the natural fractures in the EGS reservoirs (Yanagisawa et al., 2011; Hogarth et al., 2013; Meixner et al., 2014; Holl and Barton, 2015). This is further compounded by the physics of the problem, that is, the small volume of injected fluid compared to the large volume averaging by an MT sounding at the depth of interest. Furthermore, the stimulated reservoir at Habanero is a granitic basement while the targeted reservoir at Paralana is a neo-Proterozoic meta-sedimentary formation (Peacock et al., 2013; Meixner et al., 2014). The time-lapse continuous monitoring MT study at Habanero highlights the need for favorable geological settings to achieve significant decreases in resistivity in EGS reservoirs. Despite these limitations, the MT method shows promise as a complementary method to micro-seismics in fluid monitoring for unconventional resource exploration because of its sensitivity to conductivity contrasts caused by fluids (Wohlenberg and Keppler, 1987;

Baria et al., 2004; Cuenot et al., 2008; Hasting et al., 2011; Peacock et al., 2012, 2013; Cladouhos et al., 2013; Albaric et al., 2014; Börner et al., 2015).

Acknowledgments

CHAPTER

SIX

SUMMARY

There were two main aims of this PhD research program. The first was in characterizing the geothermal reservoirs of the Tendaho high temperature conventional geothermal system in north east Ethiopia. This included delineating possible fluid pathways (upflow zone), estimating the amount of melt fraction in the crust and determining the connectivity of the Dubi and Ayerobera geothermal localities in the Tendaho geothermal field using 2D and 3D resistivity models, geochemical data and borehole information.

The second aim was to determine the potential for MT to monitor permeability enhancement in unconventional EGS reservoirs in terms of spatial and temporal changes in bulk resistivity during hydraulic stimulation at the Habanero EGS site in the Cooper Basin, South Australia.

In this dissertation, different aspects of MT imaging and monitoring were presented. Chapter 2 comprises an overview of the MT method, including a discussion of the use of phase tensors and melt fraction estimation. In Chapter 3, 2D resistivity modeling was used to characterize the Tendaho conventional hydrothermal geothermal field. A 2D resistivity model, geochemical data and borehole logs were jointly analyzed in order to estimate the melt fraction in the upper crust. These results were published in *Geophysical Research Letters.* Chapter 4 presents 3D

resistivity models of the Tendaho geothermal field to a depth of 20 km obtained from the inversion of 116 MT sites in the period range from 0.003 s to 1000 s. These results were published in the *Journal of Volcanological and Geothermal Research*. Chapter 5 describes time-lapse MT inversion results and residual phase tensor analyses of MT monitoring at Habanero EGS in the Cooper Basin, South Australia. These results have been submitted to the *Journal of Geophysical Research: Solid Earth*.

6.1   MT imaging at Tendaho

The MT imaging of the Tendaho high temperature geothermal system resolves the deep geothermal reservoir under sedimentary cover that has not been imaged with previous DC resistivity surveys. A typical high temperature geothermal system is characterized by a conductive clay cap underlain by a moderately resistive reservoir. The Tendaho geothermal system also shows a similar resistivity structure to other high enthalpy geothermal systems where thick sedimentary cover acts both as cap rock and a shallow reservoir. The deep geothermal reservoir in the basalts is characterized by low permeability due to deposition of hydrothermal alteration products (Aquater, 1996a; Battistelli et al., 2002). The interpreted upflow zone in the basalts is likely an ideal target for future drilling due to its high permeability and high temperature. Lateral boundaries of the fracture zone are not resolved by the current MT data set. The integrated interpretation of the resistivity models and the geochemistry of the geothermal fluids suggest that the Dubi and Ayerobera sub-geothermal systems at Tendaho are not connected. This indicates the need for differing development plans for the two sub-geothermal systems. Three dimensional resistivity model will help in updating the existing conceptual model of the Tendaho geothermal field and siting future drilling wells.

6.2   MT monitoring at Habanero EGS

Models of a baseline MT survey reveal the main resistivity structures to a depth of 5 km. High resistivity granitic EGS reservoir is overlain

by a low resistivity thick sedimentary cover (3.6 km thick). Pre- and post-injection MT monitoring responses showed, on average a 5% decrease in xy component resistivity and a 1.5% decrease in yx component resistivity resulting from hydraulic stimulation for periods greater than 10 s. Residual phase tensor analyses reveal N/NNE oriented change in impedance tensor, most likely from conductive fluid-filled fractures that have been stimulated. The apparent resistivity versus period maps also uncovered the injected fluids plume likely propagated towards N/NNE direction. Furthermore, the time-lapse MT inversion models also indicate an increase in total conductance in the N-S direction compared to the E-W direction for a depth range of 2-5 km. This indicates an anisotropic nature of permeability generated by the fluid injection. This result is consistent with the propagation direction of the dominant microseismic events, as well as the orientation of pre-existing N-S striking sub-horizontal fractures susceptible to slip on stimulation. In general, the continuous MT monitoring at Habanero showed a small decrease in the magnitude of resistivity as result of stimulation. The continuous monitoring MT study at Habanero underscored the need for a favorable geological setting and/or controlled source methods and down-hole methods in order to measure significant changes in resistivity in EGS reservoirs.

6.3 Concluding remarks

In this research project, MT is used to characterize both conventional and unconventional geothermal systems. Permeability is one of the key factors determining the productivity and sustainability of geothermal resources. Faults and fractures are important fluid pathways in geothermal systems, which provide permeability to the reservoirs.

The MT method is commonly used to characterize conventional geothermal systems. It is sensitive to the conductivity contrasts generated by saline fluids in faults and fractures, clay alteration products, partial melts and high temperatures. The 2D and 3D resistivity models of the Tendaho geothermal field provide new constraints on permeability of the basaltic deep geothermal system. The permeable upflow zone delineated

by the MT imaging is an ideal target for future drilling at the Tendaho geothermal field. Systematically gridded additional MT sites will help in resolving the lateral boundaries of the Tendaho geothermal field.

The time-lapse MT monitoring at Habanero also provided information on the nature of the permeability in the EGS reservoirs. This research study showed that it was difficult to measure significant changes in resistivity resulting from injection with MT because of a combination of many factors. These include the decrease in resolution of MT measurements with depth, the screening effect of thick sedimentary cover and low data quality at the MT dead-band. Despite these limitations, MT shows promise as a complementary method to micro-seismics in fluid monitoring for unconventional resources (for example, coal-seam and shale gas) exploration. The coverage of continuous time-lapse MT monitoring survey can be improved by deploying many only electric field stations and using the magnetic field data from the neighboring site with complete channels of electric and magnetic components . Simulation studies with EM methods show that deployment of EM receivers (sensors) downhole at depth significantly improves the measured EM signals (Tietze and Ritter, 2014; Börner et al., 2015). The observed change in resistivity resulting from fluid injection at depth of 4 km was not recovered using smooth inversion routines. The availability of inversion codes geared to model changes in resistivity during time-lapse MT monitoring remains vital.

Appendices

SUPPORTING INFORMATION FOR CHAPTER 3

A.1   2D MT data and responses

This appendix contains 2D Occam inversion results from Tendaho geothermal field. Figure A.1 shows the location of the MT stations used for 2D inversion. Rose diagram of geoelectric strike angle for the whole data set on the profile is shown in Figure A.2. The fits of the data and model response of the TE and TM modes of the profile arranged from SW to NE are given in Figures A.3, A.4, and A.5. The blue squares and the red dots are observed TE and TM data, respectively. The green and magenta curves show the responses of the TE and TM modes, respectively. The TM mode inversion model is displayed in Figure A.6. The corresponding fits of the data and model of the profile arranged from SW to NE are shown in Figures A.7, A.8, and A.9. The red dots and magenta curves show the observed and response of the TM mode data, respectively. The station name is given on top of the plots. The total magnetic field map of Tendaho geothermal field is shown in Figure A.10. Table A.1 illustrates the dependence of melt fraction on composition, temperature, water content and pressure. A model mesh which contains 279 horizontal and 106 vertical nodes used for the 2D Occam inversion of the MT data is shown in Figure A.11.
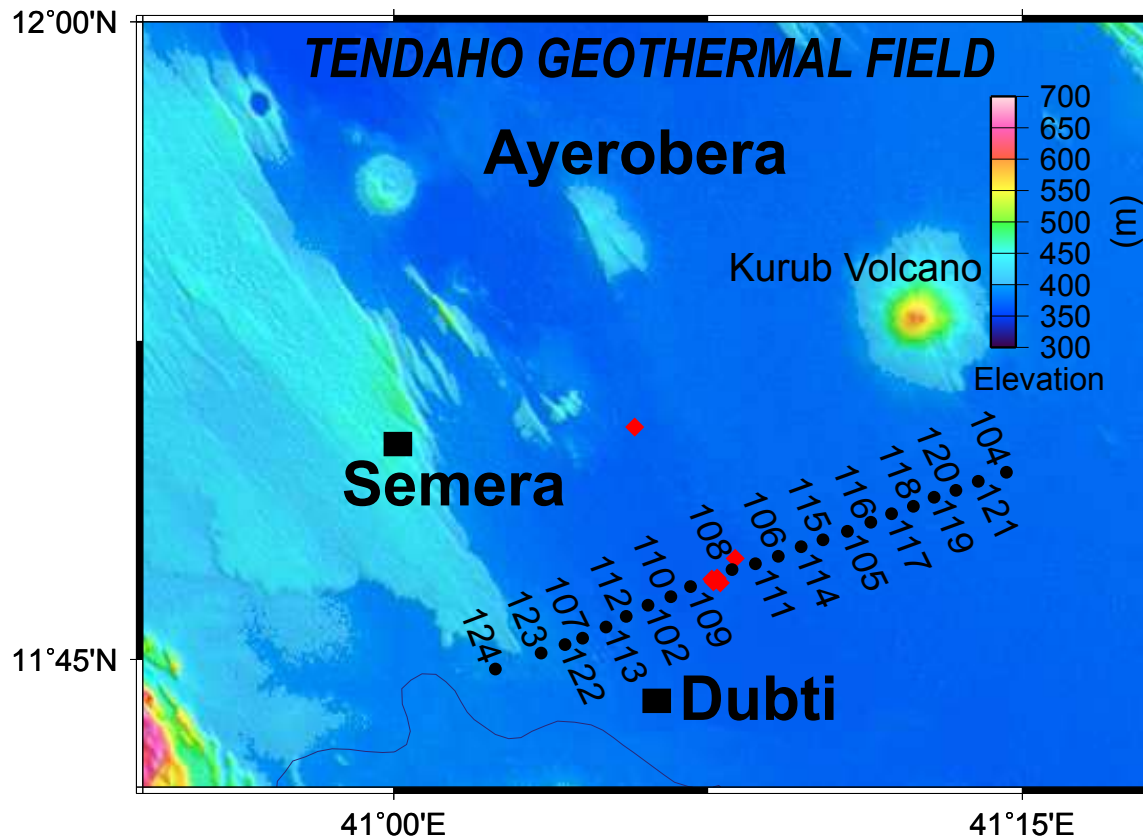
Figure A.1: Location map of MT sites used for 2D inversion from the Tendaho high temperature geothermal field. Black dots denote MT stations along a profile with station spacing of about 1 km. The red diamonds denote exploratory geothermal wells.
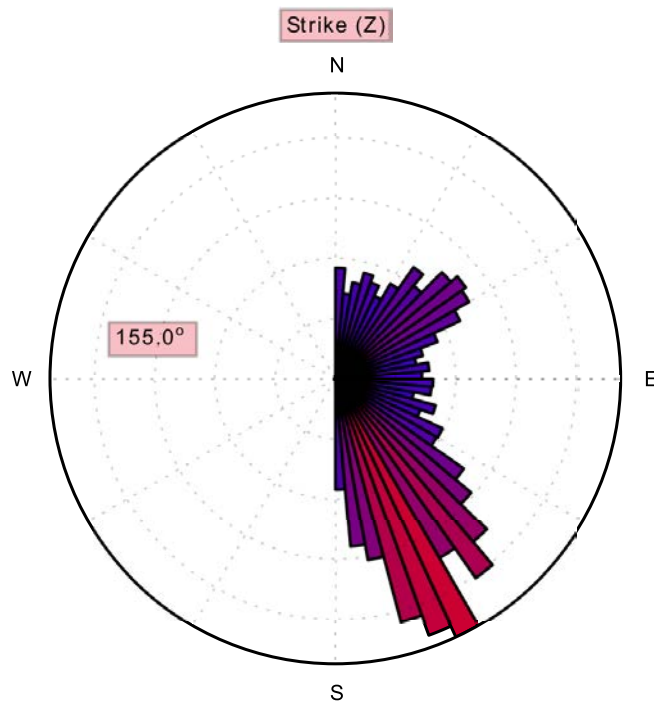
Figure A.2: Rose diagram of geoelectric strike angle determined using azimuth of main axis of phase tensors (Caldwell et al., 2004) for all sites and the whole period range (0.003 s to 1000 s) (with a 90° ambiguity). It indicates a strike direction of N155 °E which is consistent with regional geologic strike of Tendaho graben.
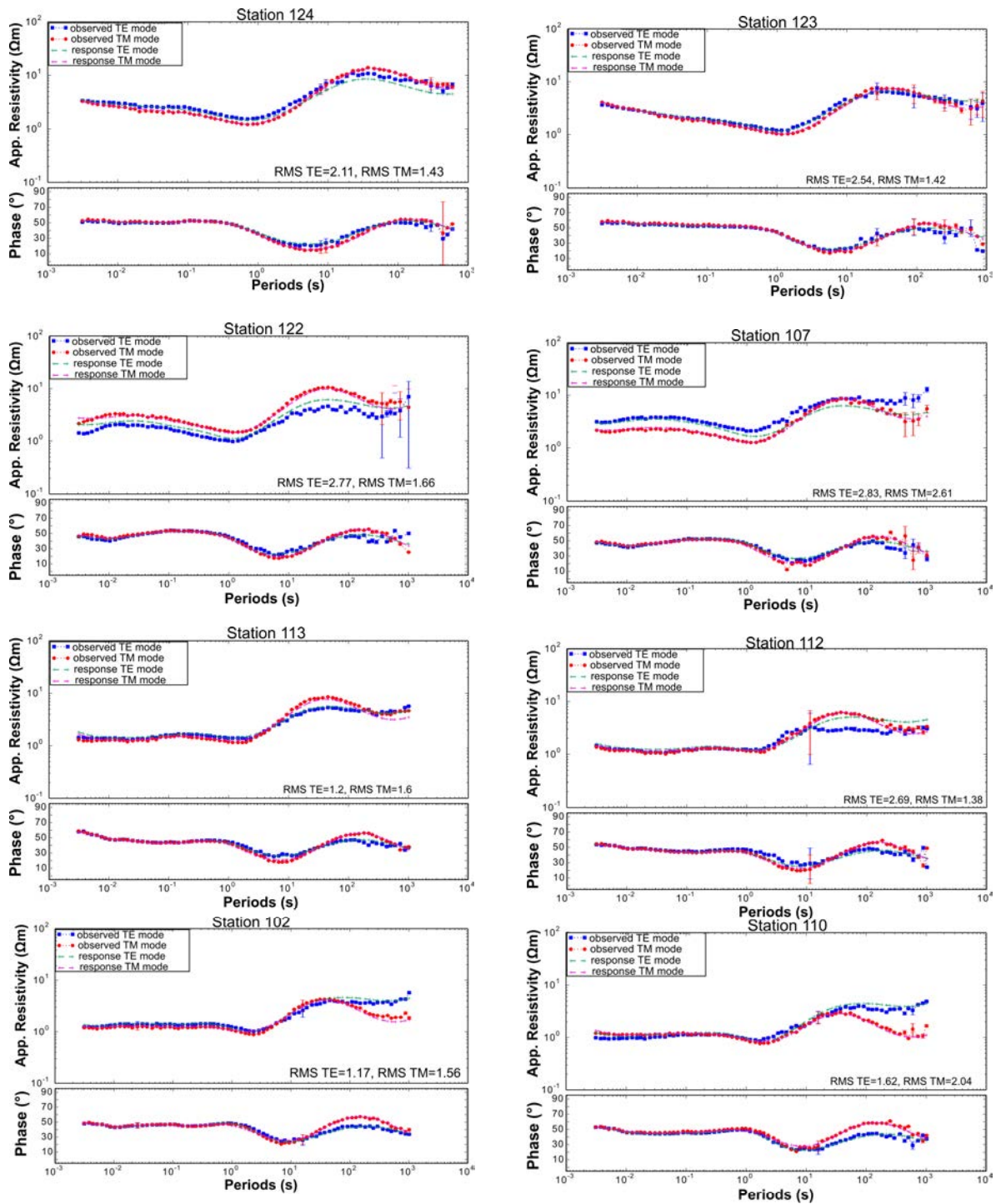
Figure A.3: Fit of data and model response from the joint 2D inversion of TE and TM modes of apparent resistivity ρ in (Ω m) and phase Φ in (°) of MT sites along the Profile. The green and magenta curves show the response of the TE and TM modes data. The blue square and the red dots are observed TE and TM data.
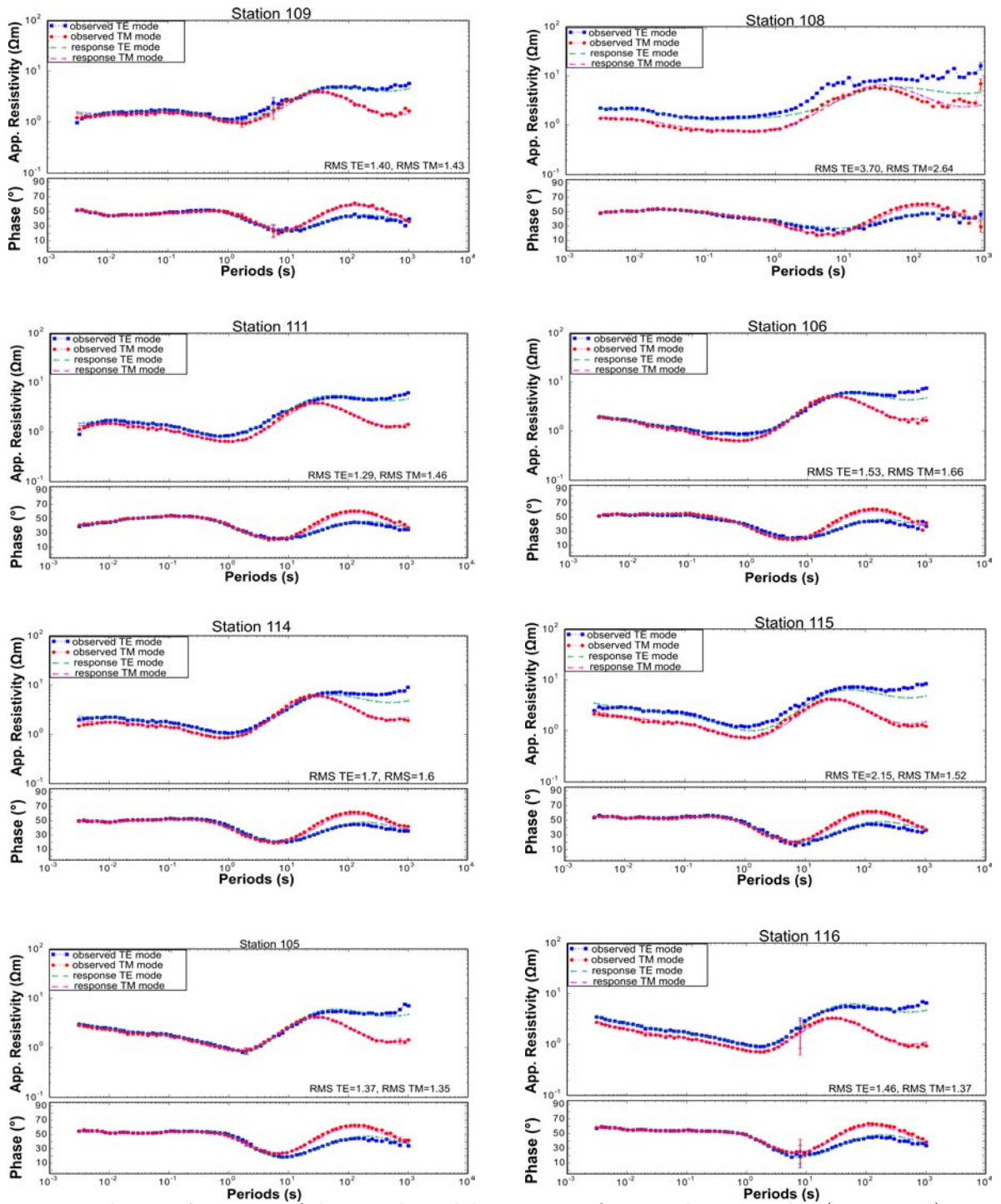
Figure A.4: Fit of data and model response of TE and TM modes (continued).
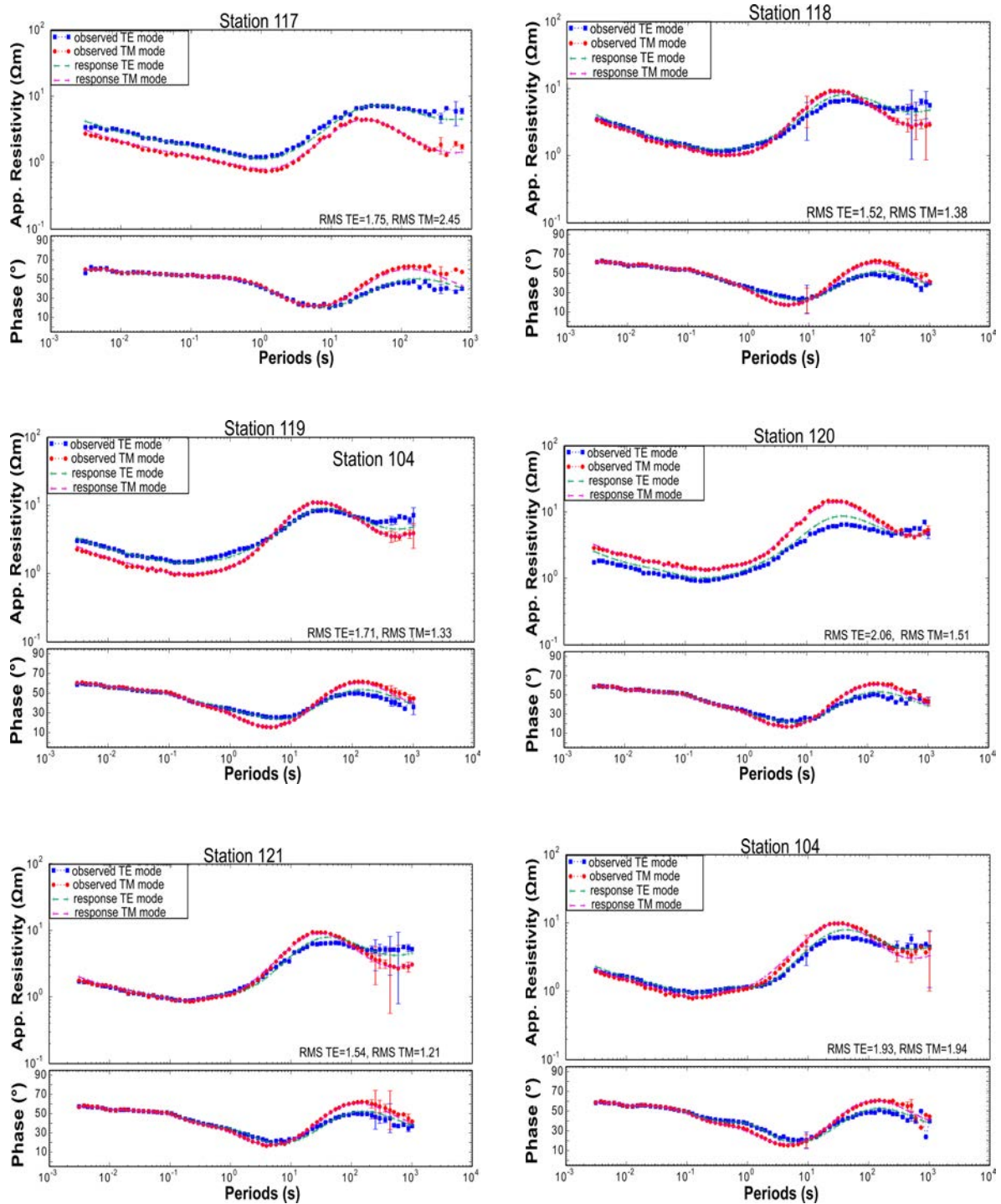
Figure A.5: Fit of data and model response of TE and TM modes (continued).
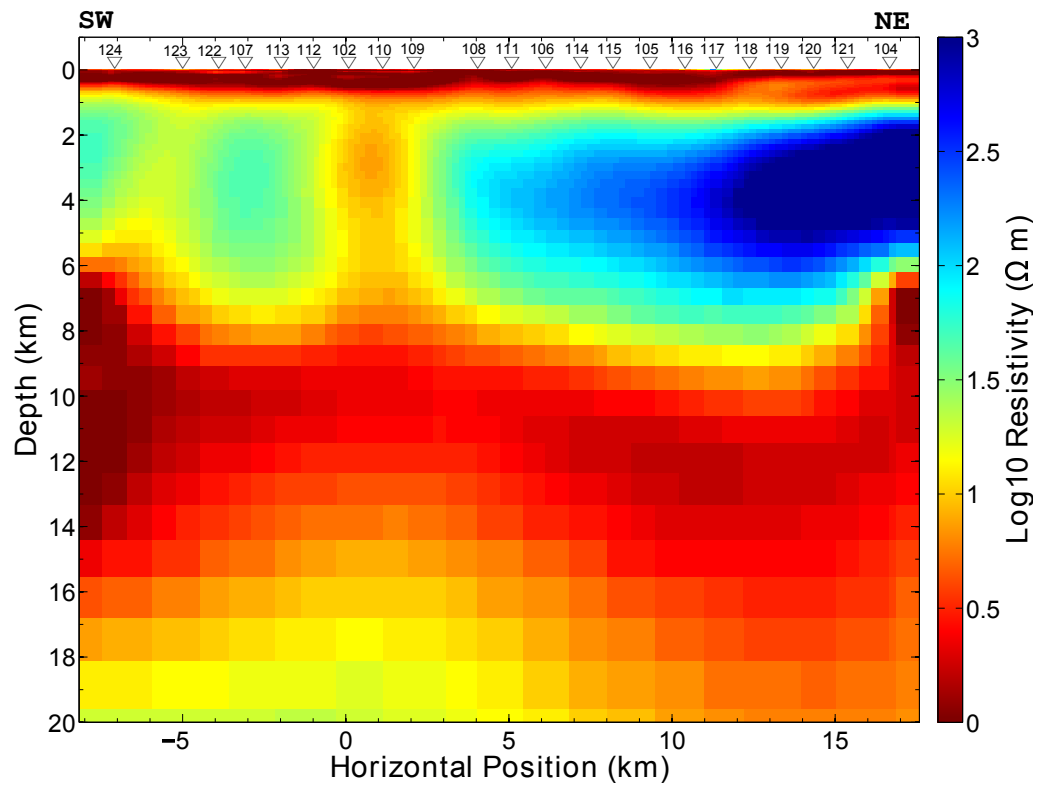
Figure A.6: Preferred 2D resistivity model obtained by inversion of TM mode data for the MT profile with a RMS misfit of 1.7. Hot (red) color is low resistivity. Blue color is high resistivity. Inverted triangles on top of the model are MT station locations.
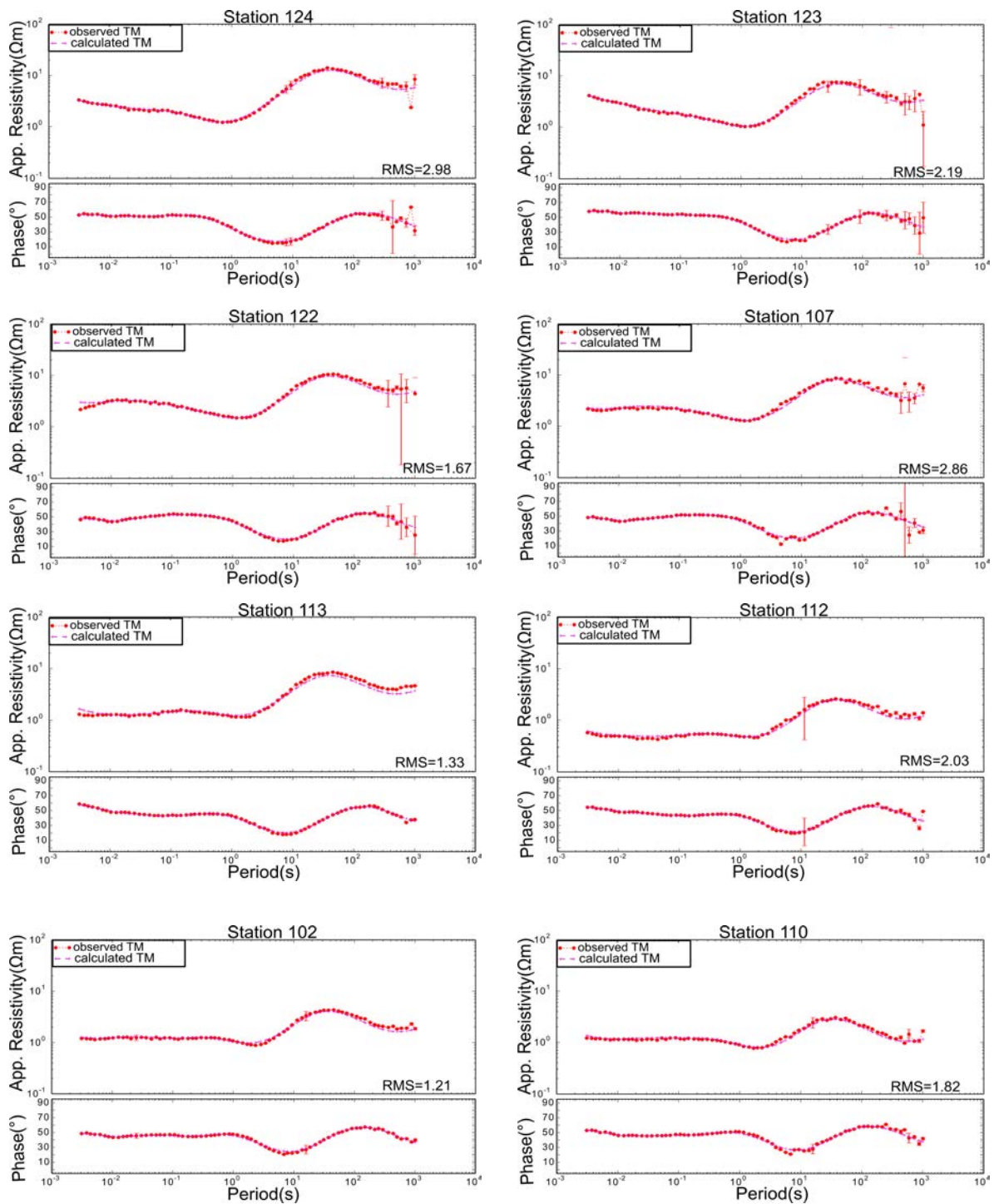
Figure A.7: Fit of data and model response from the 2D inversion of TM mode of apparent resistivity ρ in (Ω m) and phase Φ in (°) of MT sites from SW to NE along the profile. The red dots and magenta curves show the observed and response of the TM mode data, respectively.
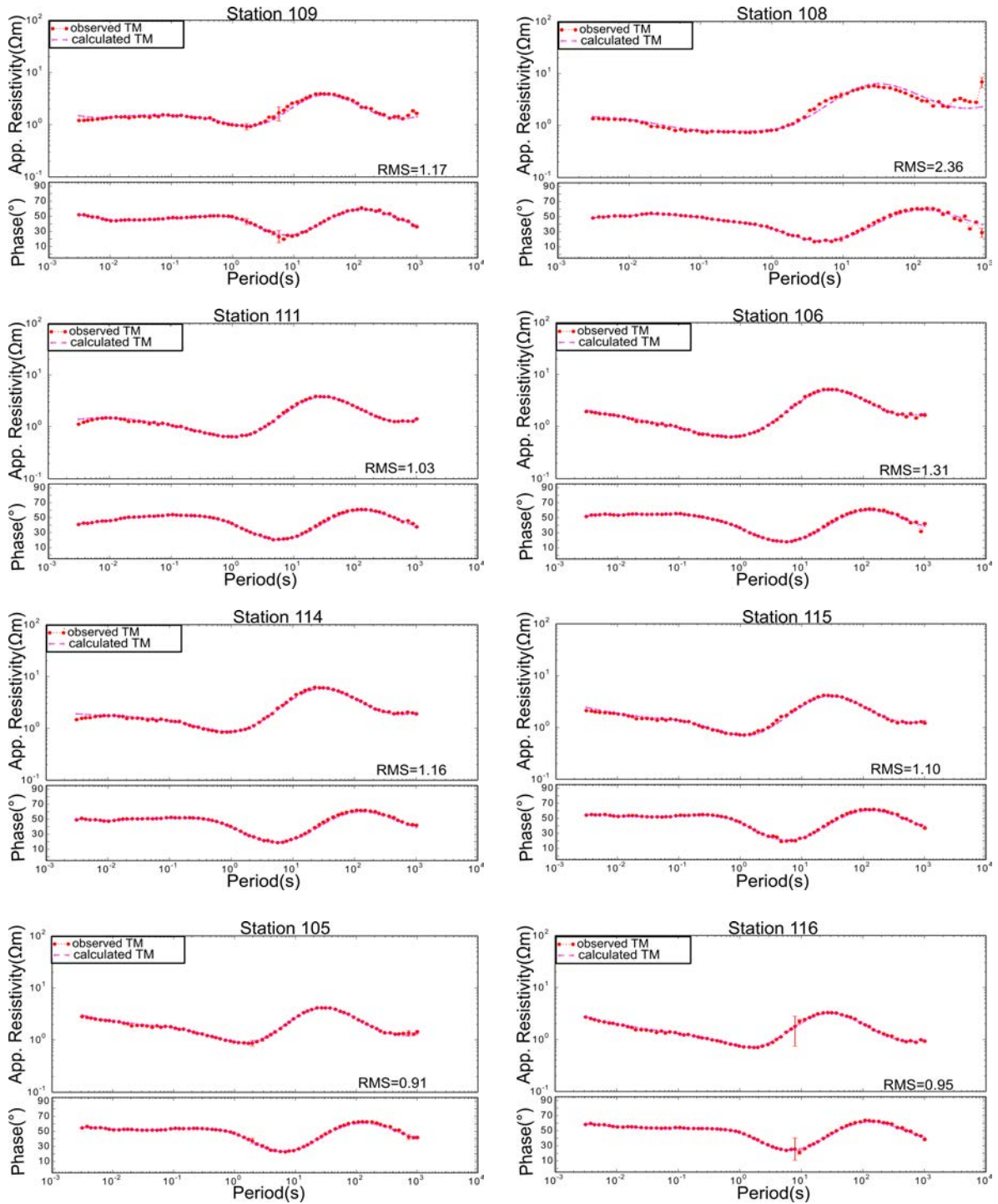
Figure A.8: Fit of data and model response of TM mode data (Continued).
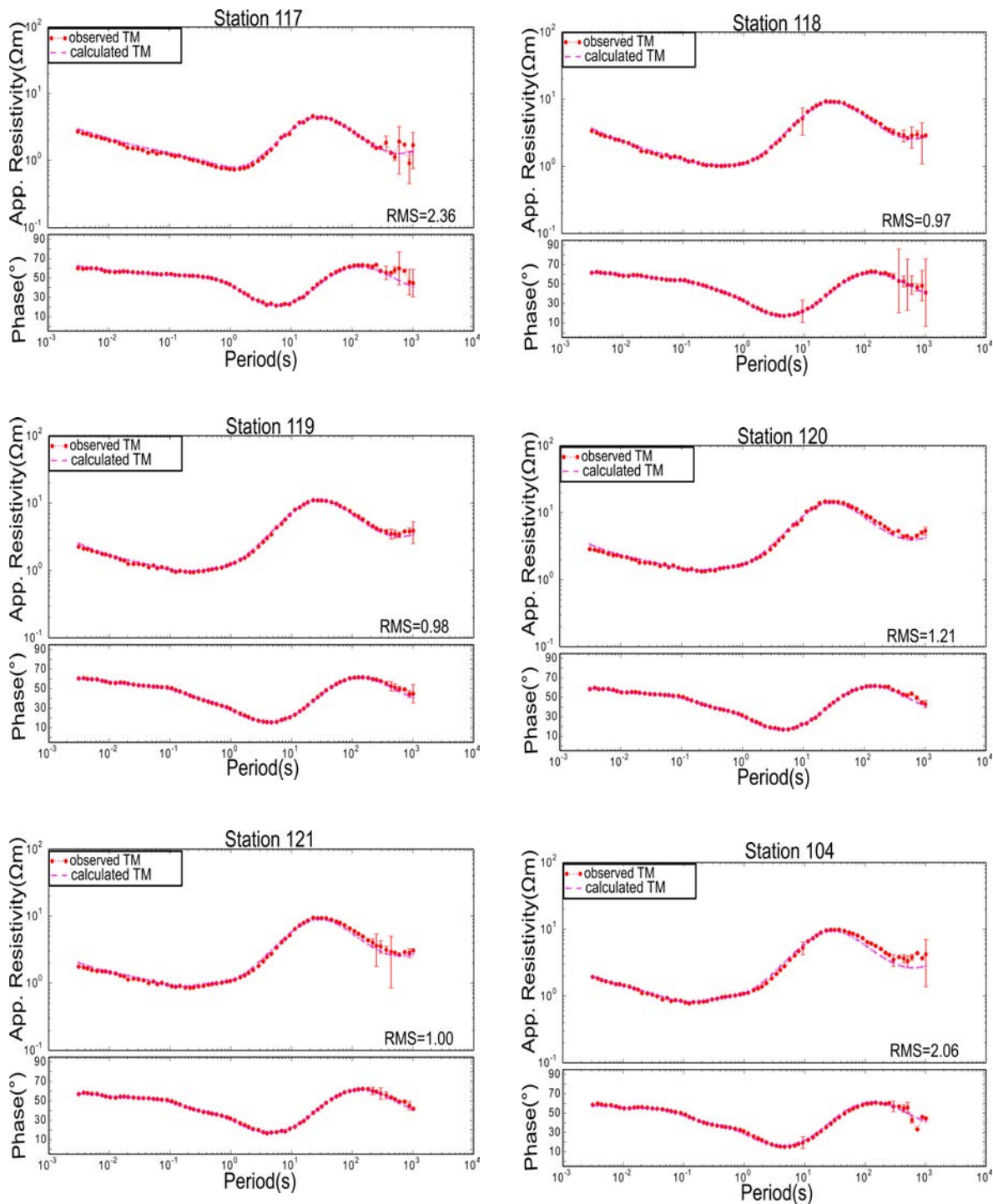
Figure A.9: Fit of data and model response of TM mode data (Continued).
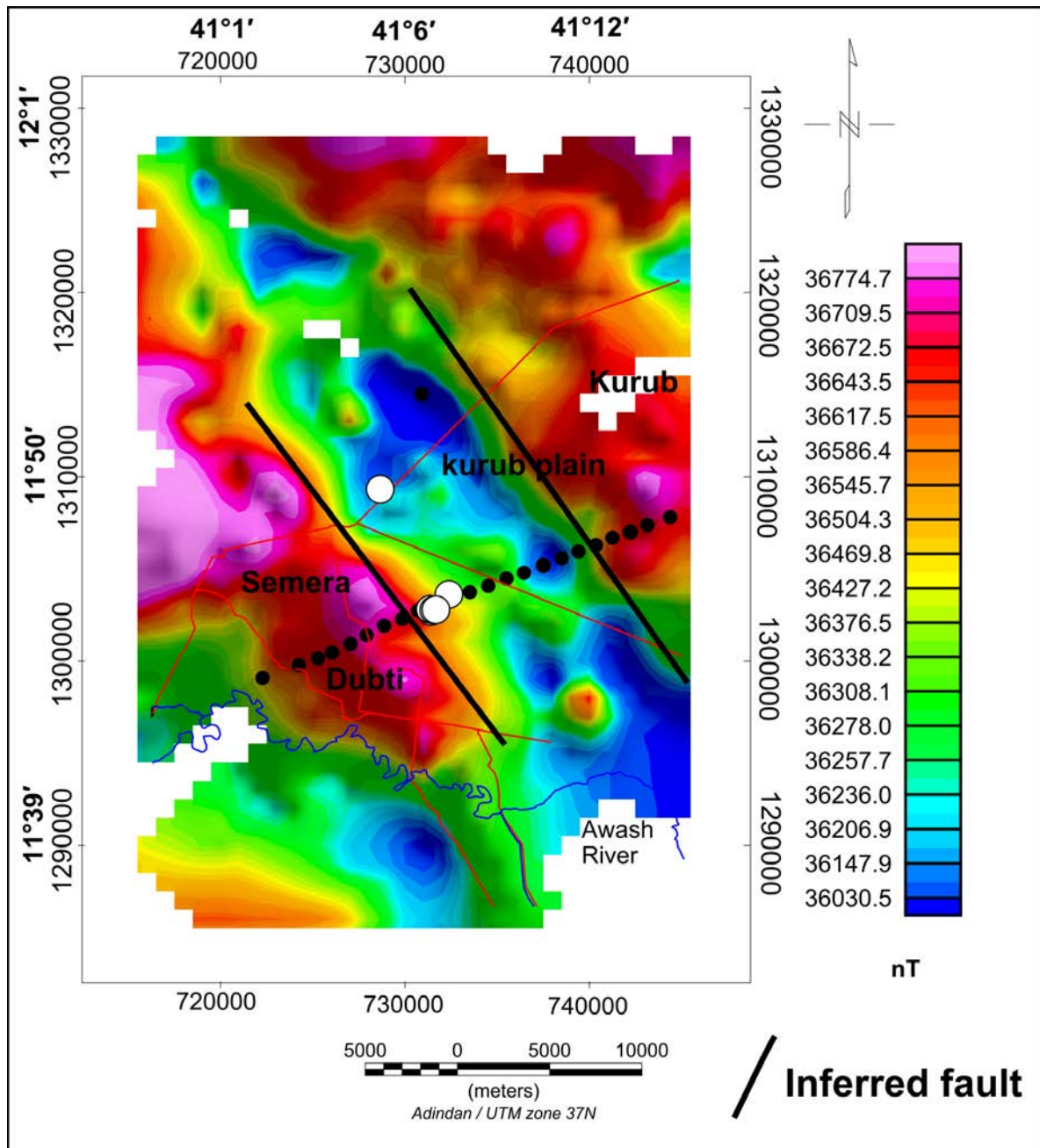
Figure A.10: Total magnetic field map of Tendaho geothermal field showing possible inferred faults which coincide with updoming low resistivity structure observed at depth 2 km in the 2D MT model under sites102, 110 and 109. White circles= Geothermal well, black dots=MT sites.

Table A.1: Melt fraction dependence on composition, temperature, water content and pressure for Tendaho rock samples calculated using SIGMELTS [Pommier Le-Tong, 2011].

Composition						
SiO$_2$		Na$_2$O	Temperature (℃)	Pressure (MPa)	Weight % H$_2$O	σ_m (Sm^{-1})
49.42		3.15	1210	250	0	0.917
46.46		2.64	1210	250	0	2.391
47.8 (average)		2.5	1210	250	0	1.584
Temperature						
SiO$_2$	Na$_2$O		Temperature (℃)	Pressure (MPa)	Weight % H$_2$O	σ_m (Sm^{-1})
47.8	2.5		975	250	0	0.207
47.8	2.5		1210	250	0	1.584
Weight % water						
SiO$_2$	Na$_2$O		Temperature (℃)	Pressure (MPa)	Weight % H$_2$O	σ_m (Sm^{-1})
47.8	2.5		1210	250	0	1.584
47.8	2.5		1210	250	1	3.126
47.8	2.5		1210	250	2	3.418
47.8	2.5		1210	250	3	4.191
47.8	2.5		1210	250	4	5.879
47.8	2.5		1210	250	5	9.497
47.8	2.5		1210	250	6	17.714
Pressure						
SiO$_2$	Na$_2$O		Temperature (℃)	Pressure (MPa)	Weight % H$_2$O	σ_m (Sm^{-1})
47.8	2.5		1210	200	0	1.573
47.8	2.5		1210	300	0	1.595

MESH FILE FROM MAKE2DMODEL							
0	279	106	0	0	2		
207524.2	69174.7	23058.2	7686.1	2562	854	284.7	94.9
94.9	94.9	94.9	94.9	94.9	94.9	94.9	94.9
94.9	94.9	94.9	94.9	94.9	94.9	94.9	94.9
94.9	94.9	94.9	94.9	94.9	94.9	94.9	94.9
91.7	91.7	91.7	91.7	91.7	91.7	91.7	91.7
91.7	91.7	91.7	91.7	81.5	81.5	81.5	81.5
81.5	81.5	81.5	81.5	81.5	81.5	92.5	92.5
92.5	92.5	92.5	92.5	92.5	92.5	92.5	92.5
92.5	92.5	98.6	98.6	98.6	98.6	98.6	98.6
98.6	98.6	98.6	98.6	89.3	89.3	89.3	89.3
89.3	89.3	89.3	89.3	89.3	89.3	89.3	89.3
87.2	87.2	87.2	87.2	87.2	87.2	87.2	87.2
87.2	87.2	87.2	87.2	95.8	95.8	95.8	95.8
95.8	95.8	95.8	95.8	95.8	95.8	97.5	97.5
97.5	97.5	97.5	97.5	97.5	97.5	97.5	97.5
97.5	97.5	97.5	97.5	97.5	97.5	97.5	97.5
97.5	97.5	86.8	86.8	86.8	86.8	86.8	86.8
86.8	86.8	86.8	86.8	86.8	86.8	87.4	87.4
87.4	87.4	87.4	87.4	87.4	87.4	87.4	87.4
87.4	87.4	88.9	88.9	88.9	88.9	88.9	88.9
88.9	88.9	88.9	88.9	88.9	88.9	99.3	99.3
99.3	99.3	99.3	99.3	99.3	99.3	99.3	99.3
94.1	94.1	94.1	94.1	94.1	94.1	94.1	94.1
94.1	94.1	94.1	94.1	89.3	89.3	89.3	89.3
89.3	89.3	89.3	89.3	89.3	89.3	89.3	89.3
96.9	96.9	96.9	96.9	96.9	96.9	96.9	96.9
96.9	96.9	84.2	84.2	84.2	84.2	84.2	84.2
84.2	84.2	84.2	84.2	84.2	84.2	98.1	98.1
98.1	98.1	98.1	98.1	98.1	98.1	98.1	98.1
99.5	99.5	99.5	99.5	99.5	99.5	99.5	99.5
99.5	99.5	86.0	86.0	86.0	86.0	86.0	86.0
86.0	86.0	86.0	86.0	86.0	86.0	92.3	92.3
92.3	92.3	92.3	92.3	92.3	92.3	92.3	92.3
92.3	92.3	92.3	92.3	92.3	92.3	92.3	276.9
830.8	2492.4	7477.2	22431.7	67295.1	201885.3		
3.0	3.0	3.0	3.0	6.0	6.0	6.0	6.0
6.0	6.0	6.0	6.0	6.0	6.0	6.0	6.2
6.7	7.3	7.8	8.5	9.1	9.9	10.6	11.5
12.4	13.4	14.5	15.6	16.9	18.2	19.7	21.2
22.9	24.8	26.7	28.9	31.2	33.7	36.4	39.3
42.4	45.8	49.4	53.4	57.6	62.2	67.2	72.5
78.3	84.6	91.3	98.6	106.5	115	124.2	134.1
144.8	156.3	168.8	182.2	196.8	212.5	229.4	247.7
267.5	288.8	311.9	336.7	363.6	392.6	423.9	457.8
494.3	533.7	576.3	622.2	671.9	725.5	783.4	845.9
913.3	986.2	1064.9	1149.8	1241.5	1340.6	1447.5	1563
1687.7	1822.3	1967.7	2124.7	2294.2	2477.2	2674.8	2888.2
3118.6	3367.4	3636.1	3926.1	4239.3	12718	38154	114462
343385.9							

(Left margin label for the upper block: Horizontal nodes (m); for the lower block: Vertical nodes (m))

Figure A.11: The 2D Occam model mesh for the profile. The second row indicates 279 nodes in the horizontal direction and 106 nodes in the vertical direction. The subsequent rows show the dimensions of the horizontal and vertical nodes in meters.

APPENDIX

B

SUPPORTING INFORMATION FOR CHAPTER 4

B.1   3D responses and magnetics map

This appendix comprises 3D inversion results, magnetics map and MT station location of Tendaho geothermal field. Figure B.1 shows the locations of the seven profiles used in the 3D inversions. The fits of selected apparent resistivity and phase curves for the 3D inversion are displayed in Figure B.2. The observed, calculated and misfit phase tensor ellipses for the 3D inversion are also shown in Figures B.3, B.4, B.5, B.6, and B.7. The magnetic map of Tendaho, which depicts inferred faults, is given in Figure B.8. Tables B.1 and B.2 contain the locations of the 116 MT stations used in the 3D inversions.
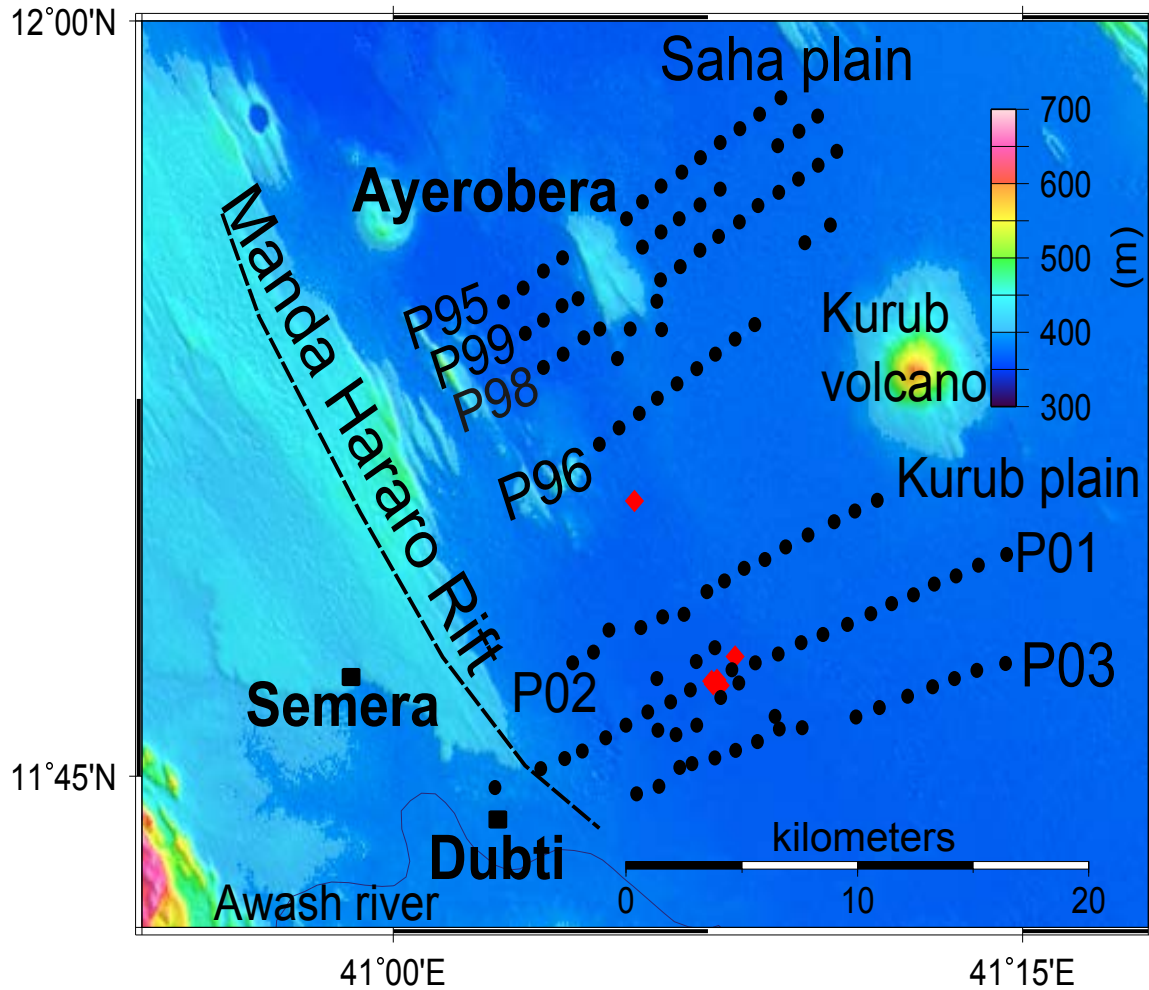
Figure B.1: Location map of MT sites used for 3D inversion from the Tendaho geothermal field. The southern profiles P01, P02, P03 are located in the Dubti sub-geothermal area and the northern profiles P96, P98, P99 and P95 are located in the Ayerobera sub-geothermal area. The red diamonds indicate geothermal wells.
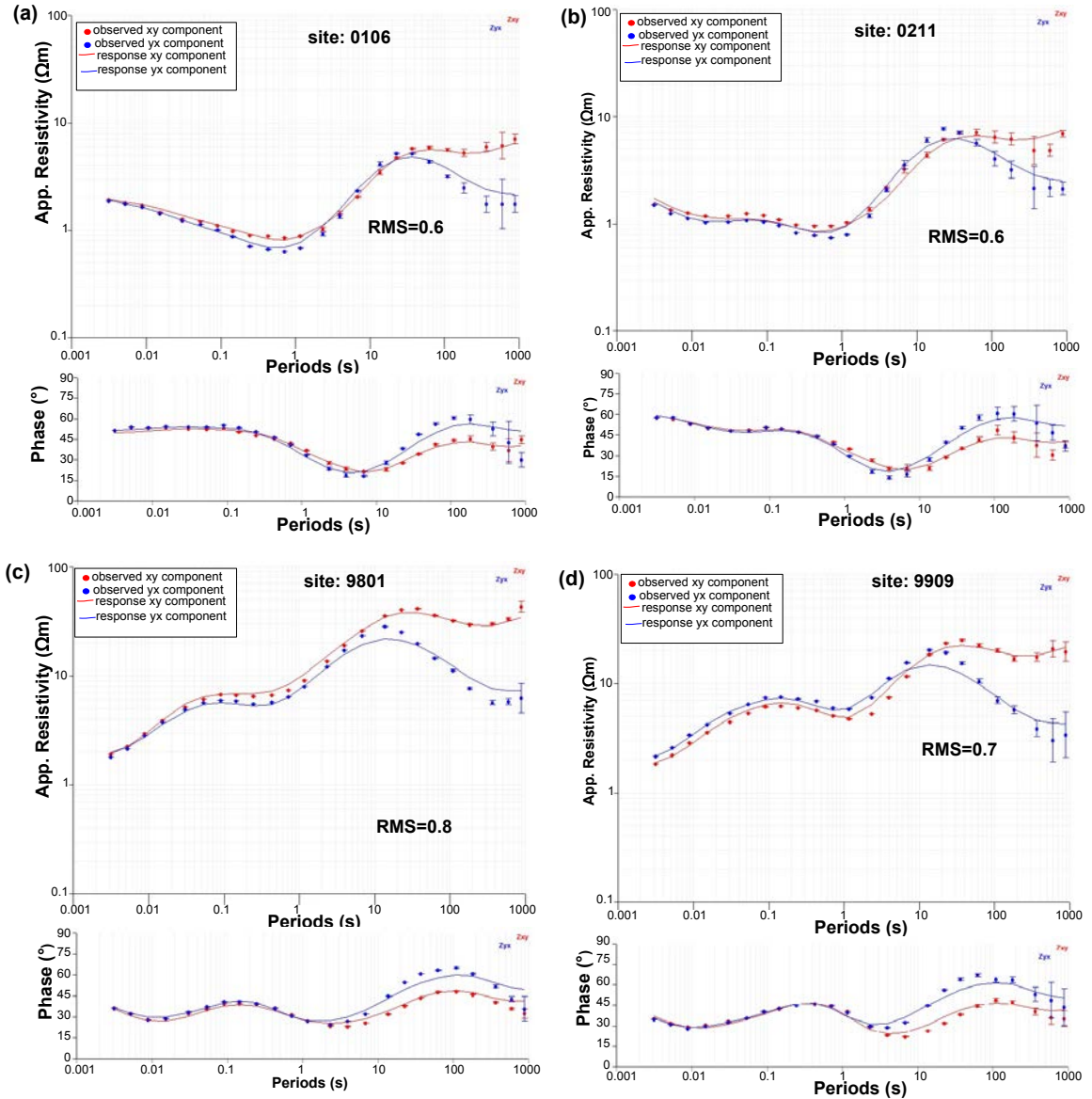
Figure B.2: Fits of selected apparent resistivity and phase curves from the 3D inversion (a)-(b) from southern profiles and (c)-(d) from northern profiles. The red dot and curves show the observed and response of xy component of resistivity and phases, respectively. The blue dots and curves show the observed and response of yx component of resistivity and phases, respectively.
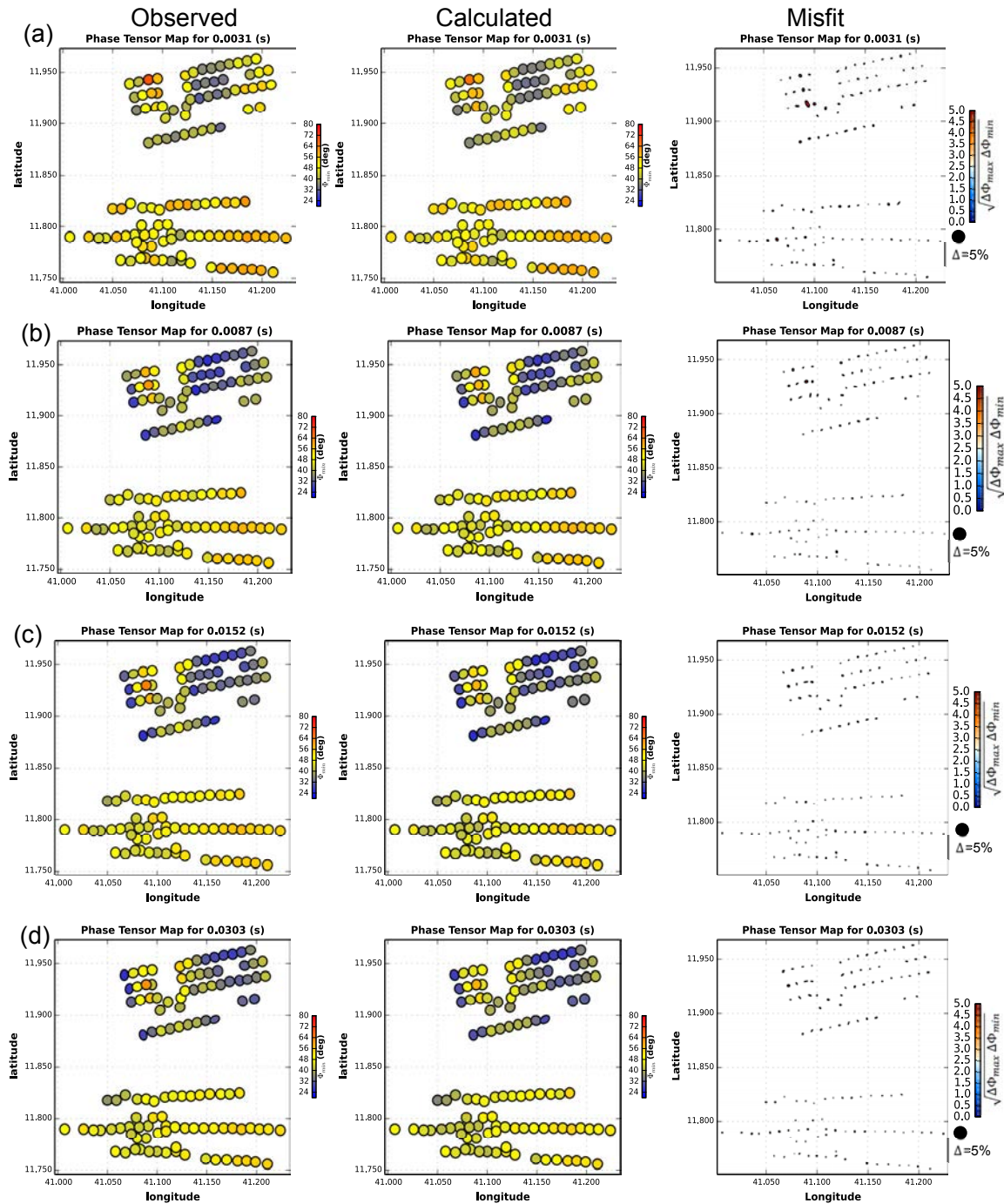
Figure B.3: Each row (a)-(d) shows phase tensor ellipses of observed data, calculated from 3D inversion and misfit for the observed and calculated inversion model for respective periods of 0.0031 s, 0.0087 s, 0.0152 s and 0.0303 s. The observed and calculated ellipses are colored by the minimum principal phase. The misfit ellipses are colored by percentage of the geometric mean of changes in maximum and minimum phases of observed and calculated phase tensors. The small size of ellipse indicates the misfit is small.
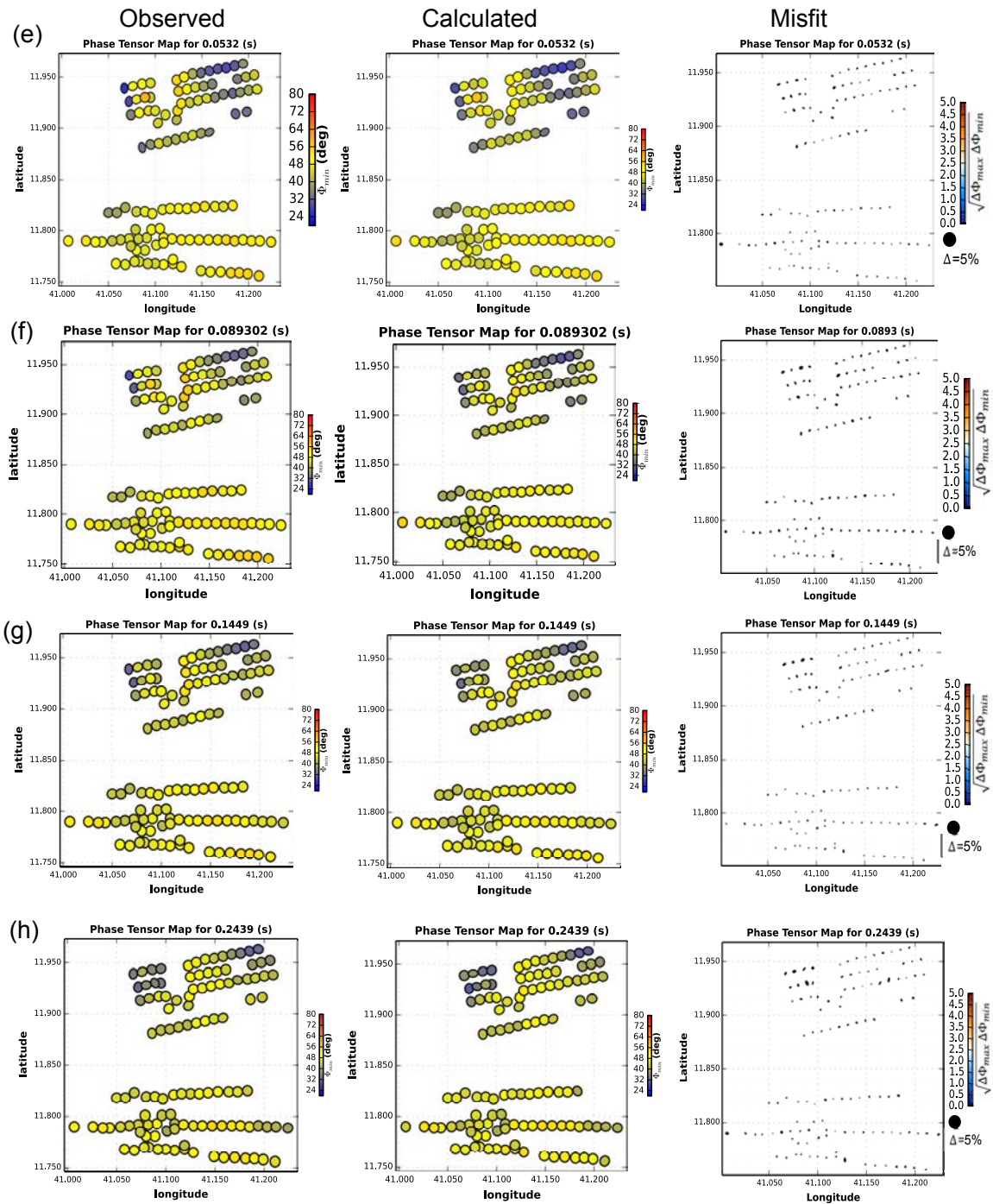
Figure B.4: Each row (e)-(h) shows phase tensor ellipses of observed data, calculated from 3D inversion and misfit for the observed and calculated inversion model for respective periods of 0.0532 s, 0.0893 s, 0.1449 s and 0.2439 s. The observed and calculated ellipses are colored by the minimum principal phase. The misfit ellipses are colored by percentage of the geometric mean of changes in maximum and minimum phases of observed and calculated phase tensors. The small size of ellipse indicates the misfit is small.
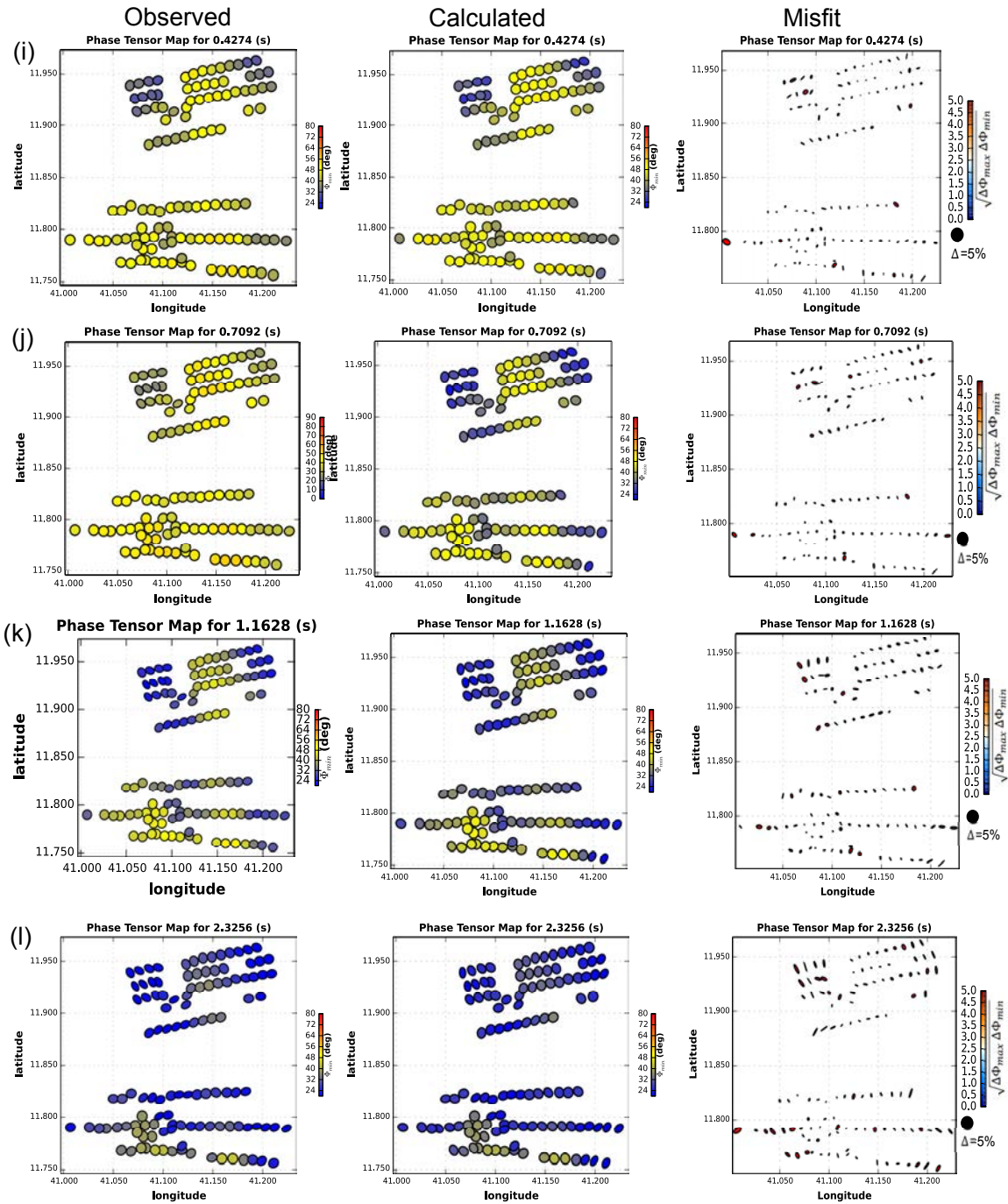
Figure B.5: Each row (i)-(l) shows phase tensor ellipses of observed data, calculated from 3D inversion and misfit for the observed and calculated inversion model for respective periods of 0.4274 s, 0.7092 s, 1.1628 s and 2.3256 s. The observed and calculated ellipses are colored by the minimum principal phase. The misfit ellipses are colored by percentage of the geometric mean of changes in maximum and minimum phases of observed and calculated phase tensors. The small size of ellipse indicates the misfit is small.
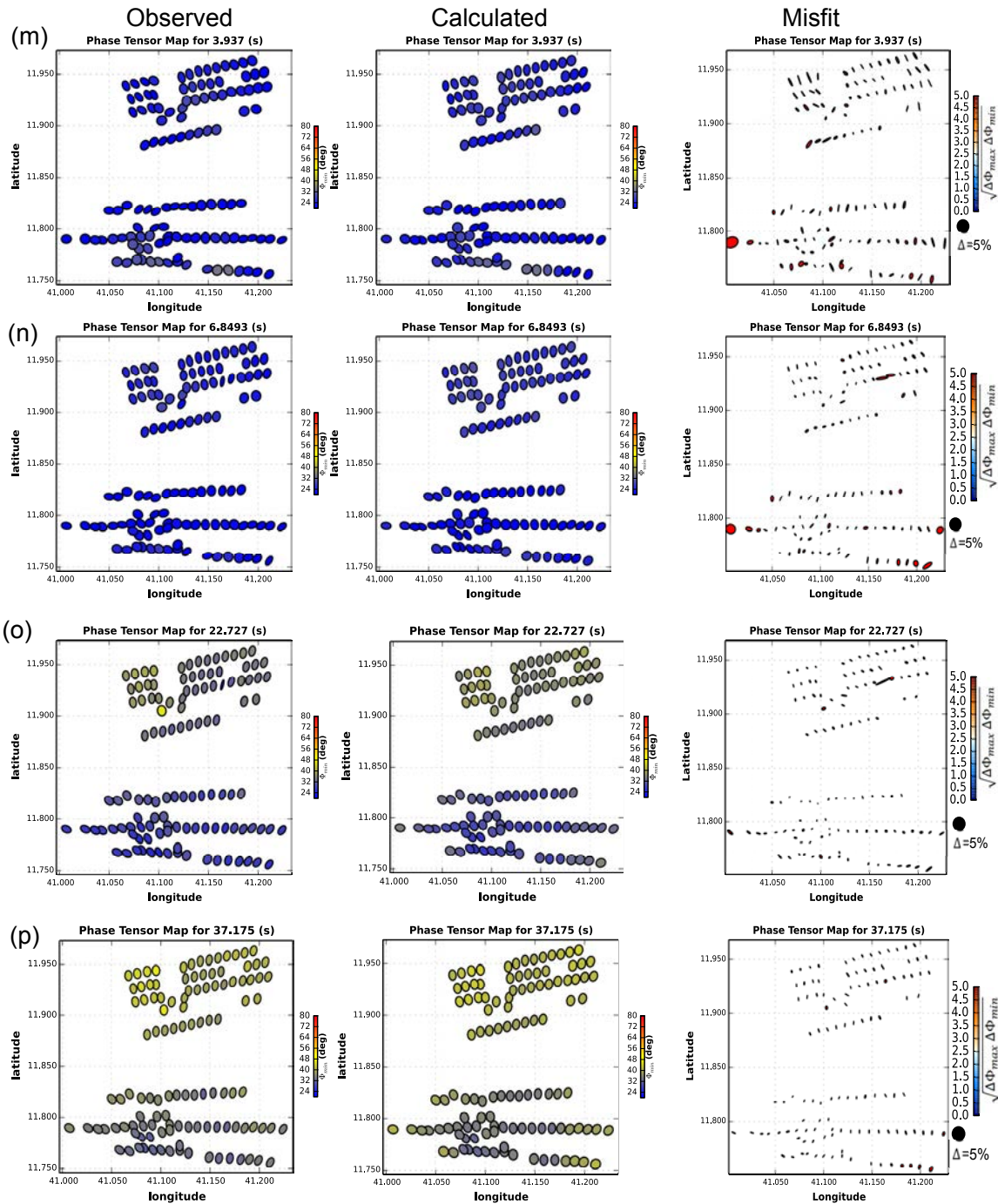
Figure B.6: Each row (m)-(p) shows phase tensor ellipses of observed data, calculated from 3D inversion and misfit for the observed and calculated inversion model for respective periods of 3.937 s, 6.8493 s, 22.727 s and 37.175 s. The observed and calculated ellipses are colored by the minimum principal phase. The misfit ellipses are colored by percentage of the geometric mean of changes in maximum and minimum phases of observed and calculated phase tensors. The small size of ellipse indicates the misfit is small.
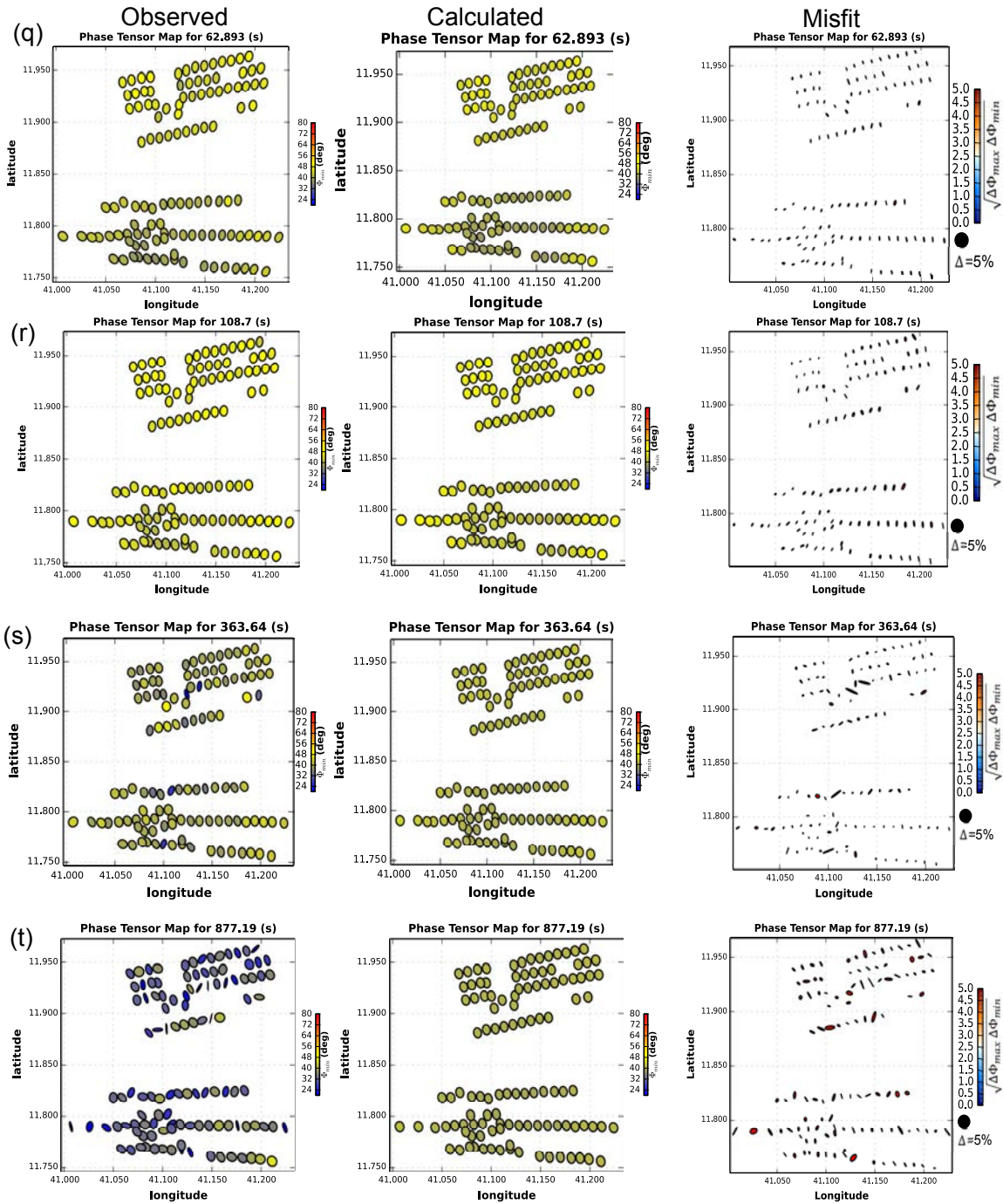
Figure B.7: Each row (q)-(t) shows phase tensor ellipses of observed data, calculated from 3D inversion and misfit for the observed and calculated inversion model for respective periods of 62.893 s, 108.7 s, 363.64 s and 877.19 s. The observed and calculated ellipses are colored by the minimum principal phase. The misfit ellipses are colored by percentage of the geometric mean of changes in maximum and minimum phases of observed and calculated phase tensors. The small size of ellipse indicates the misfit is small.
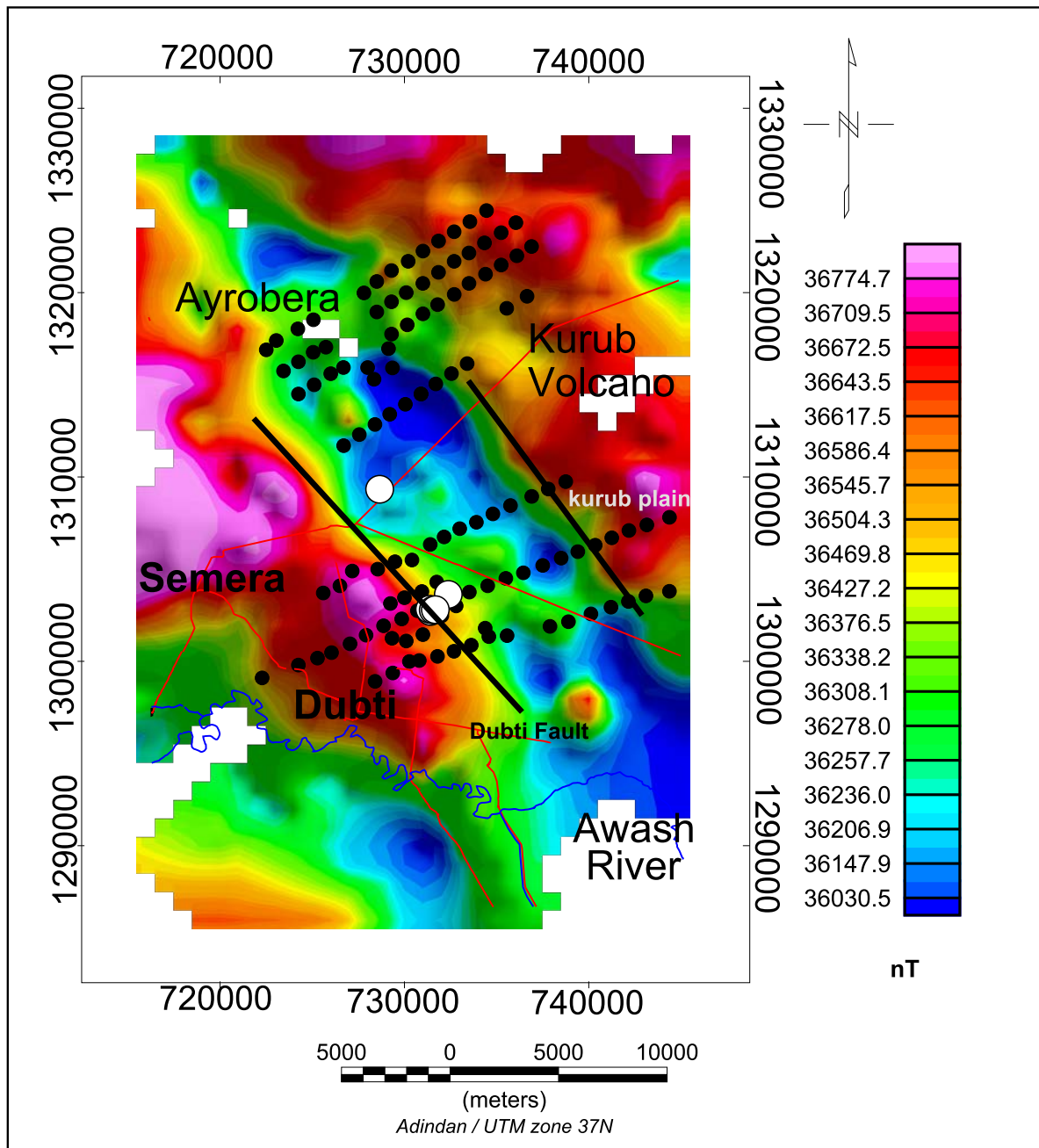
Figure B.8: Total field magnetic map showing inferred faults in the Tendaho geothermal field. Black line=inferred fault, white circle=Geothermal wells, black dots=Mt sites.

Table B.1: MT sites locations at Tendaho High Temperature Geothermal Field.

| MT station	Latitude	Longitude	Northing (UTM)	Easting(UTM)	Elevation (m)
102	11.771	41.101	1301929	728867	364
104	11.824	41.244	1307812	744378	368
105	11.800	41.181	1305203	737503	365
106	11.791	41.153	1304097	734516	365
107	11.759	41.075	1300472	726044	374
108	11.785	41.135	1303497	732501	364
109	11.779	41.118	1302745	730705	366
110	11.775	41.110	1302300	729852	362
111	11.788	41.144	1303756	733521	362
112	11.767	41.092	1301419	727919	370
113	11.763	41.084	1300950	727049	374
114	11.794	41.162	1304500	735500	372
115	11.797	41.171	1304801	736451	367
116	11.804	41.190	1305599	738502	368
117	11.807	41.198	1305950	739403	366
118	11.810	41.207	1306299	740349	365
119	11.814	41.215	1306700	741248	370
120	11.816	41.224	1307000	744220	369
121	11.820	41.233	1307400	743150	372
122	11.756	41.068	1300175	725283	384
123	11.753	41.059	1299798	724246	389
124	11.746	41.040	1299101	722280	391
201	11.788	41.071	1303707	725596	367
202	11.798	41.086	1304898	727169	369
204	11.819	41.139	1307196	732999	378
206	11.791	41.080	1304095	726500	373
207	11.799	41.098	1305000	728550	366
208	11.803	41.107	1305403	729488	364
209	11.804	41.115	1305496	730408	367
210	11.811	41.125	1306340	731400	370
211	11.815	41.132	1306748	732152	379
212	11.822	41.148	1307544	733903	379
213	11.826	41.156	1307998	734799	377
214	11.830	41.165	1308450	735752	376
215	11.834	41.175	1308946	736906	376
216	11.838	41.184	1309350	737800	375
217	11.841	41.192	1309748	738751	377
301	11.787	41.243	1303799	744375	371
304	11.754	41.119	1300044	730805	364
305	11.770	41.184	1301895	737895	368
306	11.762	41.145	1300877	733626	364
307	11.780	41.214	1302938	741205	373
308	11.766	41.153	1301342	734579	366
309	11.766	41.163	1301394	735568	359
311	11.773	41.193	1302150	738897	371
312	11.777	41.204	1302573	740117	372
313	11.759	41.136	1300545	732688	364
314	11.756	41.128	1300269	731793	366
315	11.753	41.114	1299990	730269	368
316	11.747	41.106	1299368	729368	377
317	11.744	41.097	1298913	728408	376
318	11.782	41.223	1303248	742150	371
319	11.785	41.232	1303551	743102	370
501	11.776	41.130	1302472	732029	364
502	11.767	41.121	1301449	731001	364
503	11.764	41.112	1301102	730099	366
504	11.765	41.105	1301251	729327	369
505	11.770	41.152	1301799	734380	359
506	11.781	41.137	1303004	732806	357
508	11.788	41.120	1303788	730947	363
512	11.782	41.105	1303137	729240	370
513	11.793	41.128	1304300	731750	363

Table B.2: MT sites locations at Tendaho geothermal field (continued)

MT station	Latitude	Longitude	Northing (UTM)	Easting(UTM)	Elevation(m)
9501	11.907	41.044	1316897	722504	378
9502	11.912	41.052	1317402	723049	379
9503	11.917	41.060	1318034	724218	379
9504	11.922	41.067	1318528	725062	379
9507	11.935	41.093	1319984	727802	379
9508	11.940	41.099	1320604	728500	380
9509	11.946	41.106	1321197	729298	377
9510	11.950	41.115	1321699	730203	372
9511	11.955	41.122	1322252	731005	367
9512	11.960	41.130	1322801	731851	367
9513	11.964	41.138	1323303	732697	367
9514	11.969	41.146	1323850	733551	367
9515	11.975	41.154	1324451	734452	370
9601	11.860	41.082	1311699	726702	365
9602	11.865	41.090	1312300	727552	371
9603	11.870	41.098	1312848	728401	376
9604	11.875	41.105	1313401	729202	374
9605	11.880	41.113	1313943	730051	373
9606	11.885	41.121	1314500	730900	373
9607	11.890	41.128	1314501	730900	373
9608	11.895	41.136	1315048	731703	373
9609	11.900	41.144	1315607	732552	373
9707	11.888	41.089	1314851	727445	372
9708	11.898	41.107	1315915	729350	380
9713	11.927	41.164	1319149	735549	373
9714	11.932	41.174	1319801	736652	376
9801	11.885	41.060	1314500	724250	370
9802	11.890	41.067	1315001	725102	370
9803	11.895	41.076	1315602	726003	377
9804	11.898	41.082	1315938	726690	387
9805	11.898	41.094	1315935	728002	377
9806	11.907	41.105	1316962	729136	383
9807	11.914	41.106	1317750	729301	380
9808	11.919	41.114	1318252	730151	382
9809	11.924	41.122	1318850	731002	374
9810	11.929	41.129	1319350	731800	375
9811	11.934	41.138	1319902	732700	377
9812	11.939	41.145	1320501	733501	377
9813	11.943	41.153	1321000	734399	378
9814	11.948	41.161	1321498	735248	377
9815	11.952	41.169	1322000	736099	377
9816	11.957	41.176	1322501	736896	377
9901	11.897	41.052	1315751	723441	368
9902	11.901	41.060	1316249	724249	368
9903	11.908	41.073	1316764	725050	370
9904	11.906	41.067	1317040	725739	372
9905	11.925	41.099	1318951	728501	371
9906	11.930	41.106	1319503	729298	373
9907	11.935	41.114	1320200	730188	373
9908	11.939	41.122	1320501	730999	369
9909	11.944	41.130	1321100	731848	376
9912	11.959	41.153	1322697	734343	378
9913	11.964	41.161	1323251	735247	373
9914	11.969	41.169	1323794	736047	378

SUPPORTING INFORMATION FOR CHAPTER 5

C.1   2D model and MT responses of Habanero

The appendix contains modeling results of MT baseline regional and monitoring surveys conducted at Habanero EGS project in South Australia. Pseudo-section plots of the observed data and model responses of TE and TM modes for the 2D inversion of profile LON (baseline regional MT survey) are shown in Figure C.2. The 2D resistivity model of profile LOE from regional baseline MT survey using starting model of resistivity logs and the corresponding pseudo-section plots of the observed data and model responses are displayed in Figures C.3 and C.4 (the location of profile LOE is shown in Figure C.1). The fits of xy and yx resistivity and phase data for time-lapse inversion of site 09 are shown in Figures C.5 and C.6, respectively. The fits of xy and yx resistivity and phase data for time-lapse inversion of site 28 are displayed in Figures C.7 and C.8, respectively. Tables C.1 and C.2 contain station locations of profiles LOE and LON for the baseline survey at Habanero EGS. Table C.3 consists of station locations for the time-lapse monitoring survey at Habanero EGS.
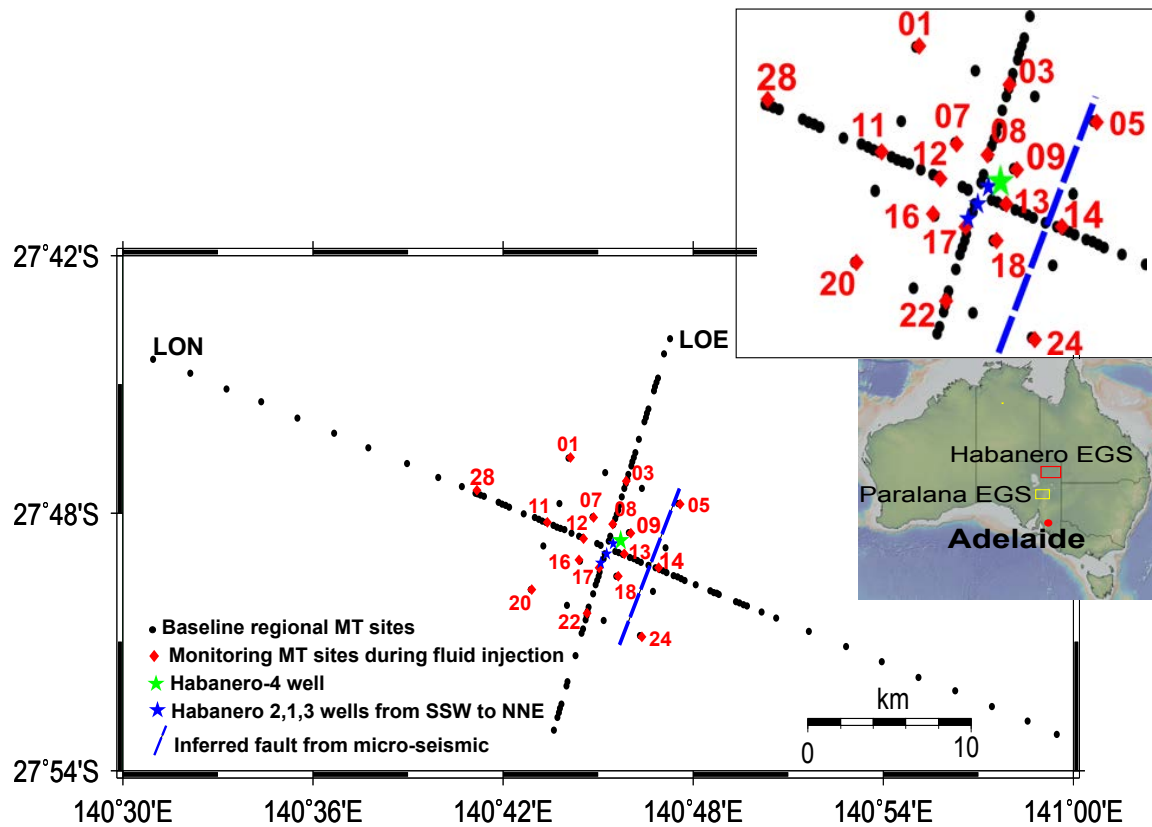
Figure C.1: Location map of MT sites at the Habanero EGS located in South Australia. Black dots denote MT stations of baseline survey along two profiles LOE and LON and infill station in a grid. The red diamonds denote time-lapse monitoring MT stations. Green star is Habanero-4 well and blue stars are Habanero-2, 1, 3 wells from SSW to NNE, respectively. The red square on the inset is Habanero EGS project area. The yellow square on the inset is Paralana EGS project area.
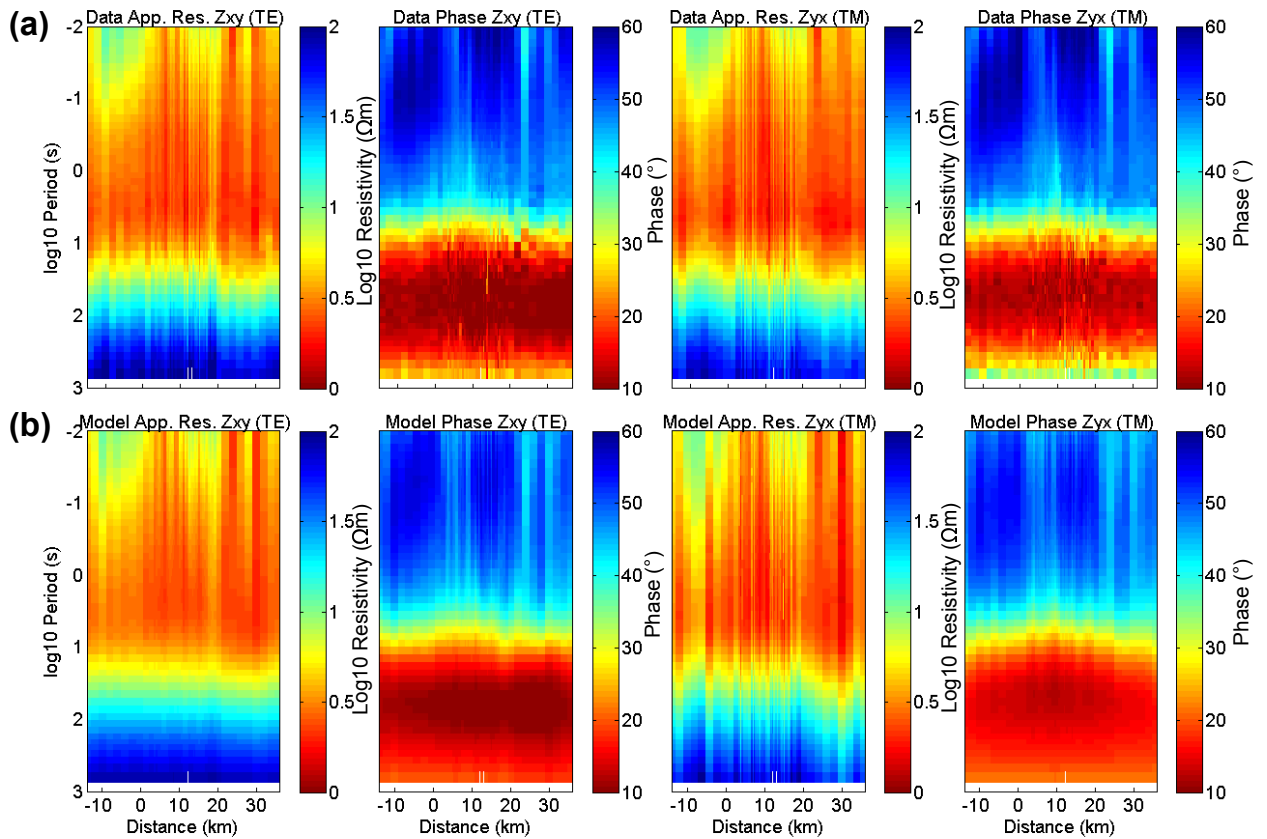
Figure C.2: Pseudo-section plots of (a) observed resistivity and phase for TE and TM modes (b) calculated responses for resistivity and phase for TE and TM modes of the baseline survey along the profile LON from NW to SE direction.
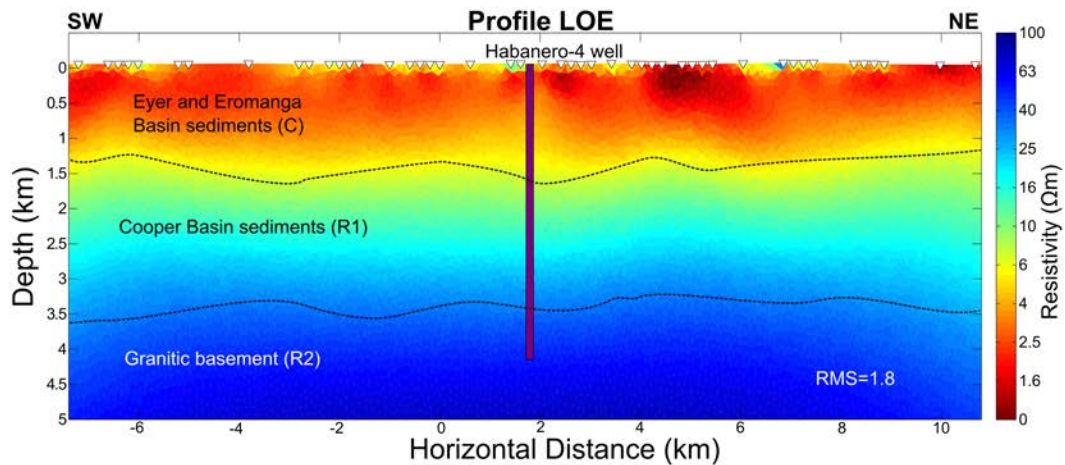
Figure C.3: Preferred 2D resistivity model obtained by joint inversion of TE and TM modes baseline MT data for profile LOE with a RMS misfit of 1.8. C is a low resistivity layer. R1 is intermediate resistivity layer and R2 is a high resistivity layer. The MT data were rotated to geoelectric strike of N40°W before the inversions.
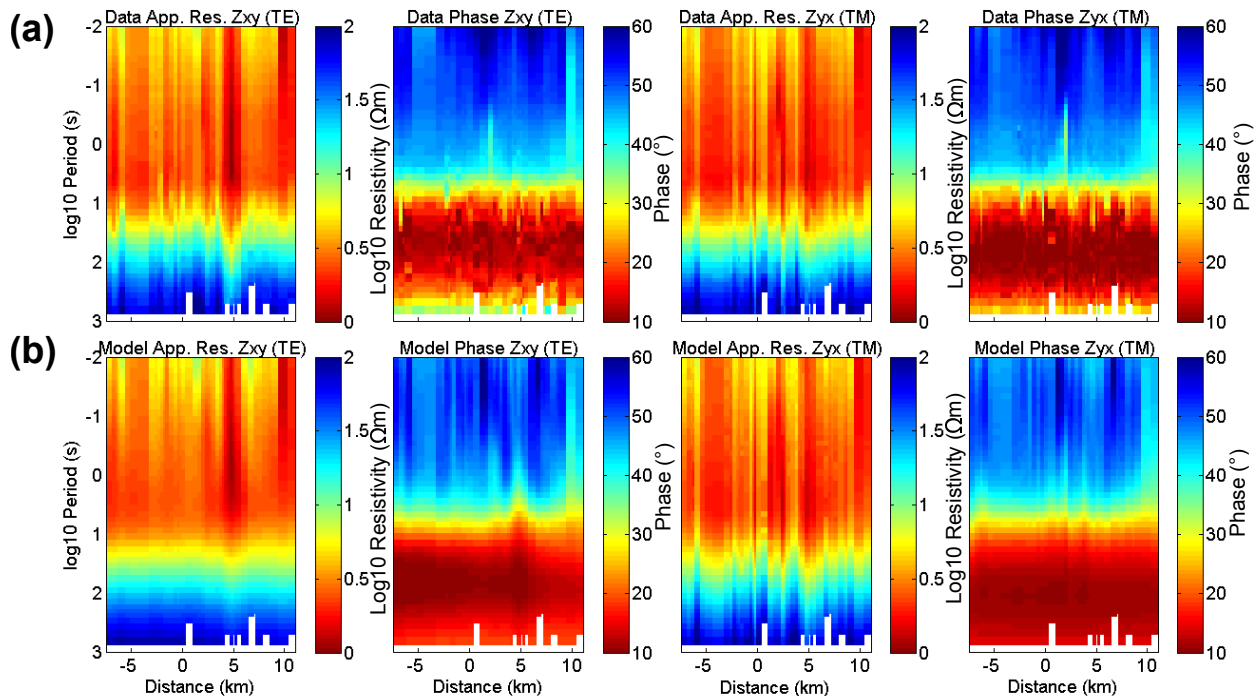
Figure C.4: Pseudo-section plots of (a) observed resistivity and phase for TE and TM modes (b) calculated responses for resistivity and phase for TE and TM modes along the profile LOE from SW to NE.
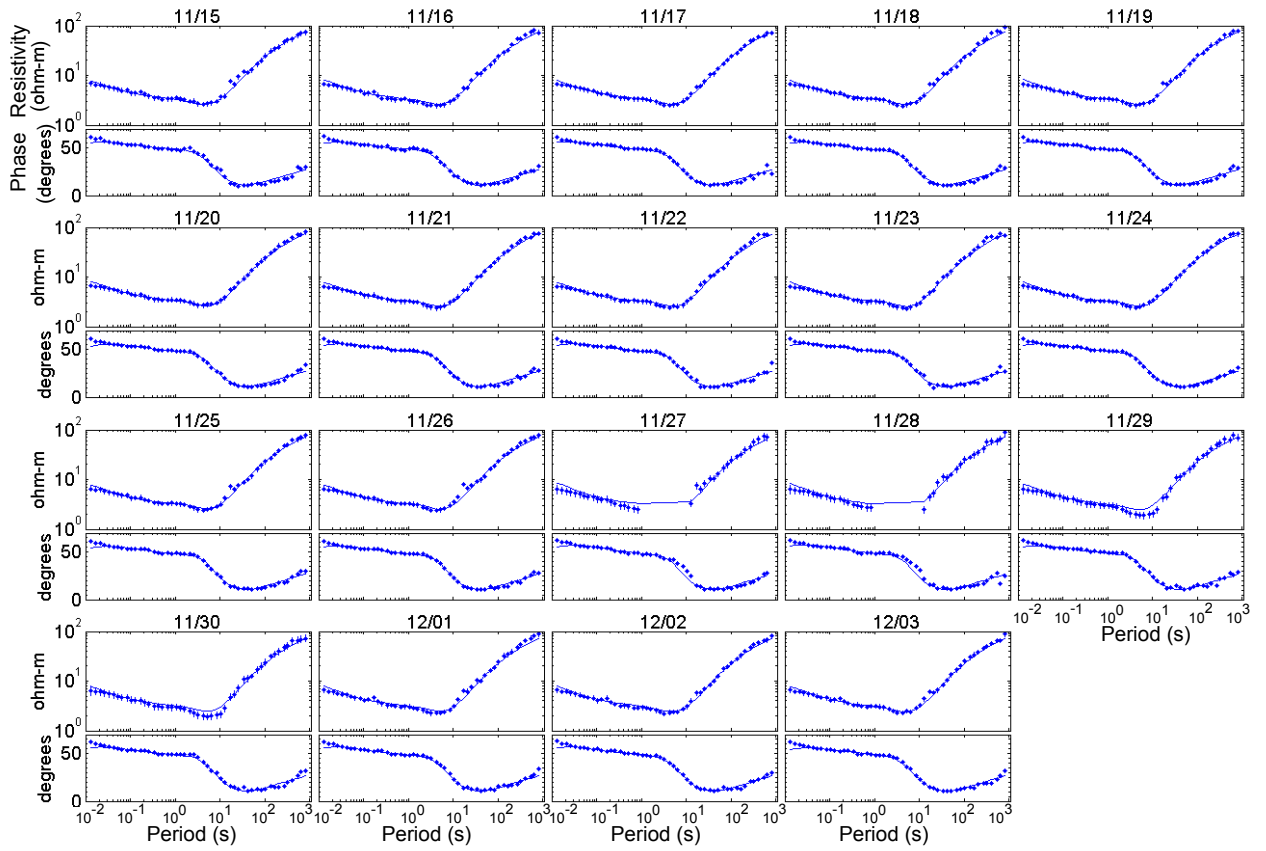
Figure C.5: Fits of xy component resistivity and phase data for the time-lapse 2D model of site 09 with an overall RMS of 1.0. The numbers on top of the plots are month/day.
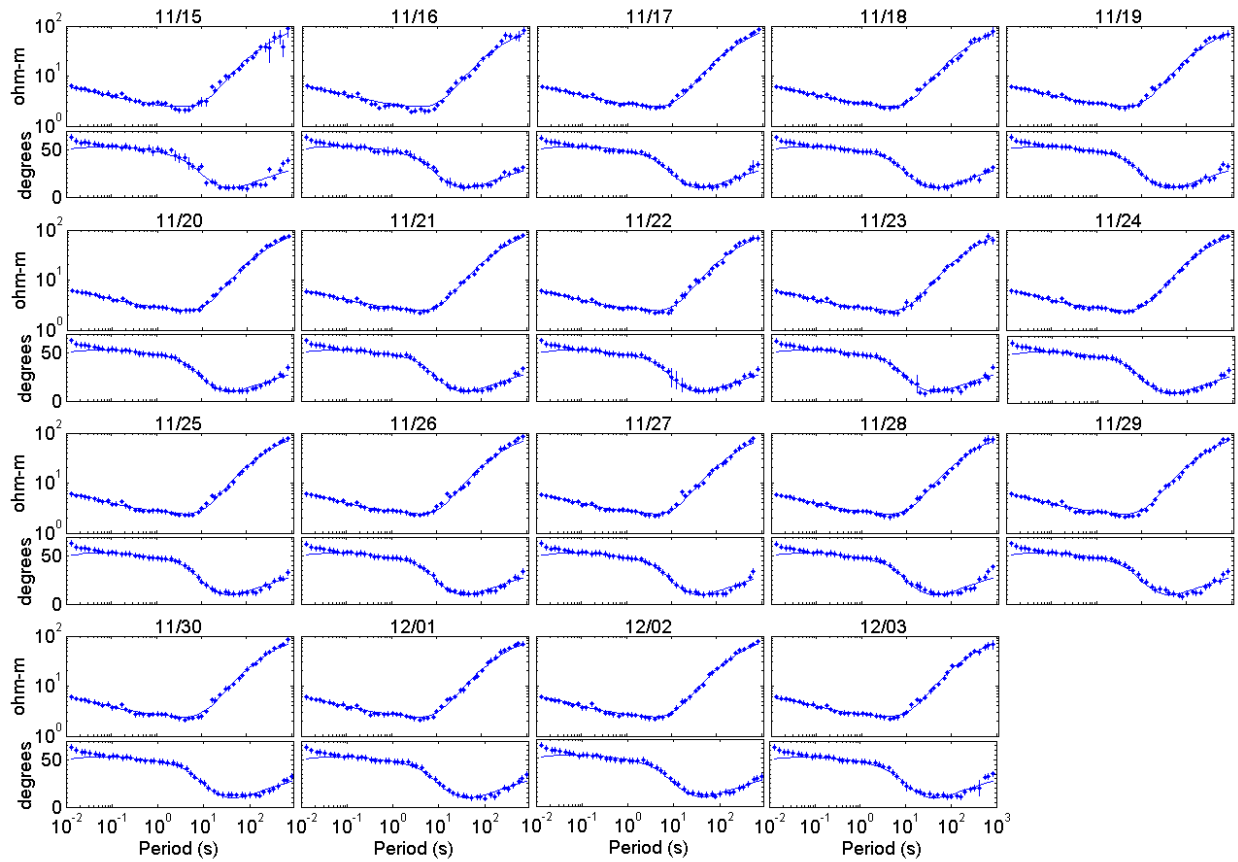
Figure C.6: Fits of yx component resistivity and phase data for the time-lapse 2D model of site 09 with an overall RMS of 1.0. The numbers on top of the plots are month/day.
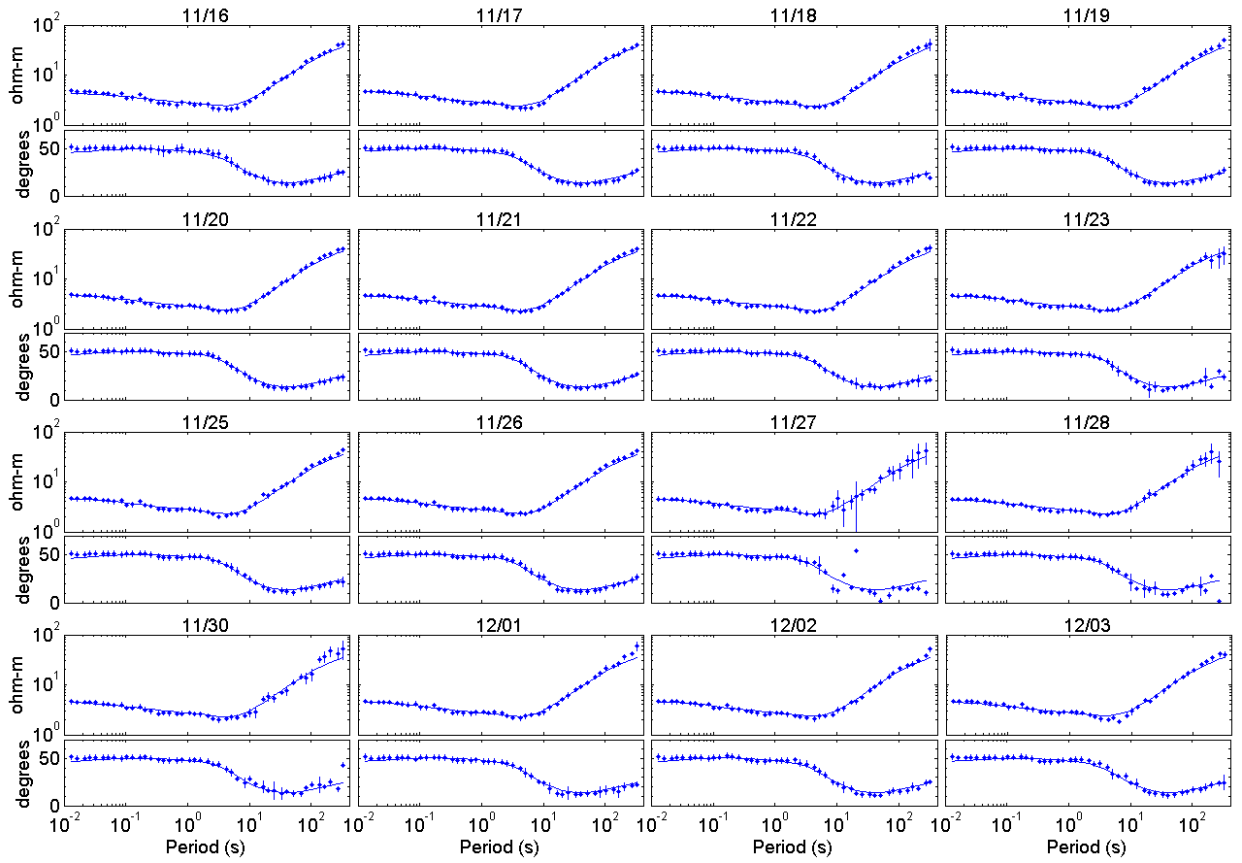
Figure C.7: Fits of xy component resistivity and phase data for the time-lapse 2D model of site 28 with an overall RMS of 1.0. The numbers on top of the plots are month/day.
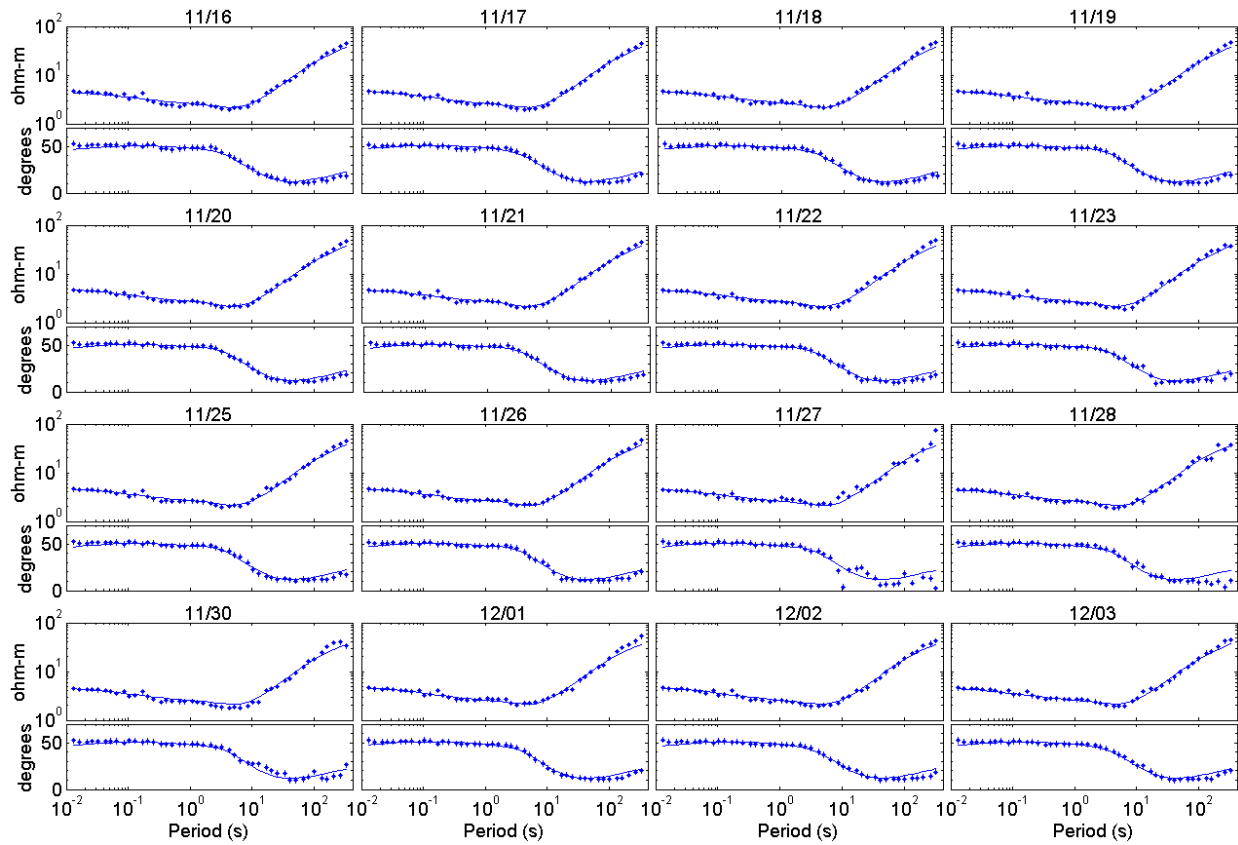
Figure C.8: Fits of yx component resistivity and phase data for the time-lapse 2D model of site 28 with an overall RMS of 1.0. The numbers on top of the plots are month/day.

Table C.1: MT sites locations for profile LOE of the baseline regional survey at Habanero EGS.

station	Latitude	Longitude	Easting (UTM)	Northing(UTM)	Elevation (m)
Profile LOE					
-8300	-27.8840	140.7270	473110	6915591	58
-7700	-27.8790	140.7290	473292	6916154	60
-7500	-27.8770	140.7290	473359	6916343	60
-7300	-27.8760	140.7300	473424	6916533	60
-7100	-27.8740	140.7310	473490	6916720	61
-6300	-27.8670	140.7330	473750	6917479	59
-6100	-27.8650	140.7340	473818	6917669	60
-4900	-27.8550	140.7380	474209	6918803	65
-3900	-27.8470	140.7410	474532	6919754	58
-3700	-27.8450	140.7420	474595	6919943	58
-3300	-27.8420	140.7430	474730	6920324	57
-3100	-27.8400	140.7440	474797	6920515	59
-2900	-27.8380	140.7450	474856	6920705	59
-2700	-27.8360	140.7450	474896	6920894	61
-2100	-27.8310	140.7470	475131	6921457	54
-1700	-27.8280	140.7490	475266	6921840	56
-1500	-27.8260	140.7500	475332	6922029	58
-1300	-27.8240	140.7500	475400	6922216	57
-1100	-27.8230	140.7510	475471	6922400	55
-500	-27.8180	140.7530	475662	6922980	60
-300	-27.8160	140.7530	475721	6923166	62
300	-27.8110	140.7560	475935	6923734	69
500	-27.8090	140.7560	476003	6923923	67
900	-27.8050	140.7580	476136	6924329	65
1300	-27.8020	140.7590	476273	6924682	65
1500	-27.8010	140.7600	476339	6924868	60
1700	-27.7990	140.7600	476405	6925057	55
1900	-27.7970	140.7610	476472	6925251	58
2300	-27.7940	140.7630	476606	6925630	70
2700	-27.7900	140.7640	476742	6926009	62
2900	-27.7890	140.7650	476809	6926198	59
3100	-27.7870	140.7650	476877	6926389	55
3300	-27.7850	140.7660	476944	6926578	55
3700	-27.7820	140.7670	477081	6926956	53
3900	-27.7800	140.7680	477149	6927145	54
4100	-27.7780	140.7690	477217	6927336	56
4300	-27.7770	140.7690	477287	6927525	60
4900	-27.7710	140.7720	477490	6928099	67
5700	-27.7650	140.7740	477767	6928852	76
5900	-27.7630	140.7750	477838	6929041	70
6100	-27.7610	140.7760	477907	6929230	71
6300	-27.7600	140.7760	477976	6929418	76
7100	-27.7530	140.7790	478254	6930178	62
7300	-27.7510	140.7800	478322	6930367	64
7500	-27.7490	140.7810	478393	6930556	62
7700	-27.7480	140.7810	478461	6930743	56
8775	-27.7380	140.7850	478784	6931779	47
9500	-27.7320	140.7880	479089	6932447	50

Table C.2: MT sites locations for profile LON at Habanero EGS

station	Latitude	Longitude	Easting (UTM)	Northing(UTM)	Elevation (m)
Profile LON					
-25000	-27.7400	140.5160	452309	6931479	36
-23000	-27.7460	140.5360	454229	6930857	39
-21000	-27.7520	140.5550	456130	6930203	40
-19000	-27.7570	140.5730	457924	6929663	38
-17000	-27.7630	140.5920	459785	6928955	36
-15000	-27.7690	140.6110	461702	6928326	37
-13000	-27.7750	140.6290	463463	6927707	45
-11000	-27.7810	140.6500	465501	6927037	35
-9300	-27.7860	140.6650	466984	6926482	48
-7800	-27.7900	140.6790	468406	6926014	48
-7150	-27.7920	140.6860	469025	6925786	48
-7050	-27.7920	140.6870	469120	6925751	48
-6900	-27.7930	140.6880	469261	6925701	48
-6700	-27.7940	140.6900	469452	6925632	49
-5900	-27.7960	140.6980	470213	6925368	49
-5700	-27.7960	140.7000	470400	6925306	45
-5500	-27.7970	140.7010	470589	6925241	47
-5300	-27.7980	140.7030	470778	6925179	51
-4500	-27.8000	140.7110	471532	6924901	51
-3900	-27.8020	140.7170	472107	6924716	48
-3700	-27.8020	140.7190	472296	6924652	53
-3500	-27.8030	140.7210	472485	6924587	52
-3300	-27.8040	140.7230	472671	6924525	47
-2900	-27.8050	140.7260	473053	6924393	39
-2700	-27.8050	140.7280	473243	6924328	37
-2500	-27.8060	140.7300	473433	6924263	34
-2300	-27.8070	140.7320	473622	6924200	31
-1900	-27.8080	140.7360	473998	6924072	49
-1500	-27.8090	140.7400	474379	6923938	49
-1300	-27.8100	140.7420	474570	6923873	52
-500	-27.8120	140.7490	475327	6923613	60
-300	-27.8120	140.7510	475516	6923548	65
500	-27.8150	140.7590	476275	6923287	54
700	-27.8150	140.7610	476463	6923220	66
900	-27.8160	140.7630	476653	6923155	76
1300	-27.8170	140.7670	477034	6923025	74
1500	-27.8180	140.7690	477223	6922955	71
1700	-27.8180	140.7710	477410	6922894	69
1900	-27.8190	140.7730	477600	6922831	69
2300	-27.8200	140.7760	477979	6922691	73
2700	-27.8210	140.7800	478359	6922570	74
2900	-27.8220	140.7820	478549	6922505	74
3100	-27.8230	140.7840	478737	6922441	74
3300	-27.8230	140.7860	478925	6922376	77
3700	-27.8240	140.7900	479306	6922247	69
3900	-27.8250	140.7920	479495	6922183	71
4100	-27.8250	140.7940	479682	6922115	71
4300	-27.8260	140.7960	479873	6922048	73
4900	-27.8280	140.8010	480447	6921854	70
5700	-27.8300	140.8090	481201	6921596	70
5900	-27.8310	140.8110	481389	6921529	70
6050	-27.8310	140.8120	481531	6921480	69
6150	-27.8320	140.8130	481626	6921447	67
7100	-27.8340	140.8230	482526	6921138	64
7300	-27.8350	140.8240	482717	6921073	67
7500	-27.8350	140.8260	482908	6921009	68
7700	-27.8360	140.8280	483096	6920944	68
8500	-27.8380	140.8360	483856	6920678	70
9300	-27.8410	140.8440	484613	6920427	62
11000	-27.8460	140.8610	486327	6919856	60
13000	-27.8520	140.8810	488269	6919185	49
15000	-27.8580	140.8990	490094	6918564	46
17000	-27.8640	140.9190	491995	6917873	48
19000	-27.8690	140.9380	493908	6917313	62
21000	-27.8750	140.9570	495816	6916631	59
23000	-27.8810	140.9760	497661	6915991	63
24800	-27.8860	140.9920	499227	6915390	73

Table C.3: MT sites locations for the time-lapse survey at Habanero EGS.

Station	Latitude	Longitude	Easting	Northing	Elevation(m)
1	-27.77835	140.73552	473942	6927323	43
3	-27.78750	140.76487	476836	6926315	52
5	-27.79658	140.79327	479634	6925313	61
7	-27.80178	140.74773	475152	6924729	45
8	-27.80430	140.75770	476135	6924452	51
9	-27.80775	140.76730	477080	6924072	60
11	-27.80362	140.72328	472743	6924522	51
12	-27.80985	140.74245	474632	6923836	46
13	-27.81578	140.76382	476739	6923181	66
16	-27.81820	140.73987	474387	6922965	43
17	-27.82117	140.75067	475456	6922583	42
18	-27.82442	140.76063	476427	6922226	45
20	-27.82968	140.71522	471954	6921633	42
22	-27.83882	140.74425	474816	6920625	48
24	-27.84793	140.77298	477647	6919623	65
28	-27.79105	140.68617	469084	6925905	41
Remote1	-28.47363	141.61540	560244	6850175	115
Remote2	-27.72633	141.35382	534877	6933062	76

BIBLIOGRAPHY

Abbate, E., Passerini, P., and Zan, L. (1995). Strike-slip faults in a rift area: a transect in the Afar Triangle, East Africa. *Tectonophysics*, 241(1):67–97.

Acocella, V., Abebe, B., Korme, T., and Barberi, F. (2008). Structure of Tendaho Graben and Manda Hararo Rift: Implications for the evolution of the southern Red Sea propagator in central Afar. *Tectonics*, 27(4).

Albaric, J., Oye, V., Langet, N., Hasting, M., Lecomte, I., Iranpour, K., Messeiller, M., and Reid, P. (2014). Monitoring of induced seismicity during the first geothermal reservoir stimulation at Paralana, Australia. *Geothermics*, 52:120 – 131.

Amdeberhan, Y. (1998). *A conceptual reservoir model and production capacity estimate for the Tendaho geothermal field, Ethiopia*, volume Rep. UNU-GTP-1998-01. United Nations University, Reykjavik, Iceland.

Anderson, E., Crosby, D., and Ussher, G. (2000). Bulls-Eye!–simple resistivity imaging to reliably locate the geothermal reservoir. In *Proceedings of World Geothermal Congress, Kyushu–Tohoku, Japan, 28 May - 10 June*, pages 909–914.

Aquater (1979). Geothermal resources exploration project Tendaho area - prefeasibility study. Technical report, EIGS and Ministry of Foreign Affairs of Italy.

Aquater (1980). Geothermal resource exploration project Tendaho area, feasibility study - Phase II. Technical report, EIGS and Ministry of Foreign Affairs of Italy.

Aquater (1995). Micro-seismic study, final report. Technical report, EIGS and Ministry of Foreign Affairs of Italy.

Aquater (1996a). Tendaho geothermal project, final report, Volume I. Technical report, MME, EIGS - Government of Italy, Ministry of Foreign Affairs.

Aquater (1996b). Tendaho geothermal project, final report, Volume II. Technical report, MME, EIGS - Government of Italy, Ministry of Foreign Affairs.

Archie, G. (1942). The electrical resistivity log as an aid in determining some reservoir characteristics. *Trans. Am. Inst. Mech. Eng*, 146(99):54–62.

Árnason, K., Eysteinsson, H., and Hersir, G. P. (2010). Joint 1D inversion of TEM and MT data and 3D inversion of MT data in the Hengill area, SW Iceland. *Geothermics*, 39(1):13–34.

Audigane, P., Royer, J.-J., and Kaieda, H. (2002). Permeability characterization of the Soultz and Ogachi large-scale reservoir using induced microseismicity. *Geophysics*, 67(1):204–211.

Ayling, B. F., Hogarth, R. A., and Rose, P. E. (2015). Tracer testing at the Habanero EGS site, central Australia. In *Proceeding of World Geothermal Congress, Melbourne, Australia, 19-25 April* , pages 1–10.

Bahr, K. (1988). Interpretation of the magnetotelluric impedance tensor: regional induction and local telluric distortion. *Journal of Geophysics*, pages 119–127.

Baisch, S., Rothert, E., Stang, H., Vrs, R., Koch, C., and McMahon, A. (2015). Continued geothermal reservoir stimulation experiments in the Cooper Basin (Australia). *Bulletin of the Seismological Society of America*, 105(1):198–209.

Baria, R., Michelet, S., Baumgaertner, J., Dyer, B., Gerard, A., Nicholls, J., Hettkamp, T., Teza, D., Soma, N., and Asanuma, H. (2004). Microseismic monitoring of the world's largest potential HDR reservoir. In *Proceedings of the Twenty-Ninth Workshop on Geothermal Reservoir Engineering, Stanford University, Stanford, California, 26-28 Jan.*, pages 194–201.

Barrat, J. A., Joron, J. L., Taylor, R. N., Fourcade, S., Nesbitt, R. W., and Jahn, B. M. (2003). Geochemistry of basalts from Manda Hararo, Ethiopia: LREE-depleted basalts in Central Afar. *Lithos*, 69:1–13.

Barton, C., Moos, D., Hartley, L., Baxter, S., Foulquier, L., Holl, H., and Hogarth, R. (2013). Geomechanically coupled simulation of flow in fractured reservoirs. In *Proceedings of the Thirty-Eighth Workshop on Geothermal Reservoir Engineering, Stanford Univ., Stanford, Calif., 11-13 Feb., SGP-TR-198*, pages 1–12. Stanford Univ., Stanford, Calif.

Battistelli, A., Yiheyis, A., Calore, C., Ferragina, C., and Abatneh, W. (2002). Reservoir engineering assessment of Dubti geothermal field, Northern Tendaho Rift, Ethiopia. *Geothermics*, 31:381–406.

Beardsmore, G. (2004). The influence of basement on surface heat flow in the Cooper Basin. *Exploration Geophysics*, 35(4):223–235.

Becken, M. and Burkhardt, H. (2004). An ellipticity criterion in magnetotelluric tensor analysis. *Geophysical Journal International*, 159:69–82.

Bedrosian, P., Weckmann, U., Ritter, O., Hammer, C., Hübert, J., and Jung, A. (2004). Electromagnetic monitoring of the groß schönebeck stimulation experiment. *proceedings Jahrestagung der Deutschen Geophysikalischen Gessellschaft*, 64.

Bendall, B., Hogarth, R., Holl, H., McMahon, A., Larking, A., and Reid, P. (2014). Australian experiences in EGS permeability enhancement - A review of 3 case studies. In *Proceedings of the Thirty-Ninth Workshop on Geothermal Reservoir Engineering, Stanford University, Stanford, California, 24-26 Feb, SGP-TR-202*, pages 1–10.

Berckhemer, H. and Baier, B. (1975). Deep seismic sounding in the Afar region and on the highland of Ethiopia. In *Proceedings of the International Symposium on the Afar Region and Related Rift Problems,Schweizerbart, I, Stuttgart*, pages 89–107.

Bertani, R. (2015). Geothermal power generation in the world 2010-2014 update report. In *Proceedings of World Geothermal Congress, Melbourne, Australia, 19-25 April*, pages 1–19.

Bertrand, E., Caldwell, T., Hill, G., Wallin, E., Bennie, S., Cozens, N., Onacha, S., Ryan, G., Walter, C., and Zaino, A. (2012). Magnetotelluric imaging of upper-crustal convection plumes beneath the Taupo Volcanic Zone, New Zealand. *Geophysical Research Letters*, 39(2):L02304.

Bibby, H., Caldwell, T., and Brown, C. (2005). Determinable and nondeterminable parameters of galvanic distortion in magnetotellurics. *Geophysical Journal International*, 163(3):915–930.

Booker, J. (2014). The magnetotelluric phase tensor: a critical review. *Surveys in Geophysics*, 35(1):7–40.

Börner, J. H., Bär, M., and Spitzer, K. (2015). Electromagnetic methods for exploration and monitoring of enhanced geothermal systems–a virtual experiment. *Geothermics*, 55:78–87.

Britannica (2015). World map of tectonic plates. http://kids.britannica.com/comptons/art-143478. Accessed:2015-08-28.

Cagniard, L. (1953). Basic theory of the magneto-telluric method of geophysical prospecting. *Geophysics*, 18(3):605–635.

Calais, E., d'Oreye, N., Albaric, J., Deschamps, A., Delvaux, D., Déverchere, J., Ebinger, C., Ferdinand, R. W., Kervyn, F., Macheyeki, A. S., et al. (2008). Strain accommodation by slow slip and dyking in a youthful continental rift, East Africa. *Nature*, 456(7223):783–787.

Caldwell, T. G., Bibby, H. M., and Brown, C. (2004). The magnetotelluric phase tensor. *Geophysical Journal International*, 158:457–469.

Casey, M., Ebinger, C., Keir, D., Gloaguen, R., and Mohamed, F. (2006). Strain accommodation in transitional rifts: extension by magma intrusion and faulting in Ethiopian rift magmatic segments. *Special Publication-Geological Society of London*, 259:143.

Chamorro, C. R., Garcia-Cuesta, J. L., M., M. E., and Perez-Madrazo, A. (2014). Enhanced geothermal systems in Europe: An estimation and comparison of the technical and sustainable potentials. *Energy*, 65(0):250 – 263.

Chave, A. and Jones, A. G., editors (2012). *The magnetotelluric method: Theory and practice.* Cambridge University Press.

Chave, A. D. and Thomson, D. J. (2004). Bounded influence magnetotelluric response function estimation. *Geophysical Journal International*, 157(3):988–1006.

Cladouhos, T. T., Petty, S., Nordin, Y., Moore, M., Grasso, K., Uddenberg, M., Swyer, M., Julian, B., and Foulger, G. (2013). Micro-seismic monitoring of Newberry Volcano EGS demonstration. In *Proceedings of the Thirty-Eighth Workshop on Geothermal Reservoir Engineering, Stanford University, Stanford, California, 11-13 Feb. , SGP-TR-198*, pages 1–9.

Cuenot, N., Dorbath, C., and Dorbath, L. (2008). Analysis of the microseismicity induced by fluid injections at the EGS site of Soultz-sous-Forêts (Alsace, France): Implications for the characterization of the geothermal reservoir properties. *Pure and Applied Geophysics*, 165(5):797–828.

Cumming, W. (2009). Geothermal resource conceptual models using surface exploration data. In *Proceedings of the Thirty-Fourth workshop on Geothermal Reservoir Engineering, Stanford University, Stanford, California, 9-11 Feb., SGP-TR-187*, pages 1–6.

Cumming, W. and Mackie, R. (2010). Resistivity imaging of geothermal resources using 1D, 2D and 3D MT inversion and TDEM static shift correction illustrated by a Glass Mountain case history. In *Proceedings of World Geothermal Congress, Bali, Indonesia, 25-29 April*, pages 1–10.

de Groot-Hedlin, C. and Constable, S. (1990). Occam's inversion to generate smooth, two-dimensional models from magnetotelluric data. *Geophysics*, 55:1613–1624.

Delhi (1984). Mcleod 1 well completion report. Technical Report 5485, Delhi Petroleum Pty Ltd, 101 Grenfell Street, Adelaide 5000, Australia.

Desissa, M., Johnson, N., Whaler, K., Hautot, S., Fisseha, S., and Dawes, G. (2013). A mantle magma reservoir beneath an incipient mid-ocean ridge in Afar, Ethiopia. *Nature Geoscience.*, 6:861–865.

Didana, Y., Thiel, S., and Heinson, G. (2014). Magnetotelluric imaging of upper crustal partial melt at Tendaho graben in Afar, Ethiopia. *Geophysical Research Letters*, 41(9):3089–3095.

DiPippo, R. (2012). Chapter 22 - Enhanced Geothermal Systems Projects and Plants. In DiPippo, R., editor, *Geothermal Power Plants*, pages 443 – 481. Butterworth-Heinemann, Boston, third edition.

Ebinger, C., Ayele, A., Keir, D., Rowland, J., Yirgu, G., Wright, T., Belachew, M., and Hamling, I. (2010). Length and timescales of rift faulting and magma intrusion: The Afar rifting cycle from 2005 to present. *Annual Review of Earth and Planetary Sciences*, 38:439–466.

Ebinger, C., Keir, D., Ayele, A., Calais, E., Wright, T., Belachew, M., Hammond, J., Campbell, E., and Buck, W. (2008). Capturing magma intrusion and faulting processes during continental rupture: seismicity of the Dabbahu (Afar) rift. *Geophys. J. Int.*, 174:1138–1152.

Egbert, G. D. and Kelbert, A. (2012). Computational recipes for electromagnetic inverse problems. *Geophysical Journal International*, 189(1):251–267.

Evans, K. F., Genter, A., and Sausse, J. (2005). Permeability creation and damage due to massive fluid injections into granite at 3.5 km at Soultz: 1. Borehole observations. *J. Geophys. Res.*, 110(B4).

Farquharson, C. G., Oldenburg, D. W., Haber, E., Shekhtman, R., et al. (2002). An algorithm for the three-dimensional inversion of magnetotelluric data. *72st Ann. Internat. Mtg., Soc. Expl. Geophys*, pages 649–652.

Field, L., Blundy, J., Calvert, A., and Yirgu, G. (2013). Magmatic history of Dabbahu, a composite volcano in the Afar Rift, Ethiopia. *Geological Society of America Bulletin*, 125(1-2):128–147.

Flóvenz, Ó., Georgsson, L., and rnason, K. (1985). Resistivity structure of the upper crust in iceland. *Journal of Geophysical Research*, 90(B12):10136–10,150.

Flóvenz, Ó., Spangenberg, E., Kulenkampff, J., Árnason, K., Karlsdóttir, R., and Huenges, E. (2005). The role of electrical interface conduction in geothermal exploration. In *Proc. World Geothermal Congress, Antalya, Turkey*.

Gasperikova, E., Newman, G., Feucht, D., and Arnason, K. (2011). 3D MT characterization of two geothermal fields in Iceland. *GRC Trans.*, 35(1-2):16671671.

Gasperikova, E., Rosenkjaer, G. K., Arnason, K., Newman, G. A., and Lindsey, N. J. (2015). Resistivity characterization of the Krafla and Hengill geothermal fields through 3D MT inverse modelling. *Geothermics*, 57:246–257.

Gatehouse, C., Fanning, C., and Flint, R. (1995). Geochronology of the Big Lake Suite, Warburton Basin, northeastern South Australia. *Geological Survey of South Australia Quarterly Geological Notes*, 128:8–16.

Geiermann, J. and Schill, E. (2010). 2-D magnetotellurics at the geothermal site at Soultz-sous-Forêts: Resistivity distribution to about 3000 m depth. *Comptes Rendus Geoscience*, 342(7–8):587 – 599.

Genter, A., Evans, K., Cuenot, N., Fritsch, D., and Sanjuan, B. (2010). Contribution of the exploration of deep crystalline fractured reservoir of Soultz to the knowledge of Enhanced Geothermal Systems (EGS). *Comptes Rendus Geoscience*, 342(78):502–516.

Geodynamics (2004). Habanero-1 well completion report. Technical report, Geodynamics Ltd., Brisbane, Australia.

Gérard, A., Genter, A., Kohl, T., Lutz, P., Rose, P., and Rummel, F. (2006). The deep EGS (Enhanced Geothermal System) project at Soultz-sous-Forêts (Alsace, France). *Geothermics*, 35(56):473–483.

Guidarelli, M., Stuart, G., Hammond, J., Kendall, J., Ayele, A., and Belachew, M. (2011). Surface wave tomography across Afar, Ethiopia: Crustal structure at a rift triple-junction zone. *Geophysical Research Letters*, 38(24).

Hamling, I. J., Wright, T. J., Calais, E., Lewi, E., and Fukahata, Y. (2014). InSAR observations of post-rifting deformation around the Dabbahu rift segment, Afar, Ethiopia. *Geophysical Journal International*, 197(1):33–49.

Hammond, J. O. S., Kendall, J. M., Stuart, G. W., Keir, D., Ebinger, C., Ayele, A., and Belachew, M. (2011). The nature of the crust beneath the Afar triple junction: Evidence from receiver functions. *Geochem. Geophys. Geosysts.*, 12:Q12004.

Hashin, Z. and Shtrikman, S. (1962). A variational approach to the theory of the effective magnetic permeability of multiphase materials. *Journal of Applied Physics*, 33:3125–3131.

Hasting, M. A., Albaric, J., Oye, V., Reid, P., Messeiller, M., and Llanos, E. (2011). Micro-Seismic Monitoring During Stimulation at Paralana-2 South Australia. *AGU Fall Meeting Abstracts*, page 1159.

Hayward, N. J. and Ebinger, C. J. (1996). Variations in the along-axis segmentation of the Afar Rift system. *Tectonics*, 15(2):244–257.

Heise, W., Bibby, H., Caldwell, T., Bannister, S., Ogawa, Y., Takakura, S., and Uchida, T. (2007). Melt distribution beneath a young continental rift: the Taupo Volcanic Zone, New Zealand. *Geophysical Research Letters*, 34(14):L14313.

Heise, W., Caldwell, T. G., Bibby, H. M., and Bannister, S. C. (2008). Three-dimensional modelling of magnetotelluric data from the Rotokawa geothermal field, Taupo Volcanic Zone, New Zealand. *Geophysical Journal International*, 173(2):740–750.

Hill, A. and Gravestock, D. (1995). *Cooper Basin*, volume 2 of *The Phanerozoic*. South Australian Geological Survey Bulletin.

Hillis, R. and Reynolds, S. (2000). The Australian stress map. *Journal of the Geological Society*, 157(5):915–921.

Hillis, R. R., Sandiford, M., Reynolds, S. D., and Quigley, M. C. (2008). Present-day stresses, seismicity and Neogene-to-Recent tectonics of Australia's passive margins: intraplate deformation controlled by plate boundary forces. *Geological Society, London, Special Publications*, 306(1):71–90.

Hogarth, R., Holl, H., and McMahon, A. (2013). Flow testing results from the Habanero EGS project. In *Proceedings of Australian Geothermal Energy Conference, Brisbane, Australia, 14-15 Nov.*, pages 21–28.

Holl, H. and Barton, C. (2015). Habanero field-structure and state of stress. In *Proceedings of World Geothermal Congress, Melbourne, Australia, 19-25 April*, pages 1–8.

House, L. (1987). Locating microearthquakes induced by hydraulic fracturing in crystalline rock. *Geophysical Research Letters*, 14(9):919–921.

Jiracek, G. R. (1990). Near-surface and topographic distortions in electromagnetic induction. *Surveys in Geophysics*, 11(2-3):163–203.

Kalberkamp, U. (2010). Magnetotelluric surface exploration at Tendaho, Afar (Ethiopia). Federal Institute for Geosciences and Natural resources (BGR), Hannover, Germany.

Katusa, M. and Bustin, M. (2009). A hot future for geothermal. `http://www.safehaven.com/article/15247`. Accessed:2015-08-28.

Keir, D., Hamling, I. J., Ayele, A., Calais, E., Ebinger, C., Wright, T. J., Jacques, E., Mohamed, K., Hammond, J. O., and Belachew, M. (2009). Evidence for focused magmatic accretion at segment centers from lateral dike injections captured beneath the Red Sea rift in Afar. *Geology*, 37:59–62.

Kelbert, A., Meqbel, N., Egbert, G. D., and Tandon, K. (2014). Modem: A modular system for inversion of electromagnetic geophysical data. *Computers & Geosciences*, 66:40 – 53.

Key, K. (2009). 1D inversion of multicomponent, multifrequency marine CSEM data: Methodology and synthetic studies for resolving thin resistive layers. *Geophysics*, 74(2):F9–F20.

Key, K. and Ovall, J. (2011). A parallel goal-oriented adaptive finite element method for 2.5-D electromagnetic modelling. *Geophysical Journal International*, 186(1):137–154.

Kirkby, A., Heinson, G., Holford, S., and Thiel, S. (2015). Mapping fractures using 1D anisotropic modelling of magnetotelluric data: a case study from the Otway Basin, Victoria, Australia. *Geophysical Journal International*, 201(3):1961–1976.

Krieger, L. and Peacock, J. R. (2014). Mtpy: A Python toolbox for magnetotellurics. *Computers & Geosciences*, 72(0):167–175.

Lees, J. M. and Wu, H. (2000). Poisson's ratio and porosity at Coso geothermal area, California. *Journal of volcanology and geothermal research*, 95(1):157–173.

Lemma, Y. (2007). Magnetotelluric and transient electromagnetic method in geothermal exploration, with example from Tendaho Geothermal Field, Ethiopia. Technical Report Number 11, United Nation University-Geothermal Training Programme, Reykjavik, Iceland.

Li, S., Unsworth, M. J., Booker, J. R., Wei, W., Tan, H., and Jones, A. G. (2003). Partial melt or aqueous fluid in the mid-crust of Southern Tibet, Constraints from INDEPTH magnetotelluric data. *Geophysical Journal International*, 153:289–304.

Llanos, E. M., Zarrouk, S. J., and Hogarth, R. A. (2015). Numerical model of the Habanero geothermal reservoir, Australia. *Geothermics*, 53(0):308–319.

MacFarlane, J., Thiel, S., Pek, J., Peacock, J., and Heinson, G. (2014). Characterisation of induced fracture networks within an enhanced geothermal system using anisotropic electromagnetic modelling. *Journal of Volcanology and Geothermal Research*, 288:1–7.

Mackenzie, G., Thybo, H., and Maguire, P. (2005). Crustal velocity structure across the Main Ethiopian Rift: results from two-dimensional wide-angle seismic modelling. *Geophysical Journal International*, 162:994–1006.

Mackie, R. L., Smith, J. T., and Madden, T. R. (1994). Three-dimensional electromagnetic modeling using finite difference equations: The magnetotelluric example. *Radio Science*, 29(4):923–935.

McKenzie, D. (1978). Some remarks on the development of sedimentary basins. *Earth planet. Sci. Lett.*, 40:25–32.

McKenzle, D. and Morgan, W. (1969). Evolution of triple junctions. *Nature*, 224:125.

McMahon, A. and Baisch, S. (2013). Case study of the seismicity associated with the stimulation of the Enhanced Geothermal System at Habanero, Australia. In *Proceedings of Australian Geothermal Conference, Brisbane, Australia, 14-15 Nov.*, pages 29–36.

McMahon, A. and Baisch, S. (2015). Seismicity Associated with the Stimulation of the Enhanced Geothermal System at Habanero, Australia. In *Proceedings of World Geothermal Congress, Melbourne, Australia, 19-25 April*, pages 1–9.

Megersa, G. and Getaneh, E. (2006). Geological, surface hydrothermal alteration and geothermal mapping of Dubti-Semera area, Tendaho Geothermal Field. pp. 62, Geological Survey of Ethiopia, unpublished internal report, Addis Ababa, Ethiopia.

Meixner, A., Kirkby, A., and Lescinsky, D. (2012). The Cooper Basin 3D Map Version 2: Thermal modelling and temperature uncertainty. Technical Report Record2012/60, Geoscience Australia.

Meixner, A. J., Kirkby, A. L., and Horspool, N. (2014). Using constrained gravity inversions to identify high-heat-producing granites beneath thick sedimentary cover in the Cooper Basin region of central Australia. *Geothermics*, 51(0):483–495.

Meixner, T., Gunn, P., Boucher, R., Yeates, T., Richardson, L., and Frears, R. (2000). The nature of the basement to the Cooper Basin region, South Australia. *Exploration Geophysics*, 31(2):24–32.

Meqbel, N. (2009). *The electrical conductivity structure of the Dead Sea Basin derived from 2D and 3D inversion of magnetotelluric data.* Phd thesis, Free University of Berlin, Berlin, Germany.

Moeck, I. (2014). Catalog of geothermal play types based on geologic controls. *Renewable and Sustainable Energy Reviews*, 37:867–882.

Moeck, I. and Beardsmore, G. (2014). A new 'geothermal play type' catalog: Streamlining exploration decision making. In *Proceedings of the Thirty-Ninth Workshop on Geothermal Reservoir Engineering, Stanford University, Stanford, California, 24-26 Feb, SGP-TR-202*, pages 1–8.

Muñoz, G. (2014). Exploring for geothermal resources with electromagnetic methods. *Surveys in geophysics*, 35(1):101–122.

Newman, G. A., Gasperikova, E., Hoversten, G. M., and Wannamaker, P. E. (2008). Three-dimensional magnetotelluric characterization of the Coso geothermal field. *Geothermics*, 37(4):369–399.

Oskooi, B. and Manzella, A. (2011). 2D inversion of the magnetotelluric data from Travale geothermal field in Italy. *Journal of the Earth & Space Physics*, 36(4):1–18.

Pachauri, R. K., Allen, M., Barros, V., Broome, J., Cramer, W., Christ, R., Church, J., Clarke, L., Dahe, Q., Dasgupta, P., et al. (2014). Climate change 2014: Synthesis report. Contribution of Working Groups I, II and III to the fifth assessment report of the intergovernmental panel on climate change.

Parkinson, W. (1959). Directions of rapid geomagnetic fluctuations. *Geophysical Journal International*, 2(1):1–14.

Parkinson, W. (1962). The influence of continents and oceans on geomagnetic variations. *Geophysical Journal International*, 6(4):441–449.

Peacock, J. (2012). *Magnetotelluric Monitoring*. PhD thesis, School of Earth and Environmental Sciences, University of Adelaide, South Australia, Australia.

Peacock, J. R., Thiel, S., Heinson, G. S., and Reid, P. (2013). Time-lapse magnetotelluric monitoring of an enhanced geothermal system. *Geophysics*, 78(3):B121–B130.

Peacock, J. R., Thiel, S., Reid, P., and Heinson, G. (2012). Magnetotelluric monitoring of a fluid injection: Example from an enhanced geothermal system. *Geophys. Res. Lett.*, 39(18):L18403.

Pellerin, L., Johnston, J., and Hohmann, G. (1996). A numerical evaluation of electromagnetic methods in geothermal exploration. *Geophysics*, 61(1).

Pommier, A. and Le-Trong, E. (2011). "SIGMELTS": A web portal for electrical conductivity calculations in geosciences. *Computers & Geosciences*, 37:1450–1459.

Reynolds, S., Mildren, S., Hillis, R., Meyer, J., and Flottmann, T. (2005). Maximum horizontal stress orientations in the Cooper Basin, Australia: implications for platescale tectonics and local stress sources. *Geophysical Journal International*, 160(1):332–344.

Reynolds, S. D., Mildren, S. D., Hillis, R. R., and Meyer, J. J. (2006). Constraining stress magnitudes using petroleum exploration data in the Cooper–Eromanga Basins, Australia. *Tectonophysics*, 415(14):123–140.

Rikitake, T. (1951). Changes in earth current and their relation to the electrical state of the Earth's crust. *Bull. Earthq. Res. Inst, Univ. Tokyo*, 29:271–276.

Roberts, J. J. and Tyburczy, J. A. (1999). Partial-melt electrical conductivity: Influence of melt composition. *J. Geophys. Res.*, 104:7055–7065.

Rodi, W. and Mackie, R. L. (2001). Nonlinear conjugate gradients algorithm for 2-D magnetotelluric inversion. *GEOPHYSICS*, 66(1):174–187.

Rosas-Carbajal, M., Linde, N., Peacock, J., Zyserman, F., Kalscheuer, T., and Thiel, S. (2015). Probabilistic 3-D time-lapse inversion of magnetotelluric data: application to an enhanced geothermal system. *Geophysical Journal International*, 203(3):1946–1960.

Rowland, J. V., Baker, E., Ebinger, C. J., Keir, D., Kidane, T., Biggs, J., Hayward, N., and Wright, T. J. (2007). Fault growth at a nascent slow-spreading ridge: 2005 Dabbahu rifting episode, Afar. *Geophysics. J. Int.*, 171:1226–1246.

Sandiford, M., Wallace, M., and Coblentz, D. (2004). Origin of the in situ stress field in southeastern Australia. *Basin Research*, 16(3):325–338.

Sato, H. and Ida, Y. (1984). Low frequency electrical impedance of partially molten gabbro: the effect of melt geometry on electrical properties. *Tectonophysics*, 107:105–134.

Sen, P. N. and Goode, P. A. (1992). Influence of temperature on electrical conductivity on shaly sands. *Geophysics*, 57(1):89–96.

Simpson, F. and Bahr, K. (2005). *Practical magnetotellurics*. Cambridge University Press.

Singh, S. C., Crawford, W. C., Carton, H., Seher, T., Combier, V., Cannat, M., Canales, J. P., Düsünür, D., Escartin, J., and Miranda, J. M. (2006). Discovery of a magma chamber and faults beneath a Mid-Atlantic Ridge hydrothermal field. *Nature*, 442(7106):1029–1032.

Siripunvaraporn, W., Egbert, G., Lenbury, Y., and Uyeshima, M. (2005). Three-dimensional magnetotelluric inversion: data-space method. *Physics of the Earth and Planetary Interiors*, 150(13):3–14.

Spichak, V. and Manzella, A. (2009). Electromagnetic sounding of geothermal zones. *Journal of Applied Geophysics*, 68(4):459–478.

Stork, A., Stuart, G., Henderson, C. M., Keir, D., and Hammond, J. (2013). Uppermost mantle (pn) velocity model for the Afar region, Ethiopia: an insight into rifting processes. *Geophysical Journal International*, 193:321–328.

Teklemariam, M. and Beyene, K. (2005). Geothermal exploration and development in Ethiopia. In *Proceedings of World Geothermal Congress, Antalya, Turkey, 24-29 April*, pages 24–29.

ten Grotenhuis, S. M., Drury, M. R., Spiers, C. J., and Peach, C. J. (2005). Melt distribution in olivine rocks based on electrical conductivity measurements. *Journal of Geophysical Research: Solid Earth*, 110:B12201.

Tester, J. W., Anderson, B. J., Batchelor, A., Blackwell, D., DiPippo, R., Drake, E., Garnish, J., Livesay, B., Moore, M., Nichols, K., et al. (2006). The future of geothermal energy. *Impact of Enhanced Geothermal Systems (EGS) on the United States in the 21st Century, Massachusetts Institute of Technology, Cambridge, MA*, page 372.

Thiel, S., Heinson, G., Gray, D. R., and Gregory, R. T. (2009). Ophiolite emplacement in NE Oman: constraints from magnetotelluric sounding. *Geophysical Journal International*, 176(3):753–766.

Tietze, K. and Ritter, O. (2013). Three-dimensional magnetotelluric inversion in practice–the electrical conductivity structure of the San Andreas Fault in Central California. *Geophysical Journal International*, 195(1):130–147.

Tietze, K. and Ritter, O. (2014). Electromagnetic monitoring of the propagation of an injected polymer for enhanced oil recovery in Northern Germany. In *Proceedings of 76th EAGE Conference and Exhibition, Amsterdam RAI, The Netherlands, 16-19 June*, pages 1–5.

Tikhonov, A. (1950). On determining electrical characteristics of the deep layers of the Earth's crust. In *Doklady*, volume 73, pages 295–297.

Tyburczy, J. A. and Waff, H. S. (1983). Electrical conductivity of molten basalt and andesite to 25 kilobars pressure: Geophysical significance and implications for charge transport and melt structure. *Journal of Geophysical Research: Solid Earth*, 88:2413–2430.

UNDP (1973). Geology, geochemistry and hydrology of hot springs of the East African rift system within Ethiopia. Technical Report technical report DD/SF/ON/11, UNDP.

Ussher, G., Harvey, C., Johnstone, R., and Anderson, E. (2000). Understanding the resistivities observed in geothermal systems. In *Proceedings of World Geothermal Congress, Kyushu–Tohoku, Japan, 28 May - 10 June*, pages 1915–1920.

Volpi, G., Manzella, A., and Fiordelisi, A. (2003). Investigation of geothermal structures by magnetotellurics (MT): an example from the Mt. Amiata area, Italy. *Geothermics*, 32(2):131–145.

Wamalwa, A. M., Mickus, K. L., Serpa, L. F., and Doser, D. I. (2013). A joint geophysical analysis of the Coso geothermal field, south-eastern California. *Physics of the Earth and Planetary Interiors*, 214:25 – 34.

Waxman, M., Smits, L., et al. (1968). Electrical conductivities in oil-bearing shaly sands. *Society of Petroleum Engineers Journal*, 8(02):107–122.

Weaver, J., Agarwal, A., and Lilley, F. (2000). Characterization of the magnetotelluric tensor in terms of its invariants. *Geophysical Journal International*, 141(2):321–336.

Whaler, K. and Hautot, S. (2006). The electrical resistivity structure of the crust beneath the northern Main Ethiopian Rift. *special publication-geological society of London*, 259:293–305.

Wohlenberg, J. and Keppler, H. (1987). Monitoring and interpretation of seismic observations in hot dry rock geothermal energy systems. *Geothermics*, 16(4):441–445.

Wright, P. M., Ward, S. H., Ross, H. P., and West, R. C. (1985). State-of-the-art geophysical exploration for geothermal resources. *Geophysics*, 50(12):2666–2699.

Wright, T. J., Ebinger, C., Biggs, J., Ayele, A., Yirgu, G., Keir, D., and Stork, A. (2006). Magma-maintained rift segmentation at continental rupture in the 2005 Afar dyking episode. *Nature*, 442:291–294.

Yanagisawa, N., Matsunaga, I., Ngothai, Y., and Wyborn, D. (2011). Geochemistry change during circulation test of EGS system. In *Proceedings of the Thirty-Sixth Workshop on Geothermal Reservoir Engineering, Stanford University, Stanford, California, 31 Jan. - 2 Feb., SGP-TR-187*, pages 1–5.

Zhang, S., Paterson, M. S., and Cox, S. F. (1994). Porosity and permeability evolution during hot isostatic pressing of calcite aggregates. *Journal of Geophysical Research: Solid Earth (1978–2012)*, 99(B8):15741–15760.

Ziagos, J., Phillips, B. R., Boyd, L., Jelacic, A., Stillman, G., and Hass, E. (2013). A technology roadmap for strategic development of enhanced geothermal systems. In *Proceedings of the Thirty-Eighth Workshop on Geothermal Reservoir Engineering, Stanford University, Stanford, California, 11-13 Feb., SGP-TR-198*, pages 11–13.